UNIVERSITÀ DEGLI STUDI DI TORINO
Facoltà di Scienze Matematiche Fisiche e Naturali
Corso di Laurea Magistrale in Fisica

Tesi di Laurea Magistrale

Measurement of the ratio $\sigma(pp \to \chi_{2c})/\sigma(pp \to \chi_{1c})$ with the CMS detector at LHC

Relatore:
Dott. Stefano Argirò

Controrelatore:
Prof. Fabrizio Bianchi

Autore:
Emanuele Usai

7 Dicembre 2011 – A.A. 2010-2011

Contents

List of Figures

List of Tables

Abstract

This thesis presents the measurement of the $\sigma(pp \to \chi_{2c})/\sigma(pp \to \chi_{1c})$ ratio with the CMS detector at LHC. The measurement was performed with $4.0 fb^{-1}$ of pp collisions at $\sqrt{s} = 7TeV$ collected in 2011. The J/ψ were observed through their $\mu^+\mu^-$ decay while the photons were reconstructed through conversions in e^+e^- pairs in the CMS inner tracker. The kinematic range covered is $|y_{J/\psi}| < 1$, $7GeV < p_{T\,J/\psi} < 25GeV$ and $E_\gamma > 0.5GeV$.

The study of χ_c states is important because they contribute to a wide fraction ($\sim 30 - 40\%$) of the prompt J/ψ production in hadron collisions, moreover it represents a test for various theory models of heavy quarks and quarkonium production.

Thanks to the excellent performance of the CMS tracking system, a very good separation between the two resonances is achieved. The ratio, obtained from prompt production of χ_c, is corrected for reconstruction efficiency and is also derived for various J/ψ p_T bins. Several sources of systematic errors are examined.

The ratio is found to be $R = \sigma(pp \to \chi_{2c})/\sigma(pp \to \chi_{1c}) = 0.723 \pm 0.028(stat) \pm 0.041(syst)$; the value is in agreement with previous measurement from CDF experiment at Tevatron.

Abstract (in italiano)

Questa tesi presenta la misura del rapporto $\sigma(pp \to \chi_{2c})/\sigma(pp \to \chi_{1c})$ col rivelatore CMS a LHC. La misura è stata ottenuta con $4.0 fb^{-1}$ di collisioni pp a $\sqrt{s} = 7TeV$ collezionati nel corso del 2011. I mesoni J/ψ sono stati osservati attraverso il decadimento in $\mu^+\mu^-$ mentre i fotoni sono stati ricostruiti attraverso conversioni in coppie e^+e^- nel tracciatore di CMS. Il range cinematico coperto è $|y_{J/\psi}| < 1$, $7GeV < p_{T\,J/\psi} < 25GeV$ e $E_\gamma > 0.5GeV$.

Lo studio degli stati χ_c è importante perché danno un largo contributo alla produzione ($\sim 30 - 40\%$) prompt di J/ψ in collisioni adroniche, in più rappresentano un test per i vari modelli teorici sulla produzione di quark pesanti e quarkonio.

Grazie alle eccellenti prestazioni del sistema di tracciamento di CMS, si ottiene una ottima separazione tra le due risonanze. Il rapporto, misurato dalla produzione prompt di χ_c è corretto per l'efficienza di ricostruzione ed è riportato per diversi intervalli di p_T della J/ψ. Varie sorgenti di errori sistematici sono prese in considerazione.

Il rapporto si trova essere $R = \sigma(pp \to \chi_{2c})/\sigma(pp \to \chi_{1c}) = 0.723 \pm 0.028(stat) \pm 0.041(sist)$; il valore è in accordo con la misura precedentemente eseguita dall'esperimento CDF a Tevatron.

Introduction

The first chapter will briefly summarize the theory underlying heavy quarkonia production at hadron colliders. The basics of the main theory models and their predictions will be reviewed to better understand the current status or research in the field. Moreover a brief summary of χ_c measurements at other colliders is presented.

The second and third chapter of this thesis are devoted to the description of the Large Hadron Collider, its goals and some technical details. There will also be a description of the Compact Muon Solenoid experiment and its subdetectors, the technical details of the subdetectors (tracking system in particular) will be useful in the later chapters of the thesis. This introductory section will also include some details about the software framework, the data storage model and the related computational challenge.

The fourth chapter contains all the details of the analysis from candidates selection cuts and conversion reconstruction to efficiency and acceptance estimation. Various sources of possible systematic errors will be examined.

In the bibliography references for technical details on the Large Hadron Collider, the Compact Muon Solenoid detector and all of its subdetectors can be found. Bibiliography references are also provided for theoretical models on quarkonia production and decays.

Chapter 1

Theory Overview and Previous Studies

1.1 A Brief Review on the Theory of Charmonium Production and Decays

The quarkonium is a quark-antiquark bound state. Quarks with a mass higher than $\Lambda_{QCD} \simeq 300MeV$ (the scale at which perturbative expansion of QCD breaks), nominally the charm ($m_c \simeq 1.4GeV$), bottom ($m_b \simeq 4.5GeV$) and top ($m_t \simeq 175GeV$) quarks, are called "heavy". Heavy quarkonia are the bound states QQ, where Q is either a c or b quark. Due to the high mass, $t\bar{t}$ pairs are not known to form bound states (t quarks decay before bound states can be formed).

The lower-mass states of heavy quarkonium resonances are rather stable particles: due to their mass below the threshold for open heavy flavored meson pair production, their decay modes are either electromagnetic or OZI-suppressed (about 30% and 70% for charmonium). The first excited state for $c\bar{c}$ mesons is the J/ψ ($m_{J/\psi} \simeq 3.1GeV, \Gamma = 91keV$), while for $b\bar{b}$ mesons is the Υ ($m_\Upsilon = 9.5GeV, \Gamma = 53keV$). The excited states below the open charm/beauty threshold have widths ranging from a few dozens keV to a few dozens MeV. The spectrum of the heavy charmonium states is shown in Figure 1.1.

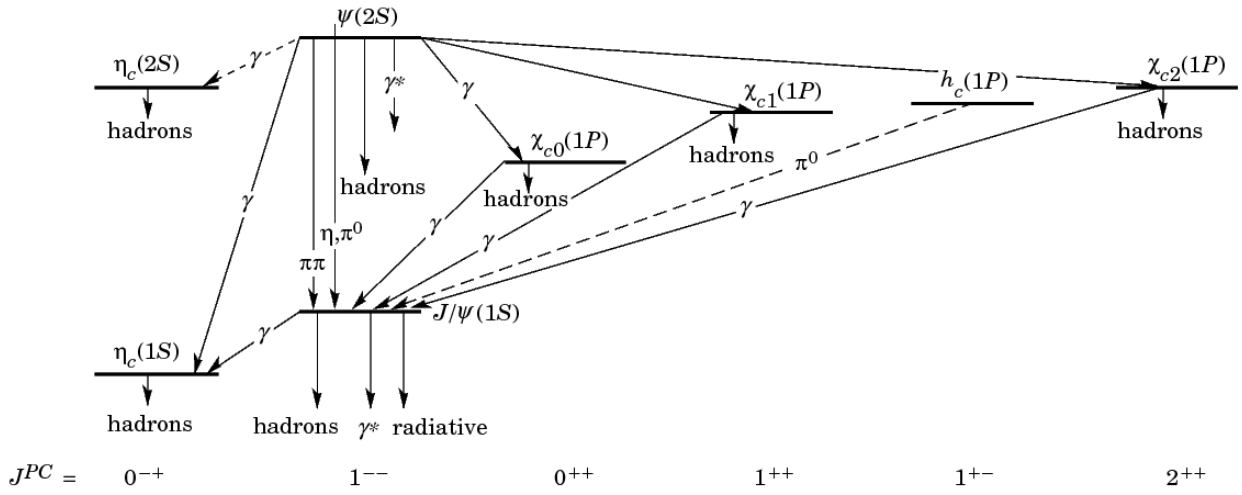

Figure 1.1: Charmonium spectroscopy diagram

The spectroscopy of quarkonia is phenomenologically described by assuming that the $Q\bar{Q}$ pair is subjected to the Cornell potential, consisting of a Coulomb-like term accounting for gluon-exchange between the two quarks and a confining term parametrizing the non-perturbative effects:

$$V(r) = -\frac{4}{3}\frac{\alpha_s(r)}{r} + k^2 r \tag{1.1}$$

The results obtained by solving the Schroedinger equation with the potential in Equation 1.1 with ad-hoc values of the parameters are in fair agreement with the observed spectra.

The mechanism of quarkonium production at hadron colliders is still an open research field. For what concerns the identification of the partons involved in the production of the $Q\bar{Q}$ pairs, earlier experiments ruled out the hypotesis of electromagnetic production via quark-quark annihilation. Similarly, the hypotesis of $q\bar{q}$ annihilation into a gluon as the main production process was rejected after the comparison between the production rate in pp and in $p\bar{p}$ collisions, since the difference between the $\bar{q}$ content of proton and antiproton should lead to a suppression in pp collisions by a factor 5-10, which is not observed. Thus quarkonium production proceeds mainly via gluon fusion ($gg \rightarrow Q\bar{Q}$) or gluon fragmentation. In Figure 1.2 reporting the main tree level Feynman diagrams contributing to quarkonium production.

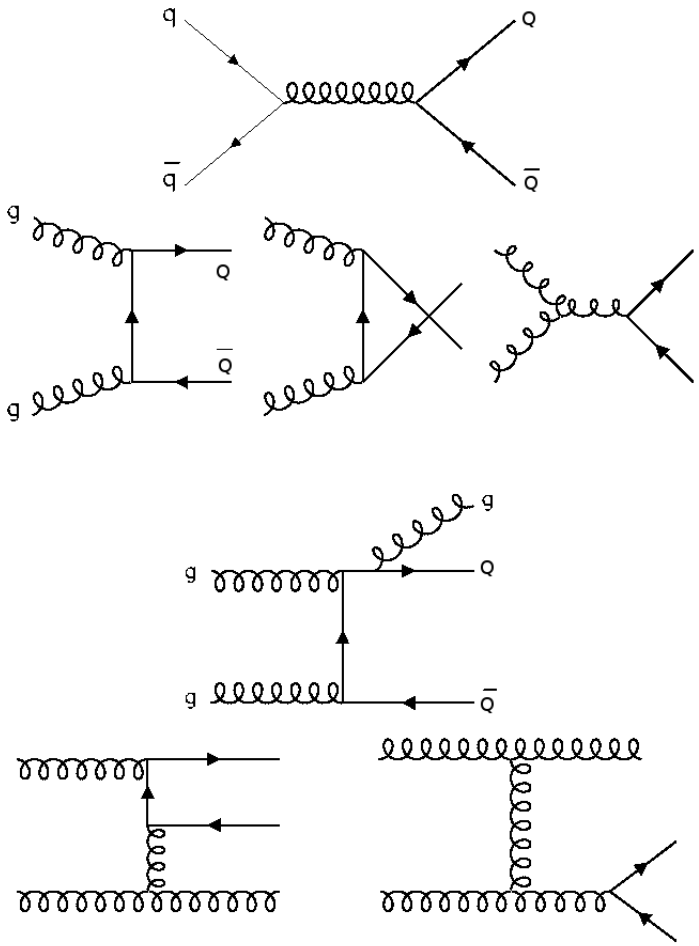

Figure 1.2: Main Feynman diagrams contributing to quarkonium production

In both heavy quarkonium annihilation decays and hard scattering production, large energy and momentum scales appear. The heavy quark mass m_Q is much larger than Λ_{QCD} and, in the case of production, the transverse momentum p_T can be much larger than Λ_{QCD} as well. This implies that the values of the QCD running coupling constant are much smaller than unity ($\alpha_S(m_c) \approx 0.25$ and $\alpha_S(m_b) \approx 0.18$). Therefore, one might hope that it would be possible to calculate the rates for heavy quarkonium decay and production accurately in perturbation theory. However, there are low-momentum, non-perturbative effects associated with the dynamics of the quarkonium bound state that invalidate the direct application of perturbation theory. In order to make use of perturbative methods, one must first separate the short-distance/high-momentum perturbative effects from the long-distance/low-momentum non perturbative effects; such a process is known under the name of factorization and nowadays is the basic approach to the problem of quarkonium production. Some models were developed over the years to describe theoretically or phenomenologically the quarkonia production mechanism and such models have been tested in the nineties on data collected at Tevatron.

1.1.1 Colour Evaporation Model (CEM)

The Colour Evaporation Model is the most phenomenological one and was first proposed in 1977. In the CEM, the production cross section for a quarkonium state H is a certain fraction F_H of the cross section for producing $Q\bar{Q}$ pairs with invariant mass below the $M\bar{M}$ threshold, where M is the lowest mass meson containing the heavy quark Q. This cross section has therefore an upper limit on the $Q\bar{Q}$ pair mass but no constraints on the colour or spin of the final state. The $Q\bar{Q}$ pair is assumed to neutralize its colour by interaction with the collision-induced colour field by colour evaporation. If the $Q\bar{Q}$ invariant mass is less than the heavy-meson threshold $2m_M$, then the additional energy that is needed to produce heavy-flavoured hadrons can be obtained from the nonperturbative colour field. Thus, the sum of the fractions F_H over all quarkonium states H can be less than unity. Further details about CEM can be found here [15] [18] [17] [2].

The fractions F_H are assumed to be universal so that, once they are determined by data, they can be used to predict the cross sections for other processes and for other kinematic regions. The leading-order calculation cannot describe the quarkonium p_T distribution, since the p_T of the $Q\bar{Q}$ pair is zero at LO. At NLO in α_S the subprocesses $ij \to kQ\bar{Q}$ (where k is a light quark, antiquark or gluon) produce $Q\bar{Q}$ pairs with nonzero p_T . The most recent set of FH values have been determined from complete NLO calculations of quarkonium production in hadronic collisions.

The most basic prediction of the CEM is that the ratio of the cross sections for any two quarkonium states should be constant, independent of the process and the kinematic region. Some variations in these ratios have been observed: for example the ratio of the cross sections for χ_c and J/ψ are rather different in photoproduction and hadroproduction. Such variations present a serious challenge to the status of the CEM as a quantitative model for quarkonium production, but nevertheless the model is still widely used as simulation benchmark.

1.1.2 Colour Singlet Model (CSM)

The colour-singlet model (CSM) was first proposed shortly after the discovery of the J/ψ. The main concept of the CSM is that, in order to produce a quarkonium, the $Q\bar{Q}$ pair must be generated with the quarkonium quantum numbers; in particular the pair has to be produced in a colour-singlet state.

1.1.3 Non Relativistic QCD (NRQCD)

One convenient way to carry out the separation between perturbative and nonperturbative effects is through the use of the effective field theory Non Relativistic QCD (NRQCD). NRQCD is more than a phenomenological model since it reproduces full QCD accurately at momentum scales of order $m_Q v$ and smaller, where v is the typical heavy quark velocity in the bound state in the CM frame ($v^2 \approx 0.3$ for charmonium, and $v^2 \approx 0.1$ for bottomonium). Virtual processes involving momentum scales of order m_Q and larger can affect the lower-momentum processes, and their effects are taken into account through the short-distance coefficients of the operators that appear in the NRQCD action.

The QQ pair can be produced in a colour-singlet state or in a colour-octet state. Its spin state can be singlet or triplet and it also can have orbital angular momentum.

Resonance	I^G	J^{PC}
$J/\psi(1S)$	0^-	1^{--}
$\chi_{c0}(1P)$	0^+	0^{++}
$\chi_{c1}(1P)$	0^+	1^{++}
$\chi_{c2}(1P)$	0^+	2^{++}

Table 1.1: χ_c states quantum numbers.

	Mass [MeV]	BR($\chi_c \to J/\psi + \gamma$)	$\Delta m(\chi_c, J/\psi)$ [MeV]
χ_{c0}	3414.75 ± 0.31	$1.14 \pm 0.08\%$	317.8
χ_{c1}	3510.66 ± 0.07	$34.1 \pm 1.5\%$	413.7
χ_{c2}	3556.20 ± 0.09	$19.4 \pm 0.8\%$	459.3

Table 1.2: χ_c states masses and branching fractions.

An important property of the matrix, which greatly increases the predictive power of NRQCD, is the fact that they are process independent; they can be calculated in lattice simulations or determined from phenomenology.

In practical calculations of the rates of quarkonium decay and production some uncertainties arises. In addition, the matrix elements are often poorly determined, either from phenomenology or lattice measurements. There are also large uncertainties in the heavy-quark masses (approximately 8% for m_c and approximately 2.4% for m_b) that can be very significant for quarkonium rates that are proportional to a large power of the mass. Many of the largest uncertainties in the theoretical predictions, as well as some of the experimental uncertainties, cancel out in the ratios of cross sections.

Another set of observables in which many of the uncertainties cancel out consists of polarization variables, which can be defined as ratios of cross sections for the production of different spin states of the same quarkonium. The NRQCD is in good agreement with data from CDF Run I for what concerns J/ψ and $\psi(2S)$ production cross sections but seems to fail in the case of $\Upsilon(1S)$ at low-pT because the NRQCD curve diverges like $1/p_T$ for small values of p_T.

In conclusion, NRQCD has been proved to be in good agreement with experimental results on quarkonium production cross sections. The measurement of polarization represents a further important test for the model. Further details about NRQCD can be found here: [3] [21] [16] [11].

1.2 The χ_c States

The only known ^3P_J states of charmonium are the χ_{c0}, χ_{c1} and χ_{c2}. They are the lowest ^3P states and the only narrow ones. They were first discovered in radiative decays from the 2^3S_1 level, the $\psi(3686)$ [22]. In turn they decay radiatively to the $J/\psi(3097)$. The spectrum of charmonium states, comprehensive of the χ_c resonances is shown in Figure 1.1. Spectroscopic information and symmetry properties of χ_c states are shown in Table 1.1 while their mass and radiative decay branching ratio is shown in Table 1.2.

As can be seen from Table 1.2 the mass difference between χ_{c1} and χ_{c2} is only about $45MeV$ thus separating the two resonances requires a very good resolution of the detector. On the other hand the χ_{c0} has a pretty low branching fraction in the radiative decay which makes its detection in this channel difficult.

While most experimental observations of charmonium production consist of J/ψ measurements, a significant contribution of J/ψ production is indirect, resulting from decay of higher mass states. In particular, the radiative decay of the χ_{cJ} states accounts for a significant fraction ($\sim 30-40\%$) of the prompt J/ψ production seen in hadronic collisions thus any calculation of J/ψ production must include χ_{cJ} production as well. This is one of the reasons why the study of χ_{cJ} resonances is relevant.

The measurement of the ratio $\sigma(pp \to \chi_{2c})/\sigma(pp \to \chi_{1c})$ represents also a benchmark for QCD theoretical models on meson production and decays.

1.3 Previous Studies of χ_c States at Hadronic Colliders

Measurements of hadronic χ_{cJ} production have been made in a variety of beam types and energies by observing the decay process $\chi_{cJ} \to J/\psi\gamma$. Experimental results before the Tevatron collider have suffered from large statistical uncertainties and no measurement has had the precision to test the consistency of the cross section ratio $\sigma_{\chi_{c2}}/\sigma_{\chi_{c1}}$ with the simple spin-state counting expectation of 5/3 for χ_{cJ} mesons that are directly produced in the interaction (i.e. promptly produced). At the Tevatron accelerator (in Fermilab) a measurement of the relative cross section times branching fractions of the χ_{c1} and χ_{c2} mesons produced in $p\bar{p}$ collisions at a center of mass energy of 1.96 TeV using the CDF II detector. The measure uses the inclusive process $p\bar{p} \to \chi_{cJ}X$, where $\chi_{cJ} \to J/\psi\gamma$ and $J/\psi \to \mu^+\mu^-$ in a data sample with a time integrated luminosity of $1.1fb^{-1}$. The final state photon is reconstructed through its conversion into e^+e^-, which provides the mass resolution needed to distinguish the χ_{c1} and χ_{c2} states. The spatial resolution of the $\mu^+\mu^-$ vertex allows separation of prompt χ_{cJ} production from events where χ_{cJ} meson is a B-hadron decay product. The ratio of the cross section times branching fraction $R_p = \sigma_{\chi_{c2}}\mathcal{B}(\chi_{c2} \to J/\psi\gamma)/\sigma_{\chi_{c1}}\mathcal{B}(\chi_{c1} \to J/\psi\gamma)$ for promptly produced χ_{cJ} mesons is measured.

In addition it is measured the analogous quantity in B decay events, $R_B = \sigma_B\mathcal{B}(B \to \chi_{c2}X)\mathcal{B}(\chi_{c2} \to J/\psi\gamma)/\sigma_B\mathcal{B}(B \to \chi_{c1}X)\mathcal{B}(\chi_{c1} \to J/\psi\gamma)$ thus obtaining a measurement of $\mathcal{B}(B \to \chi_{c2}X)/\mathcal{B}(B \to \chi_{c1}X)$ for the B hadrons produced in the Tevatron environment.

The full analysis strategy and candidate reconstruction is reported in [1]. Only the kinematic cuts used will be reported: the J/ψ candidate is required to have $p_T(J/\psi) > 4.0GeV/c$ and $|\eta(J/\psi)| < 1.0$, the photon candidate is required to have $p_T(\gamma) > 1.0GeV/c$.

An unbinned likelihood fit is used to calculate the yield of χ_{cJ} events for both prompt and B-decay production processes. The fit to the data gives an event yield ($N_{\chi_{cJ}}$) of $N_{\chi_{c0}} = 41 \pm 20$, $N_{\chi_{c1}} = 2143 \pm 60$ and $N_{\chi_{c2}} = 1035 \pm 40$ for promptly produced events. For B decay events, the yields are $N_{\chi_{c0}} = 29 \pm 16$, $N_{\chi_{c1}} = 384 \pm 35$ and $N_{\chi_{c2}} = 66 \pm 16$. The relatively small yield of χ_{c0} candidates is due to the small branching fraction into the radiative final state.

Acceptances and and reconstruction efficiencies of the final state have been studied

with a Monte Carlo simulation that generates events uniformly in rapidity with a transverse momentum distribution that matches the measured distribution of J/ψ events. The simulated events were processed through reconstruction and analysis algorithms and provided templates for the expected signal shape of the final state mass distribution.

In Figure 1.6 the values of the ratio for prompt (R_p) and B (R_B) components are reported for various p_T bins with their statistical errors. The efficiency ratio between the two resonances is also reported. In Figure 1.5 an evaluation of the systematic uncertainties is reported. Figure 1.3 shows the invariant mass distribution of the χ_c candidates while in Figure 1.4 the ct distribution is shown.

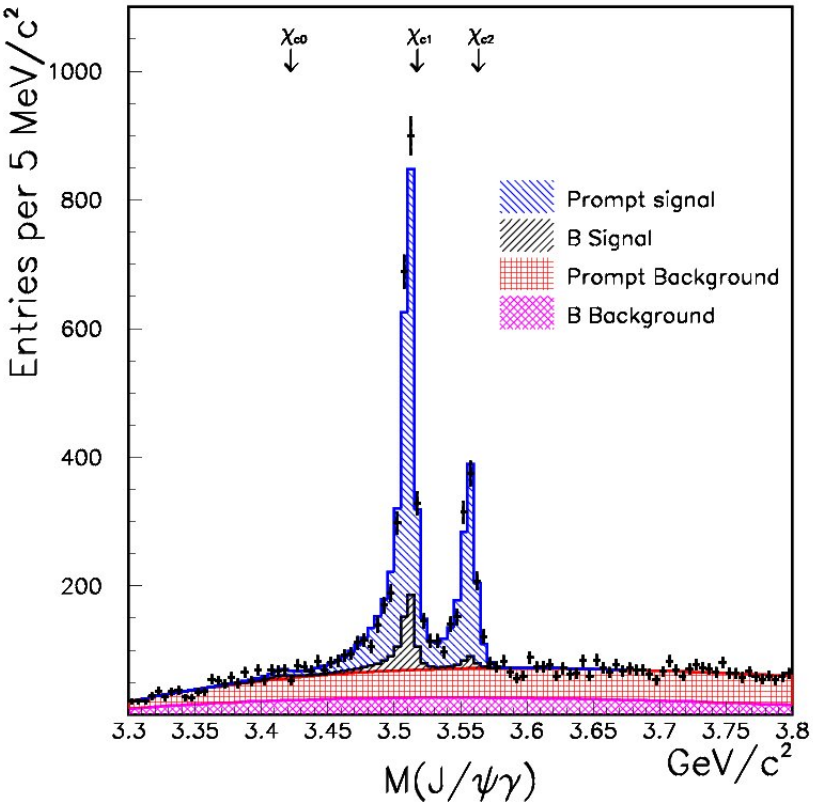

Figure 1.3: The $J/\psi\gamma$ mass distribution (points) with the projection of the likelihood fit overlaid on the data. The masses of the χ_{cJ} mesons and the contributions of the signal and background components are indicated [1].

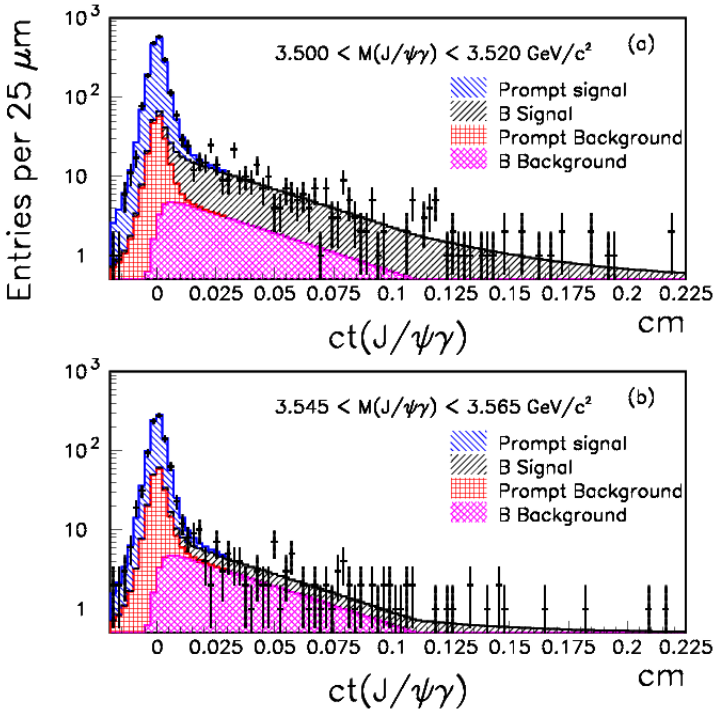

Figure 1.4: The ct distribution (points) for events in the χ_{c1} (a) and χ_{c2} (b) mass ranges. The projection of the fit is overlaid on the data, with the contribution of each signal and background component indicated [1].

Effect	Uncertainty
Simulation Sample Size	± 0.005
Photon Conversion Simulation	± 0.020
Polarization Effects	± 0.030
Invariant Mass Resolution	± 0.005
Prompt/B Separation	$\pm 0.002 (\pm 0.010$ for $B)$
Total	± 0.037 (± 0.038 for B)

Figure 1.5: Relative systematic uncertainties of R_p and R_B [1]

$p_T(J/\psi)$ (GeV/c)	$\epsilon_{\chi_{c2}}/\epsilon_{\chi_{c1}}$	R_p	R_B
$4-6$	1.27 ± 0.01	0.457 ± 0.039	0.150 ± 0.087
$6-8$	1.17 ± 0.01	0.384 ± 0.034	0.080 ± 0.094
$8-10$	1.14 ± 0.01	0.455 ± 0.053	0.116 ± 0.070
> 10	1.10 ± 0.01	0.309 ± 0.045	0.197 ± 0.082
> 4	1.23 ± 0.01	0.395 ± 0.016	0.143 ± 0.042

Figure 1.6: The acceptance ratio and ratios of cross section times branching fractions of the χ_{cJ} states for the prompt events and B decay events. Uncertainties listed are statistical only [1].

1.4 Agreement of Previous Measurement with Current Theory Prediction

The CDF Collaboration measured the ratio $R_{\chi_c} = \sigma_{\chi_{c2}}/\sigma_{\chi_{c1}}$ to be about 0.75 for $p_T > 4GeV$, the ratio becomes smaller at higher p_T. At leading order (LO) in α_S, NRQCD predicts the χ_c production cross sections to scale as $1/{p_T}^6$ in the Colour Singlet channels and scale as $1/{p_T}^4$ in the Colour Octet channel. Thus the Colour Octet contribution would dominate at large p_T predicting the ratio R_{χ_c} to be 5/3 as one would obtain from spin counting, which is much larger than the measured value 0.75. Meanwhile, the colour-evaporation model (CEM) predicts the ratio to be always 5/3 in all orders of α_S simply based on spin counting. It seems no existing theory agrees with the measured R_{χ_c}. However, according to [23], there could be a good chance for NRQCD to explain this puzzle, because the next-to-leading order (NLO) contributions in α_S will change the large p_T behaviour of cross sections. In particular, contributions of Colour Singlet channels scale as $1/{p_T}^4$ at NLO, dominant with respect to $1/{p_T}^6$ at LO. So it is necessary to study χ_{cJ} production at NLO to see how the value of R_{χ_c} can change at large p_T. The authors of [23] have thus studied the NLO QCD corrections to χ_{cJ} hadroproduction at the Tevatron and LHC including both Colour Singlet and Colour Octet. Some representative diagrams of χ_c hadroproduction involved in the calculations are shown in Figure 1.7. The result of the calculations are shown in Figure 1.8 and 1.9.

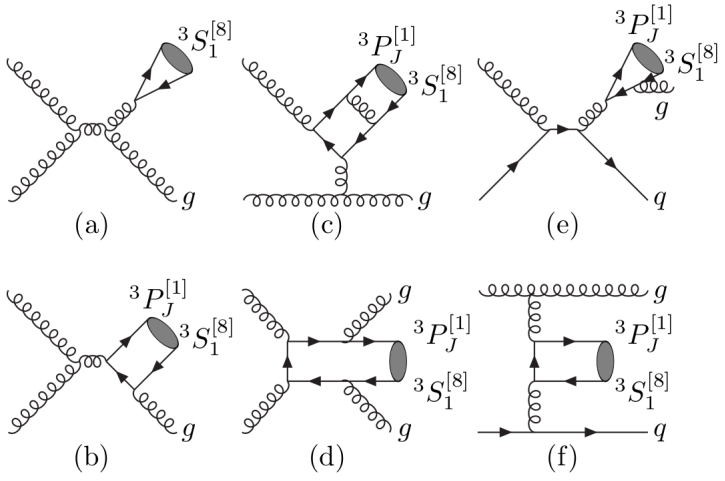

Figure 1.7: Representative Feynman diagrams for χ_{cJ} hadroproduction at LO and NLO. The gluon-gluon and gluon-quark subprocesses are all included. In both colour-singlet and colour-octet channels contribute [23].

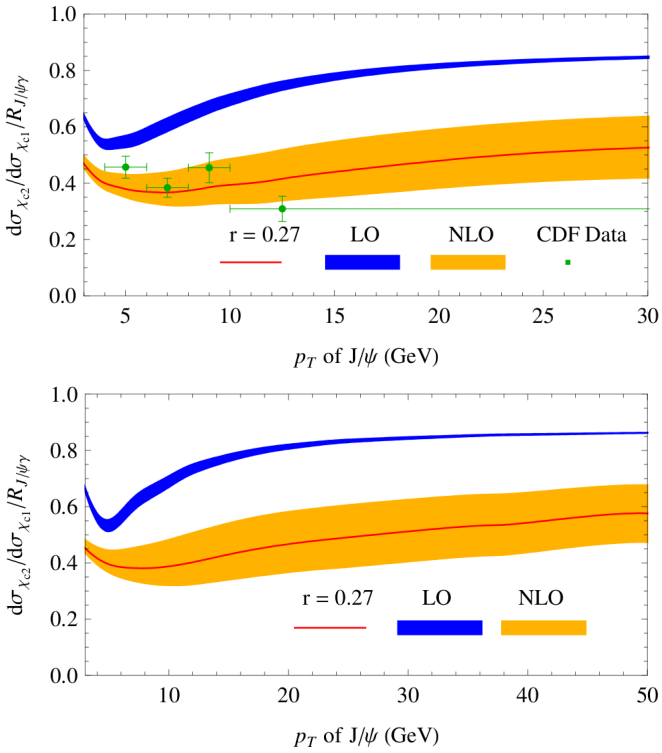

Figure 1.8: Top: transverse momentum distribution of ratio $R_{\chi_c}/R_{J/\psi\gamma}$ at the Tevatron with cut $|y_{\chi_{cJ}}| < 1$. The lower and upper bounds of LO and NLO are constrained by $0.24 < r < 0.33$.. Bottom: the same as above but for LHC with cut $|y_{\chi_{cJ}}| < 3$ [23]

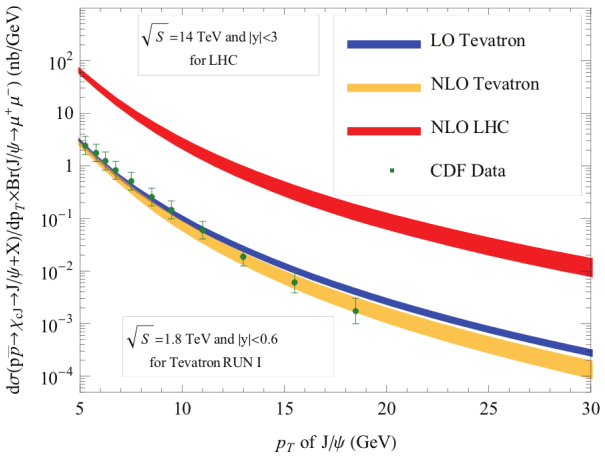

Figure 1.9: Transverse momentum distribution of χ_{cJ} feed down to J/ψ at the Tevatron RUN I and LHC [23]

The result of the calculation shows that Colour Singlet channels give large contributions at high p_T and the term for χ_{c1} decreases slower than the one for χ_{c2}, thus the measured ratio of R_{χ_c} at the Tevatron can be explained.

The simulation for Tevatron RUN I leads to a good agreement with data. As a result the observed rates of χ_{cJ} and ratio R_{χ_c} are explained simultaneously.

In χ_{cJ} production the NLO corrections already scale as $1/{p_T}^4$, which is the leading p_T behaviour, and the NNLO and other corrections are no longer important, because they are suppressed either by α_S or by v^2 (the relative velocity of quark and antiquark) relative to NLO contributions.

According to the authors of [23], this result shows that the measured R_{χ_c} disfavours CEM, but favours NRQCD giving strong support to the colour-octet mechanism, and providing further tests for NRQCD and heavy quarkonium production mechanisms.

Chapter 2

Large Hadron Collider

2.1 Introduction and Technical Details

The Large Hadron Collider is a proton-proton collider built at CERN on the French-Swiss border near the city of Geneva. As of late 2011 the Large Hadron Collider is the highest luminosity and highest energy hadron collider ever built. The LHC was built to explore the hidden sectors of the SM and in particular the Higgs mechanism, Standard Model possible supersymmetric extensions, to study heavy ions collisions, the quark gluon plasma and in general to probe particle physics at the TeV energy scale.

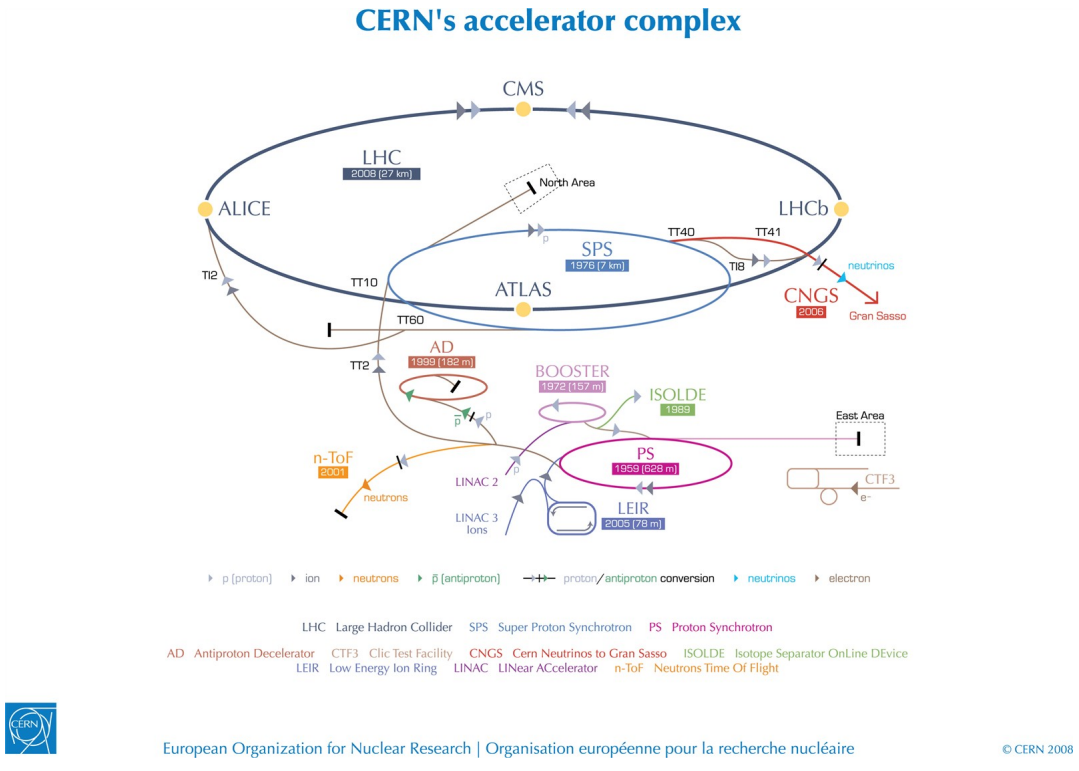

Figure 2.1: CERN accelerator complex and the LHC.

The need to investigate any new physics process up to the TeV scale requires a challenging machine, able to accelerate particles at high energy and to provide collisions with

high luminosity. These requirements dictated the main features of the machine:

- a hadron collider: the fundamental constituents entering in the scattering are the partons which carry a fraction x of the four-momentum of the particles in the beam. Therefore the center-of-mass energy of the hard scattering process $\sqrt{\hat{s}}$ can span several orders of magnitude. The design center of mass energy of LHC for proton-proton collisions is $\sqrt{s} = 14TeV$. In this way, partons momentum fractions $x_1, x_2 \simeq 0.15 - 0.20$ of the incoming protons momenta, give $\sqrt{\hat{s}} = \sqrt{x_1 x_2 s} \simeq 1 - 2TeV$ the energy range to be explored. With respect to an electron-positron machine, it is easier to accelerate protons to high energy since the energy lost for synchrotron radiation, proportional to γ^4 (where $\gamma = E/m$), is much lower than for the electrons.

- a proton-proton collider: with respect to a proton-antiproton machine, it is easier to accumulate high intensity beams of protons. Furthermore, the Higgs production process is dominated by gluon fusion, and therefore its cross section is nearly the same in proton-antiproton and proton-proton collisions.

- a high luminosity collider. The cross section σ determines the event rate R of a given process according to the formula $R = \mathcal{L}\sigma$. The factor $\mathcal{L}$ is called luminosity; it represents the number of collisions per unit time and cross-sectional area of the beams. It is specific to the collider parameters and does not depend on the interaction considered: $\mathcal{L} = f\frac{n_1 n_2}{A}$ where f is the collision frequency of bunches composed of n_1 and n_2 particles and A is the overlapping cross-sectional area of the beams. To compensate for the low cross section of the interesting processes the LHC must have a very high luminosity: the very short bunch crossing interval ($25ns$, frequency of $40MHz$) and the high number of bunches accelerated by the machine (2808 per beam) allows to reach the peak luminosity of $10^{34}cm^{-2}s{-}1 = 1nb^{-1}s^{-1}$. However this very high luminosity causes a faster radiation contamination of the detectors which negatively affects their efficiency and operation.

The idea behind the LHC is to reuse the existing 27 km long LEP tunnel to install the new collider. Here are reported design LHC parameters for pp and $PbPb$ ($^{208}Pb^{82+}$) collisions:

- Circumference: $26.659Km$
- Centre of mass energy: $14TeV$ per proton in pp collisions or $1148TeV$ per nucleus in $PbPb$ collisions.
- Dipole magnetic field: $8.3T$
- Number of particles per bunch: 2808 in pp collisions or 608 in $PbPb$ collisions
- Bunch length: $53mm$ in pp collisions or $75mm$ in $PbPb$ collisions.
- Bunch crossing rate: $40.08MHz$ in pp collisions or $0.0006MHz$ in $PbPb$ collisions.
- Design Luminosity: $10^{34}cm^{-2}s^{-1}$ in pp collisions or $2 \times 10^{27}cm^{-2}s^{-1}$ in $PbPb$ collisions.

- Beam radius at interaction point: $15\mu m$

The Large Hadron Collider posed new technological and engineering challenges to the scientific communities. In total, over 1,600 superconducting magnets are installed, weighing over 27 tonnes. Approximately 96 tonnes of liquid helium is needed to keep the magnets, made of copper-clad niobium-titanium, at their operating temperature of $1.9K$ ($-271.25°C$), making the LHC the largest cryogenic facility in the world at liquid helium temperature. In Figure 2.2 a section of the superconducting magnet can be seen.

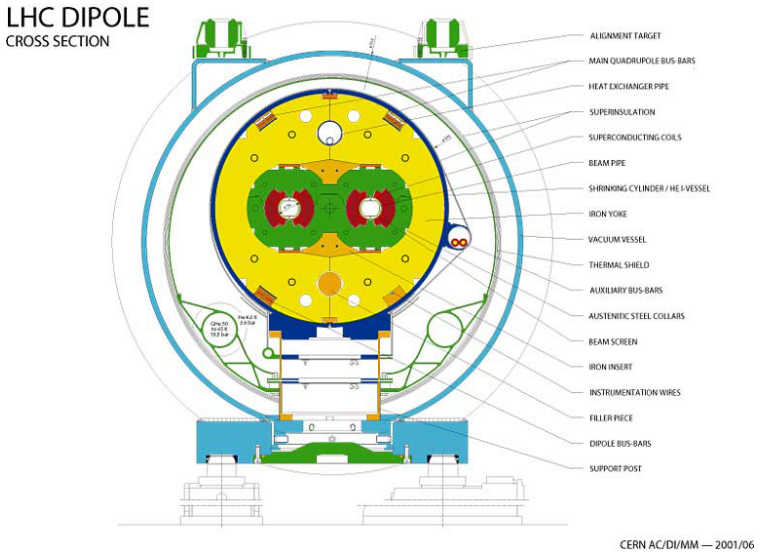

Figure 2.2: Section of LHC dipole.

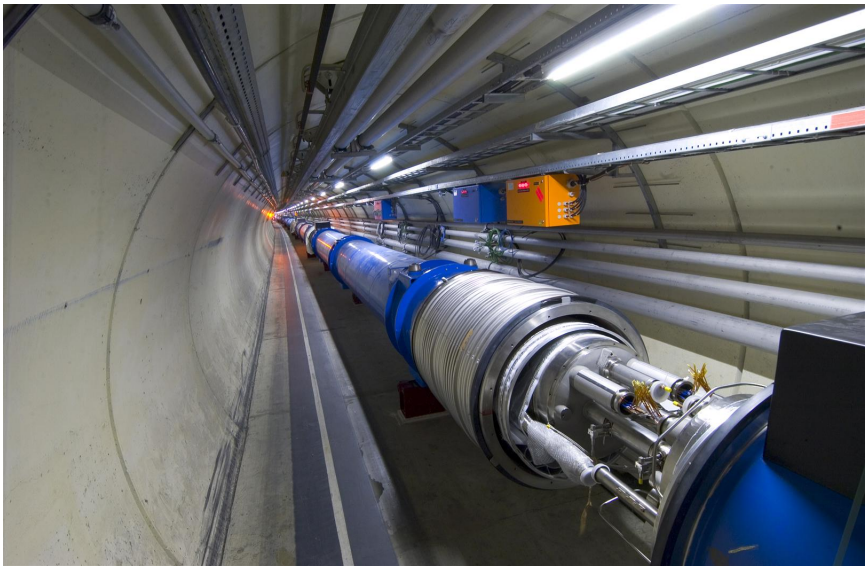

Figure 2.3: LHC magnet connection.

One very remarkable aspect of LHC physics is the overwhelming background rate compared to the interesting physics processes: the Higgs production, for instance, has a

cross section at least ten orders of magnitude smaller than the total inelastic cross section, as shown in 2.4. In fact, most of the events produced in pp collisions is either due to low p_T scattering, where the protons collide at large distance, or to QCD high p_T processes. All these events are collectively called minimum bias and they are in general considered not interesting since they constitute a background for other interesting processes, where massive particles like the Higgs are created in the hard scattering.

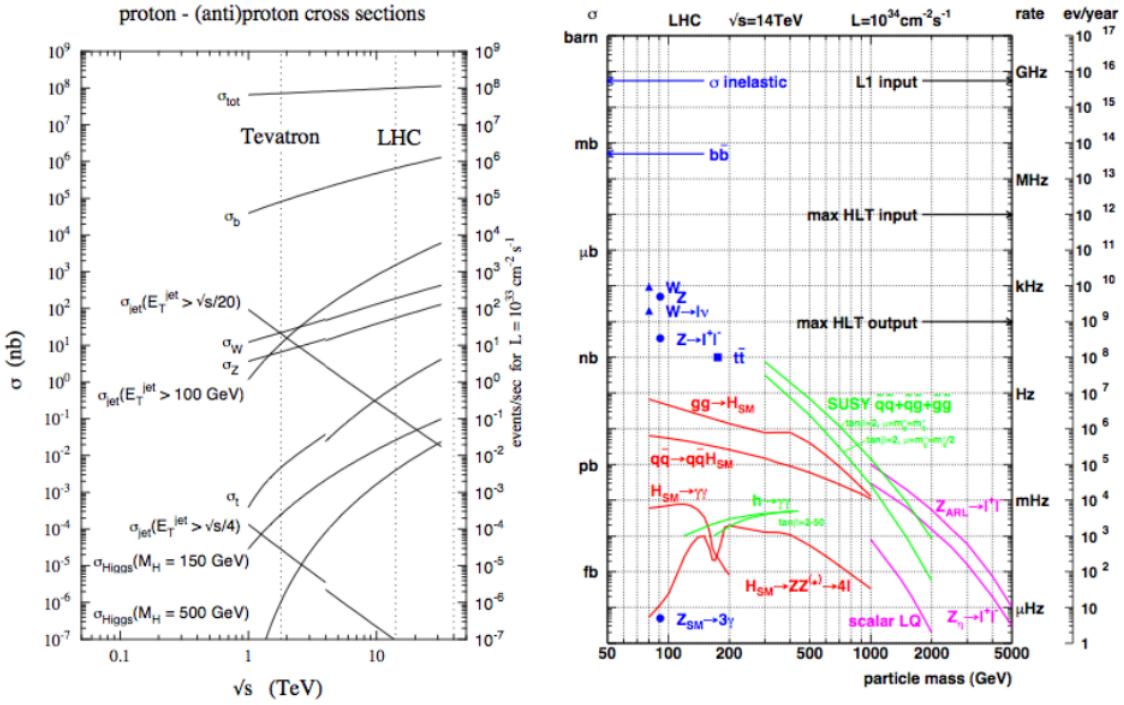

Figure 2.4: Cross section as a function of the center-of-mass energy (left) and rate of events at LHC as a function of the mass of the produced particle (right) for interesting processes [20].

Finally, the fact that the two partons interact with unknown energies implies that the total energy of an event is unknown. The proton remnants, that carry a good fraction of the proton energy, are scattered at small angles and are mostly lost in the beam pipe, escaping undetected. Experimentally, it is therefore not possible to define the total and missing energy of the event, but only the total and missing transverse energies. Thus, all the interesting physics observable are measured in the plane transverse to the beamline.

The first beam was circulated through the LHC 10 September 2008. CERN successfully fired the proton beam around the tunnel in stages, however shortly after, on 19 September 2008, a quench occurred in about 100 bending magnet causing a loss of approximately six tonnes of liquid helium, which was vented into the tunnel. Most likely the cause of the problem was a faulty electrical connection between two magnets. A total of 53 magnets were damaged in the incident and were repaired or replaced during the winter shutdown, however almost a year passed before the LHC was put in function again. Due to this accident the LHC is now running with a reduced energy of collisions $\sqrt{s} = 7TeV$ instead of the project nominal energy of $\sqrt{s} = 14TeV$.

According to the plans, LHC will run with $\sqrt{s} = 7TeV$ center of mass energy for the whole 2012, then there will be a shutdown for at least one year to technically prepare LHC for running at $\sqrt{s} = 14TeV$. Such stop is needed make sure that accidents like the one happened in 2008 won't repeat.

During this time the various detectors installed at LHC may install upgrades to their subdetectors systems to improve their performance in view of the higher energy, higher luminosity runs.

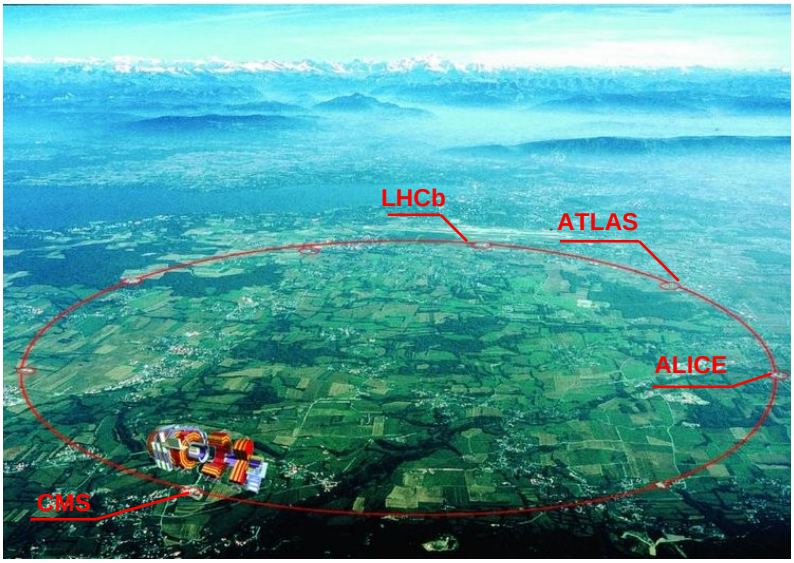

Figure 2.5: Aerial view of the LHC area and interaction points.

The Large Hadron Collider is the host of six different experiments; each experiment has a different composition and geometry of the subdetectors so that it is more specialized in a particular area of the research in particle physics. ATLAS (A Toroidal Lhc ApparatuS) and CMS (Compact Muon Solenoid) are two general-purpose, high-luminosity detectors; they are built with a cylindrical geometry around the beamline. Even if theoretically "general-purpose" detectors these two have been designed with the discovery of new physics in the TeV scale, thus their subdetectors are optimized for the reconstruction of high energy objects with great efficiency and accuracy. These two detectors will be able to measure masses of new particles produced by collisions up to 3-4 TeV. While similar in their purposes, the design of the two detectors differs significantly, since different solutions were chosen for the configuration of the magnetic field. ATLAS uses a toroidal field produced by three sets of air-core toroids complemented by a small solenoid in the inner region, while CMS uses a solenoidal field generated by the world's largest superconducting solenoid.

ALICE (A Large Ion Collider Experiment) is a detector optimized for PbPb collisions, in particular for the study of the properties of matter at high temperature and high energy density generated by such collisions (Quark Gluon Plasma). LHCb is specialized in studies regarding the physics of heavy quarks and heavy mesons with a particular attention to the b quark and its mesons.

TOTEM and LHCf are forward detectors of CMS and ATLAS repectively, they are placed $\sim 100m$ from the interaction points of the main experiments to study diffractive

physics happening in the very forward region of the collision. These detectors were to be put far from the interaction point so that the products of such very forward (i.e. high η, small angle with respect to the beamline) inelastic or elastic collisions may exit the beampipe.

Further details about LHC can be found here [20].

2.2 Physics at LHC: Early Searches and Future Perspectives

In these first two years of operations during pp collisions, the LHC experiments have started their physics program by measuring a wide range processes, beginning with large cross section processes useful to gain knowledge of the detector and perform needed calibrations with a large number of recorded events despite the low integrated luminosity. This process of "re-discover" the standard model include the measurement of observables such as the electroweak boson production cross sections, needed in a latter phase for more refined analysis of LHC data. Among the most significant results there are also the measurement of the top quark production cross section, the measurement of its mass, and measurements in the sector of B-hadron physics. A brief description of "rediscovering" of standard model analyses and their usefulness in search physics beyond the standard model will follow.

- Vector gauge boson production: the cross sections of W and Z bosons production at LHC are huge with respect to previous experiment: at $\sqrt{s} = 14TeV$ the cross sections are $\sigma(pp \to W \to l\nu) \simeq 20nb$ and $\sigma(pp \to Z \to l\bar{l}) \simeq 2nb$. These processes are important during the first data taking at LHC allowing to test the detector performances, perform alignment of the muon system and of the inner tracker and to tune the Monte Carlo codes used to simulate the physics processes. The study of Z and W events will also improve the knowledge of the Parton Distribution Functions at LHC energies.

- Top quark physics: The two most important measurements regarding top physics are the production cross section and the mass. The most promising channel for the measurement of the top mass is $t\bar{t} \to W^+W^-b\bar{b}$.

- B-physics and CP-violation: LHC can benefit from a very large $b\bar{b}$ production cross section. The main interest is the study of the decays of neutral B mesons, and in particular of the CP violation in the $B_d^0 - \bar{B}_d^0$ and $B_s^0 - \bar{B}_s^0$ system. B decays can be identified in final states containing leptons. However these leptons are usually low p_T and the identification is difficult due to the high backgrounds, pile-up and low efficiency.

A brief summary of the main searches for new physics and physics beyond the standard model will follow. These kind of searches require an high integrated luminosity and high energy of collisions so there may be the need of many years of data taking with high instantaneous luminosity to have conclusive results about these searches.

- The Higgs boson search: The main process of production of the Higgs boson in hadron collision is the so called "gluon fusion" $gg \to H$ obtained through a quark loop. There are a variety of decay channels containing leptons, jets and neutrinos in the finals state, however the two most promising channels are $H \to \gamma\gamma$ and $H \to ZZ \to l\bar{l}l\bar{l}$. Both channels have a fair branching ratio and are relatively good in terms of signal over background ratio with respect to other final states.

  Higgs boson searches require a huge amount of integrated luminosity to give conclusive results. Especially hard is the to probe is the low mass Higgs boson $(120 - 140GeV)$ since the signal over background ratio gets worse at lower energies. So far this seems to be the most promising mass range for the Higgs boson.

  Further information about Higgs searches at LHC can be found here [19].

- Supersymmetry (SUSY): is a theory that introduces a new symmetry between bosons and fermions. SUSY predicts that each particle has a supersymmetric partner whose spin differs by one half.The simplest supersymmetric model, called the Minimal Supersymmetric Standard Model (MSSM), predicts the existence of two Higgs doublets, corresponding to five Higgs particles: two charged bosons, two scalar bosons and one pseudo-scalar. The observation of MSSM Higgs bosons relies on the identification the leptons coming from τ decays and of τ-jets [10]. As the signal (if present at all) could be pretty faint a very precise modelling and tuning of the Standard Model background from Montecarlo is needed.

- Search for new massive vector bosons: These are high-mass objects decaying in leptons such as $Z' \to e^+e^-$ and $Z' \to \mu^+\mu^-$. The discovery of an object like a Z' boson will be very likely limited by the statistical significance of the signal. For these kind of searches a good momentum resolution at high p_T is needed to determine correctly the sign of the leptons.

Chapter 3

CMS Experiment

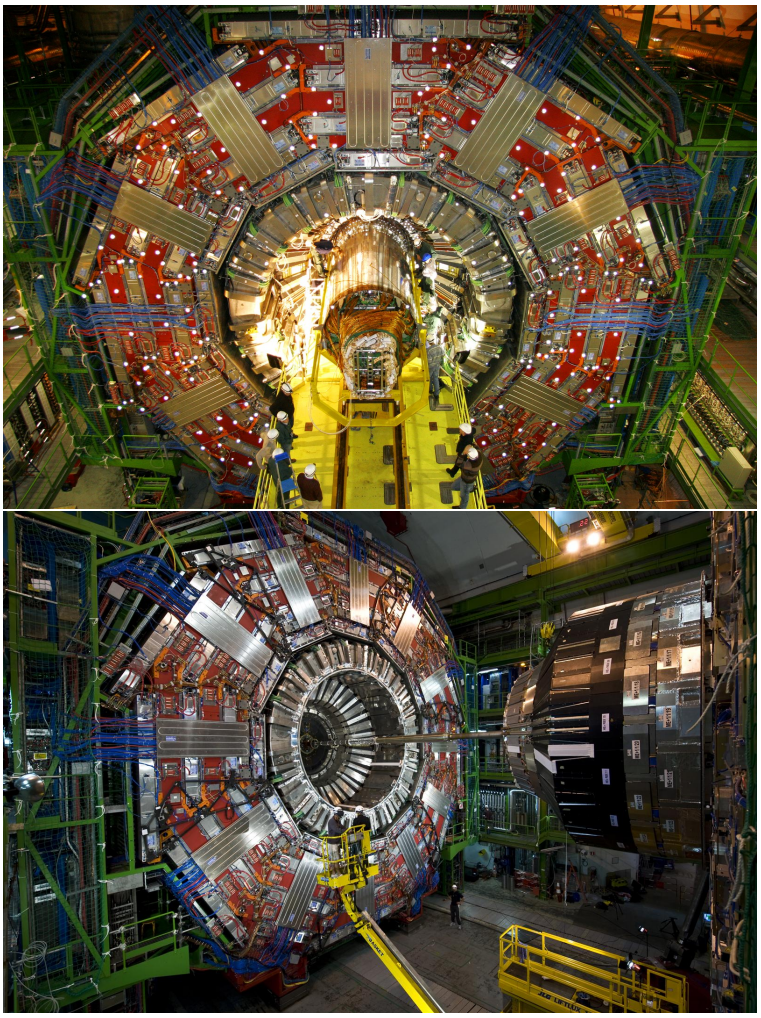

Figure 3.1: Two views of the CMS detector before closing.

As stated before, among the main goals of the LHC machine there is the study of the electroweak symmetry breaking mechanism and the search for physics beyond the Standard Model, to fulfil this goal the most important requirements are:

- good muon identification and momentum resolution over a wide range of momenta in the region $|\eta| < 2.5$. The charge of muons should be determined without ambiguity for momenta up to 1 TeV;
- good dimuon mass resolution (about 1% at 100 GeV);
- good charged particle momentum resolution and reconstruction efficiency in the tracking system together with efficient triggering and offline tagging of tau leptons and b-jets;
- good electromagnetic energy resolution, good diphoton and dielectron mass resolution, measurement of the direction of photons and correct localization of the primary interaction vertex, π_0 rejection and efficient photon and lepton isolation at high luminosities;
- good missing energy and dijet mass resolution, using hadron calorimeters with a large hermetic geometric coverage ($|\eta| < 5$) and with fine lateral segmentation.

The main layout of the CMS detector is shown in figure 3.2. The final design of the detector allows a reliable identification and precise measurement of the muon momentum by means of a redundant muon identification system (tracking system and muon chambers), a precise measurement of photons and electrons energy with a high resolution calorimeter system and an excellent reconstruction of the charged particle tracks and measurement of their momentum resolution thanks to a high quality tracking system. The inner tracking system allows also a precise localisation of the primary vertex of interaction, which is an essential feature in the scenario of high luminosity collisions causing high pileup of events.

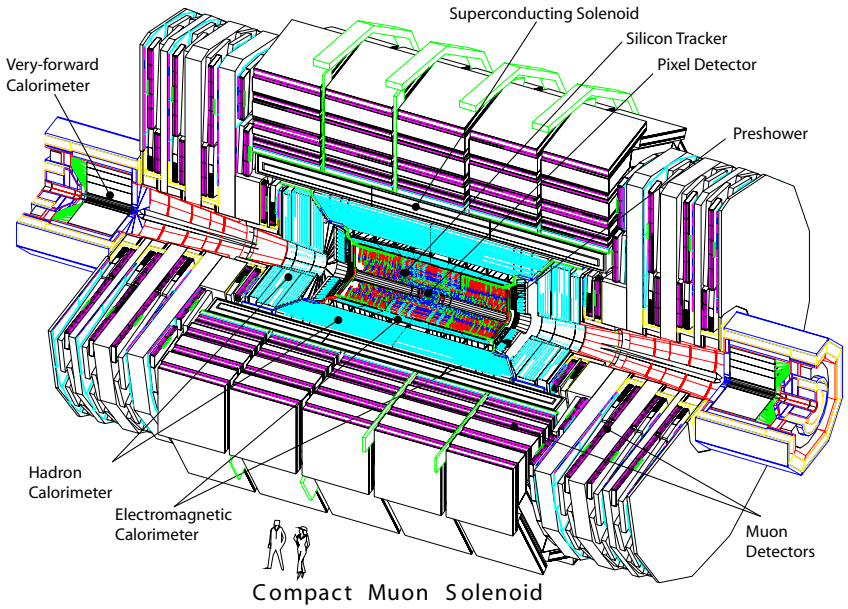

Figure 3.2: CMS detector structure [6].

The detector structure consists of a cylindrical barrel closed by two endcap disks. The overall length is $21.6m$, the diameter $14.6m$ and the total weight about 12500 tons. The thickness of the detector in radiation lengths is greater than $25X_0$ for the electromagnetic calorimeter, and the thickness in interaction lengths varies from 7 to 11 λ_I for the hadronic calorimeter, depending on the η region. For a particle carrying quadrimomentum (E, p_x, p_y, p_z), the momentum vector p can be divided in two components: the longitudinal momentum p_z and the transverse momentum defined as $p_T = \sqrt{{p_x}^2 + {p_y}^2}$. The rapidity is defined as:

$$y = \frac{1}{2} \log \left(\frac{E + p_z}{E - p_z} \right) \tag{3.1}$$

Being invariant under boost of the centre-of-mass along the z direction, the rapidity is used for describing angular distribution of momentum of particles. For an ultra-relativistic particle ($p \gg m$) y can be approximated to the pseudorapidity :

$$\eta = -\log \left(\tan \frac{\theta}{2} \right) \tag{3.2}$$

were θ is the angle between the particle momentum p and the z axis. The specific choice of a solenoidal magnetic field led to a very compact design for the CMS system with respect to, for example, the ATLAS design. This allowed the calorimeters to be installed inside the magnet, with a strong improvement in the detection and energy measurement of electrons and photons. In particular the almost constant magnetic field inside the solenoidal magnet makes the momentum measurement easier and thus much more precise, with repect to, for example, a non spatially constant magnetic field. Moreover, tracks exiting the yoke point back to the interaction point, useful for track reconstruction. The downside of this design is that muons passing through the magnet and its return yoke experience multiple scattering effects thus affecting negatively the performance of the muon chambers. The longitudinal view of one quarter of CMS and the transverse view of the barrel region are shown in Figure 3.3.

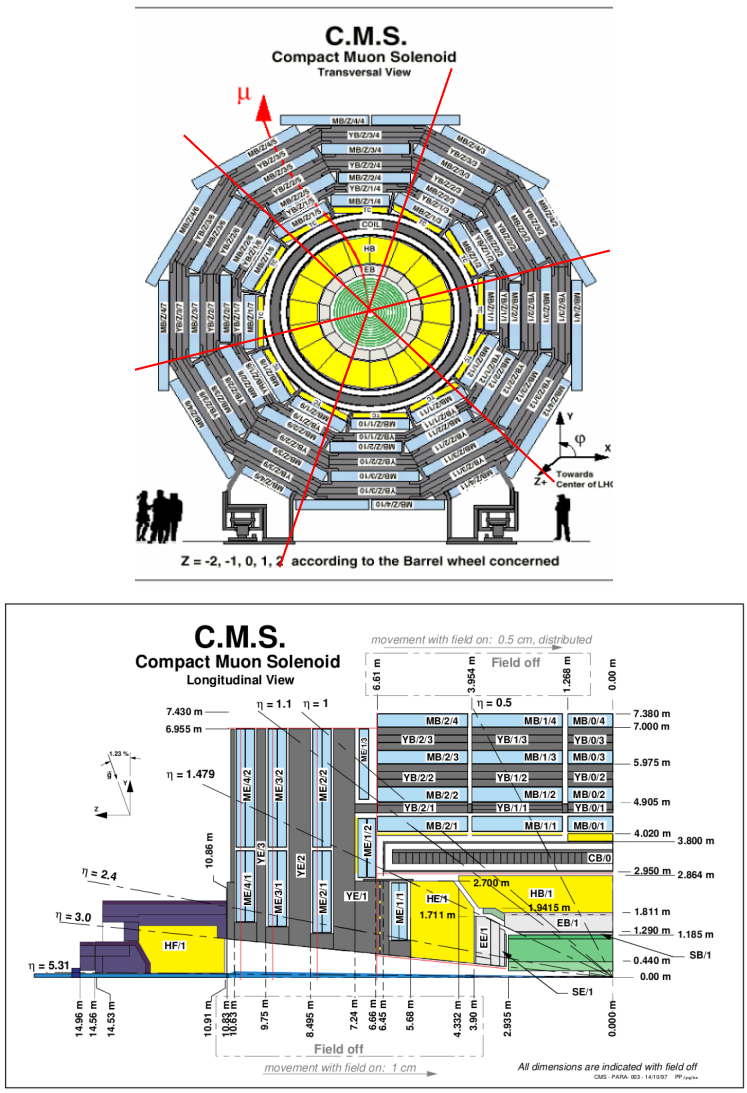

Figure 3.3: Section and side view of the CMS detector [6].

The core of the apparatus is the magnet (CB), a $13m$ long super-conductive solenoid cooled with liquid helium, which provides a $3.8T$ magnetic field. The magnet coil has a diameter of $5.9m$ and contains the Tracker, the electromagnetic and hadronic calorimeters. The iron return yoke of the magnet (YB, YE) hosts the muon spectrometer, composed by 4 stations of drift tube detectors (DT) in the barrel region (MB) and 4 stations of cathode strip chambers (CSC) in the endcaps (ME). Both the barrel and the endcaps are equipped with resistive plate chambers (RPC) which ensure redundancy and robustness at the muon trigger system. The overall pseudorapidity coverage of the muon system goes up to $|\eta| = 2.4$. The hadronic calorimeter (HCAL) is a brass/scintillator sampling calorimeter. The barrel and endcap parts (HB and HE) have the same pseudorapidity coverage as the electromagnetic calorimeter, and are complemented by a very forward calorimeterm(HF), which extends the coverage up to $|\eta| < 5.3$. Inside HCAL, the electromagnetic calorimeter (ECAL) is installed: it is an homogeneous calorimeter made of

lead tungstate ($PbWO_4$) scintillating crystals. The pseudorapidity coverage extends up to $|\eta| < 3.0$. In the endcaps a lead/silicon pre-shower detector is installed to improve the resolution on electron and photon direction and help π rejection.

The tracking detector is placed in the core of CMS: its design was driven by the requirement of a precise vertex reconstruction and a reliable b-tagging with very high track multiplicity. To achieve this goal very fine segmentation is crucial. The choice of CMS was to employ 10 layers of silicon microstrip detectors, which provide the required granularity and precision. In addition, 3 layers of silicon pixel detectors are placed close to the beampipe an the interaction region in order to improve the measurement of the position of primary and secondary vertices. The tracking device allows charged particle tracks reconstruction with at least 12 detector hits and a coverage of $|\eta| < 2.5$.

More detailed technical information on the CMS detector and its subdetectors can be found in [6], [4], [13], [5], [12].

3.1 Tracking System

The tracking system is the core of the CMS detector and it's essential for the reconstruction of the physical object produced by collisions.

In a proton collider the longitudinal momentum of the interacting partons $p_z = p \cdot \cos(\theta)$ is not exactly known for every event (only on a statistical basis), and the measurement of the physics observables is thus usually performed in the transverse plane. Therefore, it becomes essential to measure the transverse momentum $p_T = p \cdot \sin(\theta)$ with a very high resolution. The trajectory of a particle with transverse momentum p_T and charge $Q = ze$ inside a magnetic field B is an helix, with radius R. The relation among these quantities is:

$$p_T = 0.3 \cdot z \cdot B \cdot R \tag{3.3}$$

where p_T is expressed in GeV, B in T e R in m. What is experimentally measured is the radius R, or better, the curvature $k = Q/R$. The distribution of the measurements is gaussian, and the error can be written as the sum in quadrature of two contributions, the resolution on the measurement (δk_{res}) and the multiple Coulomb scattering ($deltak_{ms}$):

$$\delta k = \sqrt{\delta k_{res}^2 + \delta k_{ms}^2} \tag{3.4}$$

Parametrizing the formula in terms of p_T, the particle transverse momentum resolution can be written as:

$$\frac{\delta p_T}{p_T} = C_1 p_T \oplus C_2 \tag{3.5}$$

where the term C_2 contains the multiple Coulomb scattering effects, while the angular coefficient C_1 depends on the detector geometry, in particular from the number of points used for the track reconstruction (n), its length (L), and the resolution on the single point measurement (σ_x):

$$C_1 \propto \frac{\sigma_x}{\sqrt{n} \cdot B \cdot L^2} \tag{3.6}$$

For low energetic particles C_2 dominates. C_1 is minimized having a long Tracker detector, and a consistent number of points n in the track fit. The resolution σ_x on a single

measured point is given by:

$$\sigma_x = \sqrt{\sigma_{int}^2 + \sigma_{syst}^2} \tag{3.7}$$

where σ_{int} is the intrinsic resolution of the detectors and σ_{syst} the systematic error given by the unknown spatial position of hit module: this last one can be minimized by alignment procedures.

The major requirements for the CMS Tracker can be summarized in the:

- promptness in the response, given the high track population during the nominal LHC collisions of one (plus pile-up) event every $25ns$;
- robustness of its components to the radiation exposure, given the high density of hadronic tracks up to $10^{14} n_e q \cdot cm^{-2}$, where $n_e q$ are "equivalent" $1MeV$ neutrons;
- minimization of the crossed material, with the aim of reducing the multiple Coulomb scattering of charged particles crossing the detector, photon conversion and electron energy loss via Bremsstrahlung;
- perfect alignment, internal of its components and with the muon system, in order to provide a reliable measurement of the particle momentum.

The CMS Tracker detector was designed in order to fulfill these requirements, giving at its nominal performance:

- reconstruction capability in the region $|\eta| < 2.5$ with an efficiency of at least 95% for charged tracks with $p_T > 10GeV$;
- high momentum resolution for isolated tracks:

$$\frac{\delta p_T}{p_T} = (1.5 \cdot p_T \oplus 0.5)\% for |\eta| < 1.6 \tag{3.8}$$

$$\frac{\delta p_T}{p_T} = (6.0 \cdot p_T \oplus 0.5)\% for |\eta| < 2.5 \tag{3.9}$$

  where the p_T is expressed in TeV. As shown in Figure 3.4 adding the information from the muon system, the resolution, for $p_T > 0.1TeV$ muons, becomes:

$$\frac{\delta p_T}{p_T} = (4.5\% \cdot \sqrt{p_T}) \tag{3.10}$$

- high resolution for transverse impact parameter, $\sigma(d_{xy}) = 35\mu m$ and longitudinal impact parameter $\sigma(d_z) = 75\mu m$.

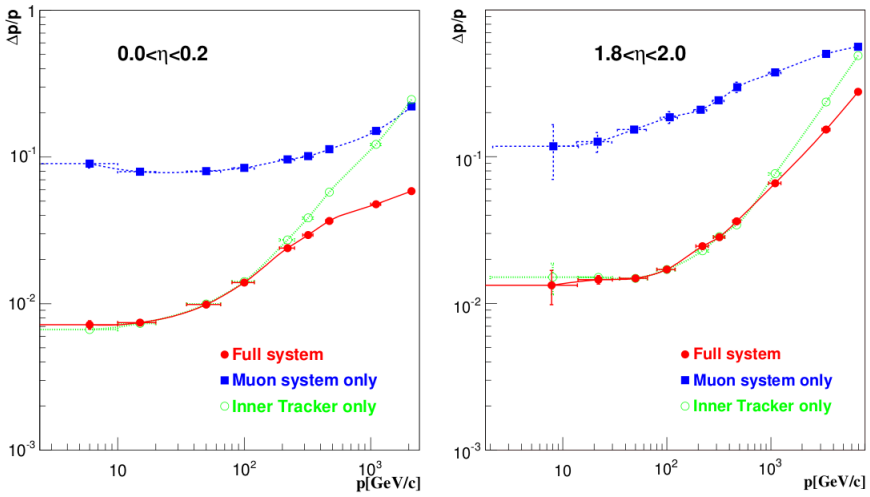

Figure 3.4: Expected momentum resolution of muons as a function of momentum p, using measurements of the muon system only (blue), the Tracker only (green) or both detectors (red). Left. Central region $0 < \eta < 0.2$. Right. Forward endcap region $1.8 < \eta < 2.0$ [6].

The CMS collaboration decided to build the whole detector using a silicon detector technology. This type of detector provides a low spatial resolution, from $10\mu m$ to $20\mu m$ and a fast collection of the charge deposited on the sensible elements, below $10ns$. The Tracker covers the pseudorapidity region $|\eta| < 2.5$ with a radius ranging between $4.3cm$ and $120cm$ in the z interval between $-270cm$ and $270cm$. The innermost region is made of pixel detectors, while the outermost one is built with strip detectors.

3.1.1 The Pixel Detector

The pixel Tracker consists of three $53.3cm$ long barrel layers and two endcap disks on each side of the barrel section, as shown in 3.5. The innermost barrel layer has a radius of $4.4cm$, while for the second and third layer the radii are $7.3cm$ and $10.2cm$, respectively. The layers are composed of modular detector units (called modules) placed on carbon fiber supports (called ladders). Each ladder includes eight modules, consisting of thin ($285\mu m$), segmented silicon sensors with highly integrated readout chips (ROC) connected by Indium bump-bonds. Each ROC serves a 52×80 array of $150\mu m \times 100\mu m$ pixels. The Barrel Pixel (BPIX) region is composed of 672 full modules and 96 half modules, each including 16 and 8 ROCs, respectively. The number of pixels per module is 66560 (full modules) or 33280 (half modules). The total number of pixels in the barrel section is 47923200.

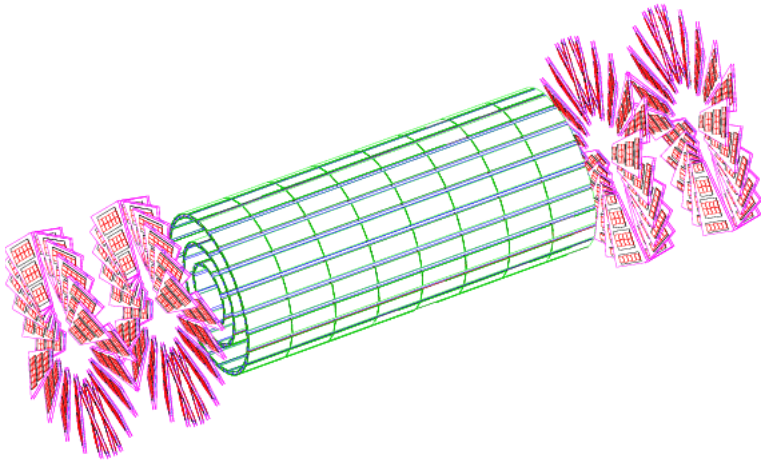

Figure 3.5: Schematic illustration of the pixel tracker. [6]

The Forward Pixel (FPIX) endcap disks, extending from $6cm$ to $15cm$ in radius, are placed at $z = \pm 35.5cm$ and $z = \pm 48.5cm$. Disks are split into half-disks, each including 12 trapezoidal blades arranged in a turbine-like geometry. Each blade is a sandwich of two back-to-back panels. Rectangular sensors of five sizes are bump-bonded to arrays of ROCs, forming the so-called plaquettes. Three (four) plaquettes are arranged on the front (back) panels with overlap to provide full coverage for charged particles originating from the interaction point. The endcap disks include 672 plaquettes ($270\mu m$ thick), for a total of 17971200 pixels. The minimal pixel cell area is dictated by the readout circuit surface required for each pixel. In localizing secondary decay vertices both transverse ($r\phi$) and longitudinal (z) coordinates are important and a nearly square pixel shape is adopted. Since the deposited charge is often shared among several pixels, an analog charge readout is implemented. Charge sharing enables interpolation between pixels, which improves the spatial resolution. In the barrel section, the charge sharing in the $r\phi$-direction is largely due to the Lorentz effect. In the endcap pixels, the sharing is enhanced by arranging the blades in the turbine-like layout.

3.1.2 The Strip Detector

Outside the pixel detector, the Tracker (see Figure 3.6) is composed of 10 layers of silicon microstrip detectors. The barrel region ($|\eta| < 1.6$) is divided into two parts: the Tracker Inner Barrel (TIB), covering $20 < r < 60cm$ and the Tracker Outer Barrel (TOB), covering $60 < r < 120cm$. The TIB is composed by four layers of p-on-n type silicon sensors with a thickness of $320\mu m$ and strip pitches varying from $80\mu m$ to $120\mu m$. The first two layers are made with double sided modules, composed by two detectors mounted back to back with the strips tilted by $100mrad$. This kind of sensors provides a measurement in both $r\phi$ and $r - z$ coordinates with a single point resolution between $23 - 34\mu m$ and $230\mu m$ respectively. The TOB is made of six layers. In this region the radiation levels are smaller and thicker silicon sensors ($500\mu m$) can be used to maintain a good signal-to-noise ratio for longer strip length. The strip pitch varies from $120\mu m$ to $180\mu m$. Also the first two layers of the TOB provide a stereo measurement with a single point resolution which varies from $35\mu m$ to $52\mu m$ in the r direction and $530\mu m$ in z. The

endcap region ($|\eta| > 1.6$) is covered by the Tracker Inner Disks (TID) and Tracker End Cap (TEC). The three disks of the TID fill the gap between the TIB and the TEC while the TEC comprises nine disks that extend into the region $120cm < |z| < 280cm$. Both subdetectors are composed of wedge shaped modules arranged in rings, centred on the beam line, and have strips that point towards the beam line (radial topology).

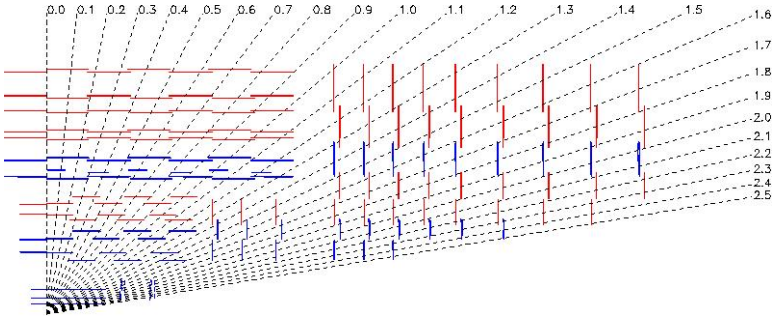

Figure 3.6: Schematic view of the strip tracker. [6]

3.2 Electromagnetic Calorimeter

The goal of the electromagnetic calorimeter is the accurate measurement of the energy and position of electrons and photons. The physics process that imposes the strictest requirements on its performance is the low mass ($mH \simeq 120 - 140GeV$) Higgs decay into two photons $H \to \gamma\gamma$. This is a very promising channel for Higgs searches because of the good signal over background ratio. The goal is 1% resolution on the diphoton invariant mass. The natural choice to achieve this task is a homogeneous calorimeter.

The ECAL is composed of 75,848 finely segmented lead tungstate ($PbWO_4$) crystals chosen because of their excellent energy resolution. Lead tungstate is a fast, radiation-hard scintillator characterised by a small Moliere radius ($R_M = 1.9mm$) e and a short radiation length ($X_0 = 8.9mm$), that allows good shower containment in the limited space available for the detector. Moreover, these crystals are characterised by a very short scintillation decay time that allows the electronics to collect about 80% of the light within $25ns$. A pre-shower detector is installed in front of the endcaps, consisting of two lead radiators and two planes of silicon strip detectors, with a total radiation length of $3X_0$. It allows rejection of photon pairs from π_0 decays and improve the estimation of the direction of photons, to improve the measurement of the two-photon invariant mass. The geometric coverage of the calorimeter extends up to $|\eta| = 3.0$, as shown in 3.7. The crystals are arranged in a $\eta - \phi$ grid in the barrel and a $x - y$ grid in the endcaps and they are almost pointing to the interaction point: the axes are tilted a 3° in the barrel and at $2° - 5°$ in the endcaps with respect to the line from the nominal vertex position.

Contribution	Barrel($\eta = 0$)	Endcap($\eta = 2$)
Stochastic term a	2.7%	5.7%
Noise (low luminosity) b	$0.155GeV$	$0.205GeV$
Noise (high luminosity)	$0.210GeV$	$0.245GeV$
Constant term c	0.55%	0.55%

Table 3.1: Different contributions to the energy resolution of ECAL

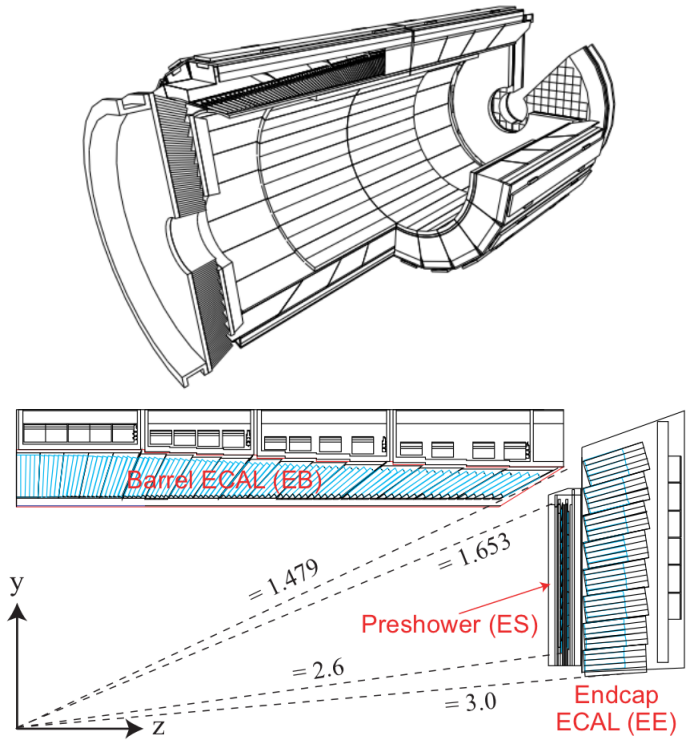

Figure 3.7: Schematic view of the Electromagnetic Calorimeter [6]

The energy resolution of a calorimeter is usually parameterized as:

$$\left(\frac{\sigma_E}{E}\right)^2 = \left(\frac{a}{\sqrt{E}}\right)^2 + \left(\frac{b}{E}\right)^2 + c^2 \tag{3.11}$$

where a is the stochastic term and it includes the effects of fluctuations in the number of photo-electrons as well as in the shower containment, b is the noise from the electronics and pile-up and c is a constant term related to the calibration of the calorimeter. The values of the three constants measured on test beams are reported in Table 3.1. The different contributions as a function of the energy are shown in Figure 3.8.

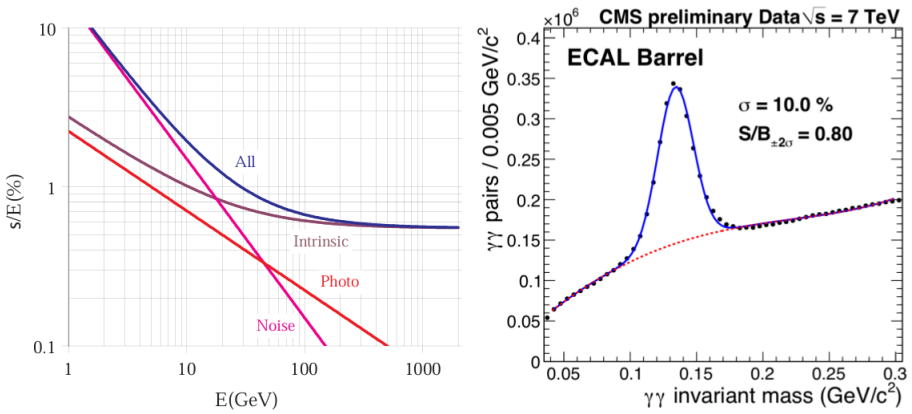

Figure 3.8: Left: Different contributions to the energy resolution of the ECAL. Right: diphoton invariant mass spectrum reconstructed by ECAL with about $250nb^{-1}$ of data at. The π_0 peak is visible, the mass resolution is of the order of 10% [6].

3.3 Hadron Calorimeter

The goal of the hadron calorimeter is to measure the direction and energy of hadronic jets, the total transverse energy and the missing transverse energy (MET) of the event. High hermeticity is required for this purpose, which means the subdetector must cover a portion of the solid angle as big as possible. For this reason, the barrel and endcap parts installed inside the magnet are complemented by a very forward calorimeter which is placed outside the magnet return yokes, with a total coverage of $|\eta| < 5.3$. The barrel and endcap HCAL cover the region $|\eta| < 3.0$. They are sampling calorimeters, whose active elements are plastic scintillators interleaved with brass absorber plates and read out by wavelength-shifting fibres. The first layer is read out separately, while all others are read out together. The absorber material has been chosen for its short interaction length, and its non-magnetic property. Both barrel and endcap are read-out in towers with a size of $\Delta\eta \times \Delta\phi$.

In the barrel, full shower containment is not possible within the magnet volume, and an additional tail catcher is placed outside the magnet consisting of an additional layer of scintillators. The projective depth in terms of nuclear absorption length goes from $5.1\lambda_I$ at $\eta = 0$ to $9.1\lambda_I$ at $\eta = 1.3$ and $10.5\lambda_I$ in the endcap. The very forward calorimeter is placed outside the magnet yoke, $11m$ from the interaction point. The active elements are quartz fibres parallel to the beam, inserted in steel absorber plates. The signal originated from quartz fibres is Cerenkov light.

The expected energy resolution (E in GeV) is $\sigma/E \simeq 65\%\sqrt{E} \oplus 5\%$ in the barrel, $\sigma/E \simeq 85\%\sqrt{E} \oplus 5\%$ in the endcaps and $\sigma/E \simeq 100\%\sqrt{E} \oplus 5\%$ in the very forward calorimeter.

3.4 Magnet and Muon Detection System

3.4.1 The Superconducting Magnet

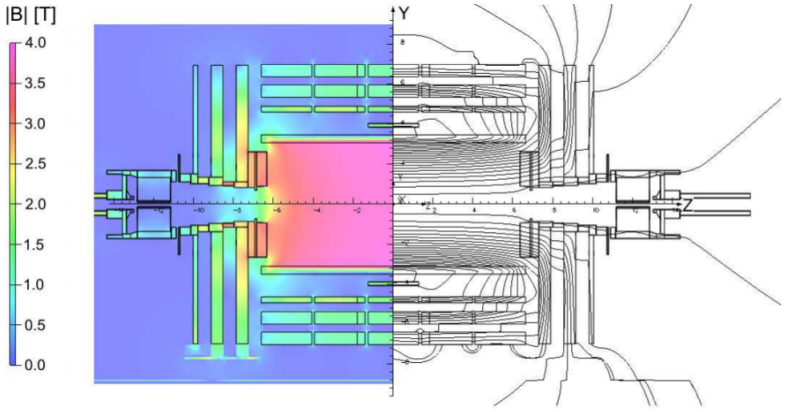

Figure 3.9: The CMS magnet and the generated magnetic field [6]

The CMS magnet is a $13m$ long superconducting solenoid, the largest ever built. It is able to generate a uniform magnetic field of $4T$ in the inner region, storing about $2.5GJ$ of energy. It operates at a temperature of $4K$, ensured by a sophisticated helium cooling system. At such temperatures, the flat $NiTb$ cable becomes superconducting, allowing a $20kA$ current to flow without appreciable loss.

The whole magnet is contained in a enormous vacuum cylinder, which isolates it from the external environment. Outside, an iron structure composed by five barrel layers and three disks for each endcap constitutes the iron yoke, needed to guide the return magnetic field, which would get lost otherwise, causing interferences. The CMS magnet provides a huge bending power, allowing a precise measurement of the transverse momentum of charged particles inside the solenoid, operated by the inner tracking system. A further and independent p_T measurement outside the solenoid is possible thanks to the iron yoke, which surrounds the muon chambers.

3.4.2 The Muon System

Muons provide a clear signature for many physics processes. For this reason, the muon spectrometer must provide a robust trigger and an accurate measurement of the muon momentum and charge, also without the contribution of the Tracker. The muon system, shown in 3.10, is embedded in the iron return yoke of the magnet, which shields the detectors from charged particles other than muons. The minimum value of the muon transverse momentum required to reach the system is $\simeq 5GeV$. The muon spectrometer consists of three independent subsystems.

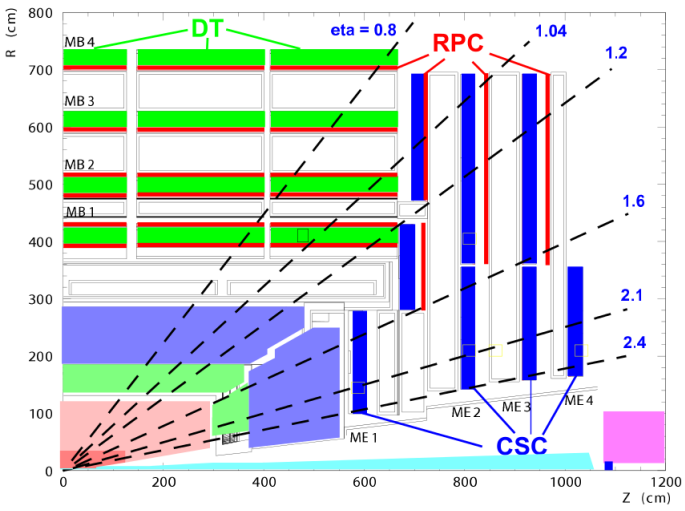

Figure 3.10: Schematic view of the Muon system. [6]

In the barrel ($|\eta| < 1.2$), where the track density and the residual magnetic field are low, four layers (stations) of drift tube chambers (DT) are installed. The chamber segmentation follows that of the iron yoke, consisting of five wheels along the z axis, each one divided into 12 azimuthal sectors. Each chamber has a resolution of about $100\mu m$ in $r\phi$ and $1mrad$ in ϕ.

In the endcaps ($0.8 < |\eta| < 2.4$), four disks (stations) of cathode strip chambers (CSC) are located, being this detector technology more indicated in a region suffering high particle rates and large residual magnetic field between the plates of the yoke. The rings are formed by 18 or 36 trapezoidal chambers, which are stacked with a small overlap in ϕ. These chambers have a spatial resolution of about $200m$ ($100m$ for the chambers belonging to the first station) and $10mrad$ in $r - \phi$. Redundancy is obtained with a system of resistive plate chambers (RPC), that are installed in both the barrel and the endcaps. RPCs have limited spatial resolution, but fast response and excellent time resolution of few ns, providing unambiguous bunch crossing identification. RPC detectors operate in avalanche mode, thus allowing the detectors to sustain higher rates. This mode is obtained with a lower electric field, thus the gas multiplication is reduced and an improved electronic amplification is required. In the barrel the RPC chambers follow the segmentation of DT chambers. A total of six layers of RPCs are present. In the endcaps the chambers are trapezoidal distributed on four disks. They are also used to complement DTs and CSCs in the measurement of p_T. The RPC system covers the region $|\eta| < 2.1$. The robustness of the spectrometer is also guaranteed by the different sensitivity of DT, RPC and CSC to the background. The main sources of background particles in the LHC environment will be represented by secondary muons produced in pion and kaon decays, from punch-through hadrons and from low energy electrons originating after slow neutron capture by nuclei with subsequent photon emission. This neutron induced background will be the responsible of the major contribution to the occupancy level in the muon detectors. CSC and DT chambers, in contrast with RPC detectors, are characterised by a layer layout which helps in reducing the effect of background hits: the request of correlation between consecutive layers is particularly effective against background hits

affecting only a single layer.

3.5 Trigger System and Data Acquisition

The huge amount of data produced due to the high interaction rate produced at LHC cannot be sustained by any storage system presently available. Given the typical size of a raw event ($1MB$), only a rate of $\approx 100Hz$ can be stored for offline analysis, when the collisions rate is in fact $40MHz$. A huge reduction factor is thus necessary: it is accomplished by the trigger and the data acquisition systems.

3.5.1 The Trigger System

The event rate is mainly composed of protons interactions with particles of low transverse momentum. A good triggering system should have a large rejection of the less interesting particles and maintain at the same time a high efficiency on the (potential) interesting events. This characteristic is achieved at CMS in two steps: a Level 1 Trigger (L1) and a High Level Trigger (HLT). The rate reduction capability is designed to be a factor of 107 for the combined L1 and HLT.

3.5.2 The Level 1 Trigger

The Level 1 Trigger consists of custom-designed, largely programmable electronics: it reduces the rate of selected events down to $100kHz$ for the high luminosity runs. The full data are stored in pipelines of processing elements, while waiting for the trigger decision. The maximum latency allowed is $3.2\mu s$: if the L1 accepts the event, the data are moved to be processed by the High Level Trigger. The high bunch crossing rate does not permit the full readout of the detector, mainly because of the slowness of the tracker algorithms: only the calorimetric and muons information are employed. The Calorimeter Trigger identifies the best four candidates of each of the following classes: electrons and photons, central jets, forward jets and so on identified from the shape of the deposited energy. The information of these objects is passed to the Global Trigger, together with the measured missing E_T . The Muon trigger is performed separately for each muon detector. The information is then merged and the best four muon candidates are transferred to the Global Trigger. The Global Trigger takes the decision to reject an event or to accept the event for further evaluation by the HLT. The decision is based on algorithm calculations and on the readiness of the sub-detectors and the DAQ. The L1 Trigger electronics is housed partly on the detectors, partly in the underground control room located at a distance of approximately $20m$ from the CMS detector site.

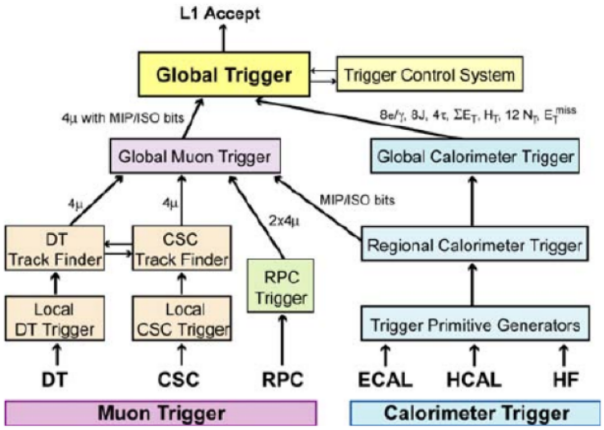

Figure 3.11: Scheme of the L1 trigger. [6]

3.5.3 The High Level Trigger (HLT)

HLT is a software system (implemented in a filter farm of about one thousand commercial processors) which reduces the output rate down to around 100 Hz. The idea of the HLT trigger software is the regional reconstruction on demand: only objects in the useful regions are reconstructed and uninteresting events are rejected as soon as possible. The HLT has access to the high-resolution data in pipelined memories in the front-end electronics as well as the information from the silicon tracker: it can therefore perform complex calculations. The L1 and HLT schema lead to the development of three "virtual trigger" levels: at the first level only the full information of the muon system and of the calorimeters is used, in the second level the information of the tracker pixels is added and in the third and final level the full event information is available.

3.5.4 The Data Acquisition (DAQ)

The CMS Data Acquisition (DAQ) [32] has the task to transport the data from about 650 data sources at the detector side, to the filter units for processing of complete events. Each data source provides event fragments of about $2kB$. The central DAQ runs online software on about 3000 PC used for buffering and processing of event data. The DAQ system of CMS is shown in 3.12. The detector is read out through a builder network with a bandwidth of $100GB/s$ by the so called Front-End Drivers (FED). The FEDs are located in the underground counting room $\sim 70m$ from the detector. Complete events are fed to the event filter systems at a rate of maximal $100kHz$. The large rate to the filter systems stems from the design choice of CMS to build the full event already after the first level trigger instead of building partial events as in traditional multi level trigger systems. This requires the read-out, assembly and forwarding of the full event data at the nominal level one trigger rate. The total rate of data produced by the online trigger system is $\sim 230MB/s$. These data need to be stored for further processing and analysis.

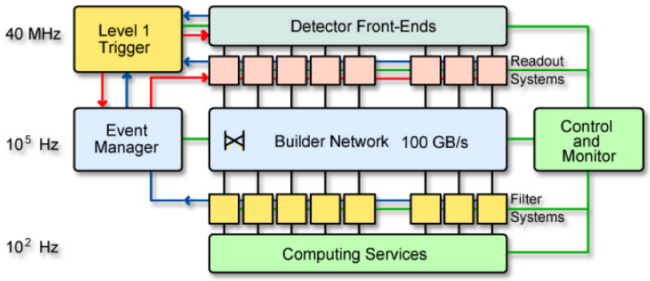

Figure 3.12: Scheme of the DAQ system. [6]

3.6 Software Framework and Computational Challenge

The CMS experiment poses new challenges not only in terms of the physics to discover and the detector to build and operate, but also in terms of the data volume and the necessary computing resources. Datasets and resource requirements are at least an order of magnitude larger than in previous LEP experiments.

CMS computing and storage requirements is, with present technology, impossible to fulfil in only one place, for both technical and funding reasons. Therefore, the CMS computing environment has been constructed as a distributed system of computing services and resources that interact and cooperate with each other, as Grid services. The set of services and computing resources are used for storage, connectivity resources, data processing, data archiving, Monte Carlo event generation and all kinds of computing-related activities.

Grid computing aims to provide reliable and secure access to widely scattered resources for authorized users located virtually anywhere in the world. When a user submits a job, the Grid software controls where the job gets sent for processing.

A 3-level Tier structure of computing resources has been organized to handle the vast storage and computational requirements of the CMS experiment. A CMS physicist may use Grid tools to submit a CMS analysis job to a "Workload Management System" (WMS), and does not need to worry about the details such as location of data and available computing power, which are handled transparently.

The CMS Grid system is part of the larger Worldwide LHC Computing Grid Project (WLCG). The mission of the WLHC Computing Project (WLCG) is to build and maintain a data storage and analysis infrastructure for the entire high energy physics community that will use the LHC. The WLCG project aims to collaborate and interoperate with other major Grid development projects and production environments around the world. As such, WLCG has developed relationships with regional computing centres as T1 centres. These centres exist in a number of different countries in Europe, North America and Asia.

As stated just above, the computing centres available to CMS through the Grid system around the world are distributed and configured in a "tier" architecture. Each of the three tier levels provides different resources and services:

- Tier-0, the first tier in the CMS model, for which there is only one site, CERN.

Among its tasks there are: accept, archive and distribute RAW data collected from the CMS Online Data Acquisition and Trigger System (TriDAS), perform Prompt calibration in order to get the calibration constants needed to run the reconstruction, perform prompt first pass reconstruction which writes the RECO and Analysis Object Data (AOD) extraction, transfer Prompt reconstructed RECO and AOD datasets to Tier-1.

- Tier-1: there is a set of seven Tier-1 (T1) sites, which are large centers in CMS collaborating countries (large national labs o research institutes, e.g. INFN, and FNAL) Among its tasks there are: archive and redistribute to Tier-2 RAW, RECO, AOD and MC samples,

- Tier-2: this is a more numerous set of smaller centres, but with substantial CPU resources, providing capacity for user analysis, calibration studies, and Monte Carlo production. Tier-2 provide limited disk space, and no tape archiving. T2 centers rely upon T1s for access to large datasets and for secure storage of the new data (i.e. Montecarlo simulations) produced at the T2.

CMS Data is arranged into a hierarchy of data tiers. Each physics event is written into each data tier, where the tiers each contain different levels of information about the event. The three main data tiers used in CMS are:

- RAW: full event information from the Tier-0 (i.e. from CERN), containing 'raw' detector information (detector element hits, detailed trigger information, various electronic info). Not used directly for analysis.

- RECO ("RECOnstructed data"): the output from first-pass processing by the Tier-0. This layer contains reconstructed physics objects and part of RAW info, thus it's still very detailed and may slow down analysis when CMS has collected a substantial data sample.

  The event reconstruction step from RAW to RECO is structured in several hierarchical steps:

  1. Detector-specific processing: Starting from detector data unpacking and decoding, detector calibration constants are applied and cluster or hit objects are reconstructed.
  2. Tracking: Hits in the silicon and muon detectors are used to reconstruct global tracks. Pattern recognition in the tracker is the most CPU-intensive task.
  3. Vertexing: Reconstructs primary and secondary vertex candidates.
  4. Particle identification: Produces the objects most associated with physics analyses. Using a wide variety of sophisticated algorithms, standard physics object candidates are created (electrons, photons, muons, missing transverse energy and jets; heavy-quarks, tau decay).

  The normal completion of the reconstruction task will result in a full set of these reconstructed objects usable in physics analyses. Reconstruction is expensive in terms of CPU and is dominated by tracking.

- AOD ("Analysis Object Data"): this is a "distilled" version of the RECO event information, and is expected to be used for most analyses. AOD provides a compromise between event size and complexity of the available information to optimize flexibility and speed for analyses, most of the raw information of the detector are lost at this point.

The overall collection of software used in CMS is referred to as CMSSW, it is built around a Framework, an Event Data Model (EDM), and Services needed by the simulation, calibration and alignment, and reconstruction modules that process event data so that analysis can be performed. The primary goal of the Framework and EDM is to facilitate the development and deployment of reconstruction and analysis software.

The CMSSW event processing model consists of one executable, called cmsRun, and many plug-in modules which are managed by the Framework. All the code needed in the event processing (calibration, reconstruction algorithms, etc.) is contained in the modules. The same executable is used for both detector and Monte Carlo data.

The CMSSW executable, cmsRun, is configured at run time by the user's job-specific configuration file. This file tells cmsRun

- which data to use
- which modules to execute
- which parameter settings to use for each module
- what is the order or the executions of modules, called path
- how the events are filtered within each path and how the paths are connected to the output files

The CMS Event Data Model (EDM) is centered around the concept of an Event. An Event is a C++ object container for all RAW and reconstructed data related to a particular collision. During processing, data are passed from one module to the next via the Event, and are accessed only through the Event. All objects in the Event may be individually or collectively stored in ROOT files, and are thus directly browsable in ROOT.

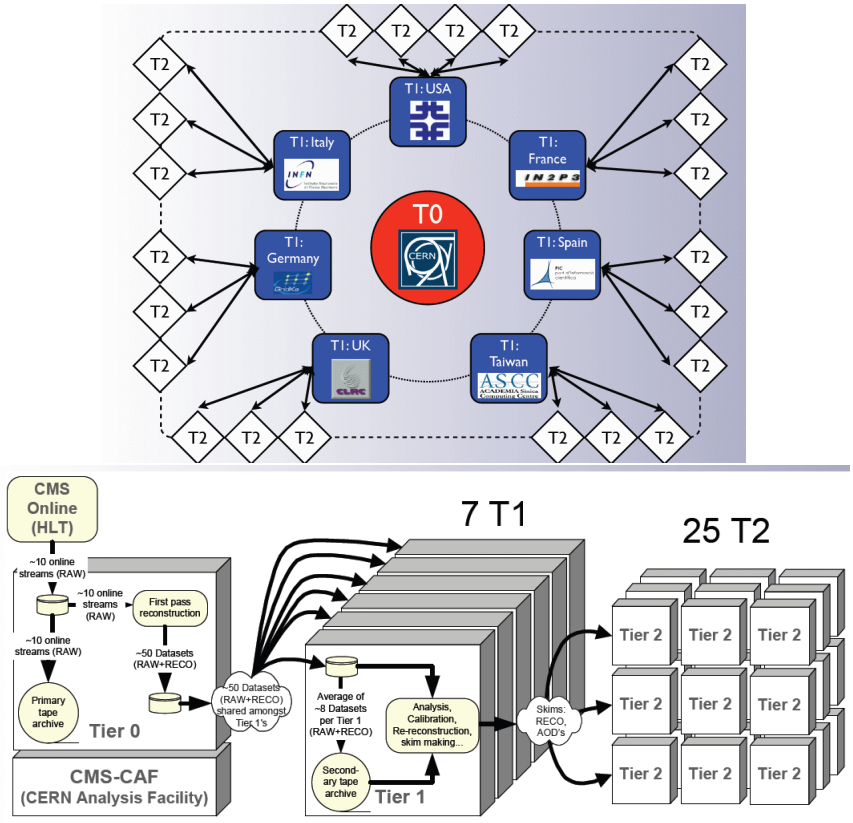

Figure 3.13: Schematic representation of the CMS Grid storage tier structure and the associated data workflow [6]

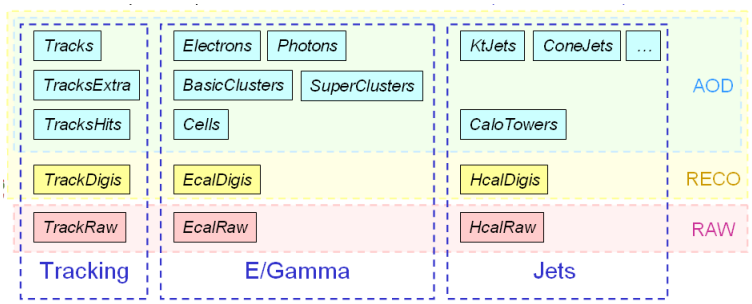

Figure 3.14: Schematic representation and comparison of the CMS Data tiers content [6]

Given the large data volumes involved and the large size of the CMS collaboration, a fully distributed computing model is used for data reconstruction and analysis. The system is based upon Grid middleware, with the common Grid services at centres defined and managed through the Worldwide LHC Computing Grid (WLCG) project, a collaboration between LHC experiments, computing centres, and middleware providers.

Chapter 4

Data Analysis

4.1 Analysis Strategy

χ_{c1} and χ_{c2} candidates are selected by searching for their radiative decays into the $J/\psi\gamma$ final state, with the J/ψ decaying into two muons.

The reconstruction starts from the standard CMS J/ψ to $\mu\mu$ selection criteria, which will be described later in the next section. Other cuts on the dimuon objects will be applied to further select the number of candidates. To complete the reconstruction of the χ_c, a sufficiently accurate reconstruction of the photon is needed. The photon has an energy of $413MeV$ for the χ_{c1} decay and $459MeV$ for the χ_{c1} in the center of mass of the χ_c states, which results in a p_T of the detected photon mostly between $0.5GeV$ and $6GeV$ in the laboratory frame. In order to distinguish the two, the initial idea would be to use the Electromagnetic Calorimeter to detect the photon. However given the small difference in mass between χ_{c1} and χ_{c2} states ($\approx 45MeV$), a resolution in energy of the ECAL of less than $45MeV$ is needed. As described earlier in the detector chapter, the energy resolution of ECAL is not sufficient thus using this subdetector to reconstruct the γ would not allow to resolve the two very close charmonium resonances.

The CMS ECAL is in fact built and optimized with the goal of reconstruction of more energetic photons and electrons that are useful for Higgs and physics beyond the standard model searches. In Figure 4.1 it is reported an early attempt of plotting the invariant mass of $\chi_{c1,c2}$ where photons are reconstructed using calorimetric photons ($p_T > 1GeV$).

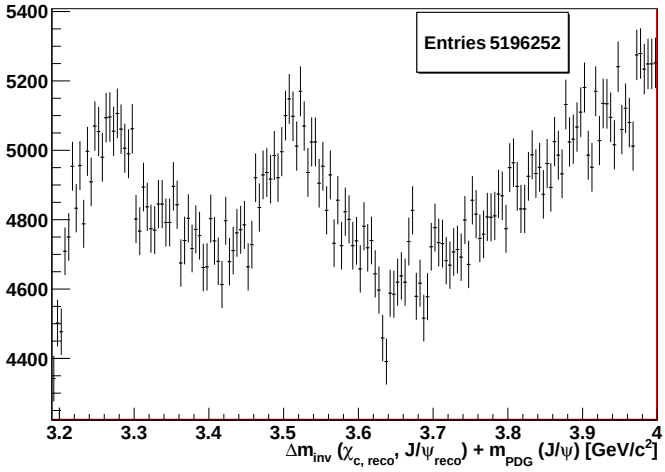

Figure 4.1: Invariant mass of $\chi_{c1,c2}$ where photons are reconstructed using calorimetric photons ($p_{T\gamma} > 1GeV$)

On the contrary, a measurement of the momentum of the two electrons originating from a conversion of the photon in the beam pipe or in the inner layers of the tracker results in a sufficiently precise measurement of the photon energy, given the outstanding p_T resolution of the inner CMS tracker. However using reconstruction through conversions leads to a reduced yield of events, due to the conversion probability in the tracker and, most important, to the low reconstruction efficiency because of the difficulty reconstruct low energy conversion. Low energy conversions are harder to reconstruct because low p_T electrons may leave short and low quality tracks (i.e. with few hits in the tracker) thus standard CMS conversion reconstruction algorithms, tuned for higher energy conversions, may not be efficient enough for this study. A dedicated low energy conversion reconstruction algorithm has been developed for this analysis and details will be discussed in a following section of this chapter.

For each χ_c candidate, the mass difference $m_{\mu\mu\gamma} - m_{\mu\mu}$ is evaluated. It has been chosen to use the mass difference instead of the bare mass to factorize, in the plot, the error on the determination of the J/ψ candidate mass. An unbinned maximum likelihood fit to the mass difference spectrum is then performed to extract the yield of χ_{c1} and χ_{c2} for several bins of the p_T of the J/ψ. A correction must be applied for the different acceptance of the detector for the two states (mostly driven by a different acceptance of the conversion reconstruction between the two charmonium states). The ratio of the production cross section is then obtained as:

$$\frac{\sigma(pp \to \chi_{c2})}{\sigma(pp \to \chi_{c1})} = \frac{N_{\chi c2}}{N_{\chi c1}} \cdot \frac{\epsilon_1}{\epsilon_2} \cdot \frac{BR(\chi_{c1} \to J/\psi\gamma)}{BR(\chi_{c2} \to J/\psi\gamma)} \tag{4.1}$$

where N_{χ_i} is the number of candidates of each type obtained from the fit, ϵ_1/ϵ_2 is the acceptance correction derived from a full detector simulation, and BR are the branching ratios obtained from the PDG.

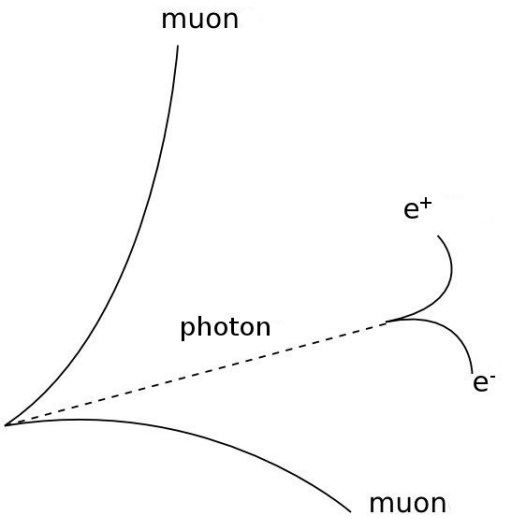

Figure 4.2: Schematic representation of the decay process taken into account in this analysis.

4.2 Data and Event Selection

4.2.1 Dataset

The data acquired by LHC in the 2011 run has been taken into account in this analysis. The 2011 LHC run is subdivided in two periods: 2011A and 2011B, the latter is characterized by higher instantaneous luminosity and larger number of interactions per bunch crossing.

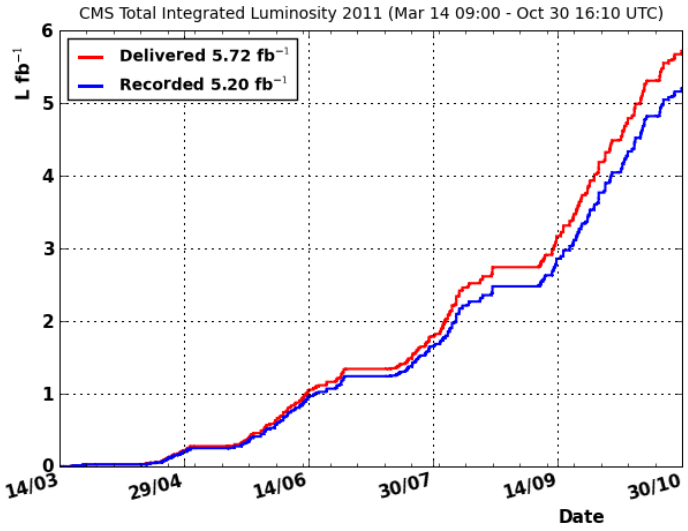

Figure 4.3: Total Integrated Luminosity vs. Time: integrated luminosity versus time delivered to (red), and recorded by CMS (blue) during stable beams at $7TeV$ centre-of-mass energy.

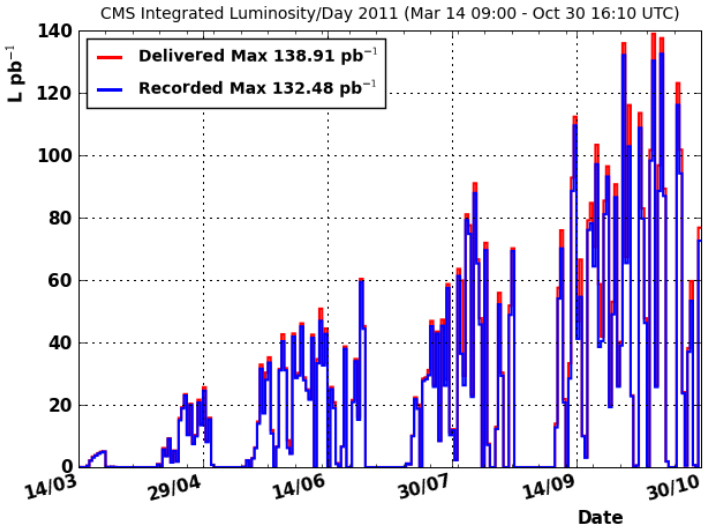

Figure 4.4: Total Integrated Luminosity Per Day: integrated luminosity per day delivered to (red), and recorded by CMS (blue) during stable beams at $7TeV$ centre-of-mass energy.

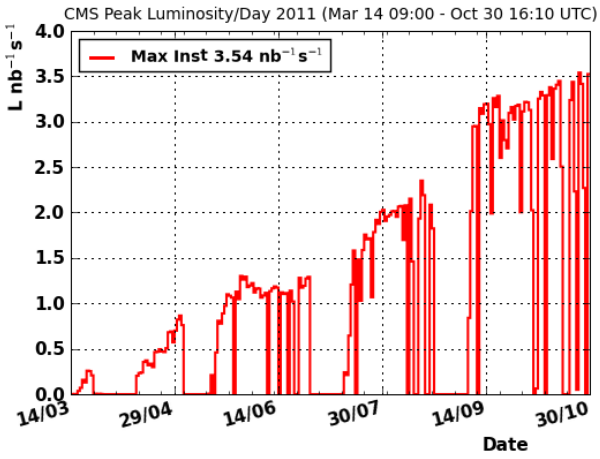

Figure 4.5: Instantaneous Luminosity: maximum Instantaneous luminosity per day delivered to (red) CMS during stable beams at $7TeV$ centre-of-mass energy.

This second run (2011B) poses more problems of pileup, which means the superposition of several pp interactions registered by the same events.

To separate the tracks and the other physical objects coming from different pp interaction the role of the pixel inner tracker is essential. The primary vertices of pp interactions must be determined with great accuracy to avoid utilizing tracks/objects from different vertices.

While the vertexing process uses sophisticated algorithms to reconstruct the primary vertices there is always the possibility of misassignment of tracks thus this may cause a dependence of the results of the analysis from pileup. In a later section of this chapter this possible dependence from pileup will be taken into account.

Another difference between the two run is the different trigger conditions used, trigger bits requirements and prescale tables have been changed in the high luminosity run to favour high p_T final states thus reducing the frequency of events saved. Setting higher prescale factor for trigger bits means that the number of events that pass a certain trigger is further reduced by the prescale factor. This change reduced in run 2011B the number of final χ_c candidates per unit of luminosity of a factor ~ 4 due to the modified rates in J/ψ triggers rates.

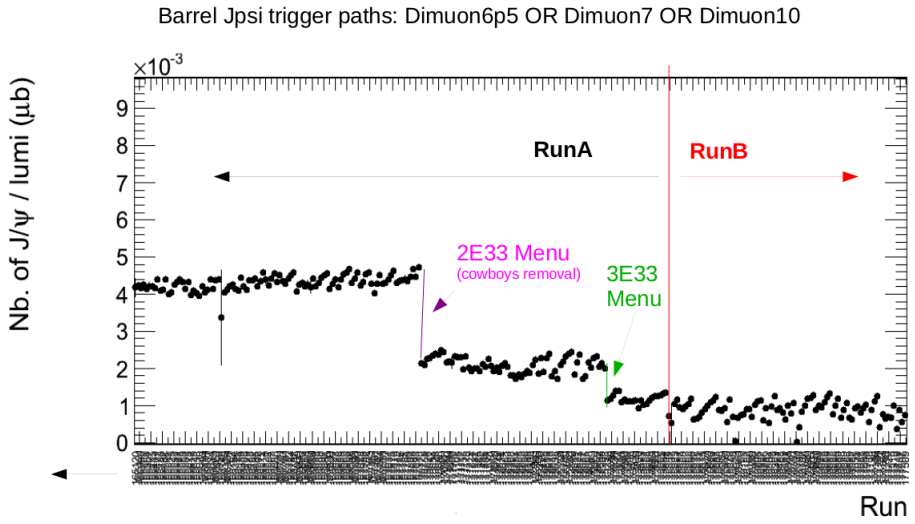

Figure 4.6: Drop in J/ψ candidates in run 2011B due to modified trigger tables.

4.2.2 J/ψ reconstruction

The first step in the reconstruction of the candidate χ_c is the selection of good J/ψ candidates decayed in $\mu^+\mu^-$ couples. The starting point of $J/\psi \to \mu^+\mu^-$ event selection is an already pre-selected dataset provided by the CMS Collaboration. The selection is performed through the following High Level Trigger bits:

```
HLT_DoubleMu2_Bs_v1
HLT_DoubleMu3_Jpsi_v2
HLT_DoubleMu3_LowMass_v1
HLT_DoubleMu3_Quarkonium_v2
HLT_DoubleMu3_Upsilon_v1
HLT_Mu3_Track3_Jpsi_v5
HLT_Mu5_L2Mu2_Jpsi_v2
HLT_Mu5_L2Mu2_v2
HLT_Mu5_Track2_Jpsi_v1
HLT_Mu7_Track5_Jpsi_v2
HLT_Mu7_Track7_Jpsi_v2
```

The HLT_Mu* triggers are single muon using very loose L1 muon trigger primitives. After reconstructing the track in the HLT online farm, including information from the Silicon tracker, a p_T cut of 3, 5 and 7 GeV/c is imposed respectively for HLT_Mu3_*, HLT_Mu5_ and HLT_Mu7_. The differentiation between the various HLT_MuX_* triggers lies in the particular algorithm used to reconstruct the track and on eventual additional cuts, however these details are not relevant at this stage as the next step of selection will require much stronger cuts to identify the J/ψ meson.

The HLT_DoubleMu* triggers on the other hand require at least two muons with a cut on p_T of 2 and 3 Gev/c for HLT_DoubleMu2_* and HLT_DoubleMu3_* respectively. In this case too, the differences between the HLT_MuX_* algorithms are technical and not relevant in this analysis because the goal of this analysis is not to measure a plain

cross section rather a cross section ratio thus the trigger efficiencies cancel out in the ratio.

It is worth to note that these trigger bits are combined with 'OR' operators, which means that it is enough for only one of the trigger path algorithms to 'approve' the event for it to be saved in the skimmed dataset.

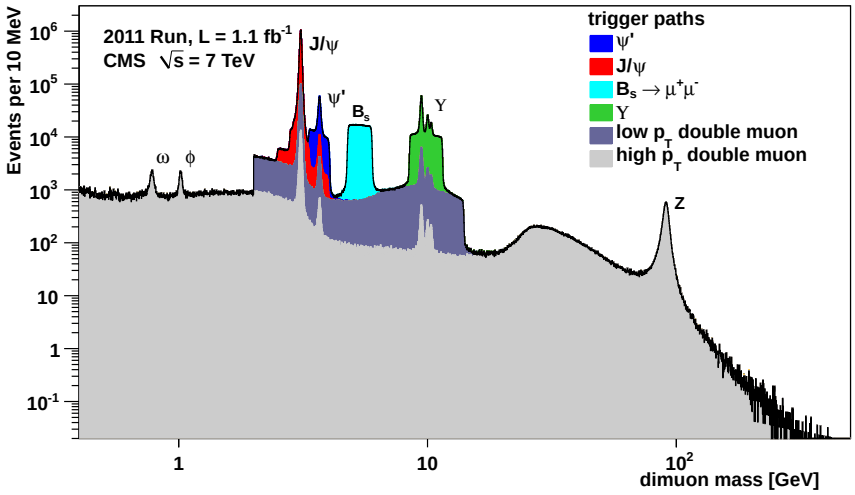

Figure 4.7: 2011 data collected by early July, corresponding to an integrated luminosity of $1.1 fb^{-1}$, superposition of various dimuon trigger paths

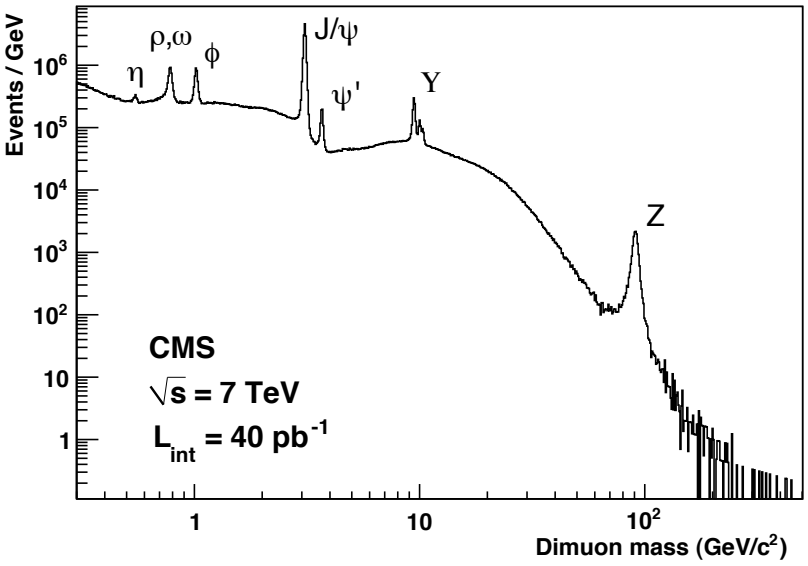

Figure 4.8: 2010 data, corresponding to an integrated luminosity of $40 pb^{-1}$, dimuon trigger path with no p_T threshold

The next step in J/ψ selection involves another 'standard' CMS skimming tool used as a basis for most quarkonium and B-physics studies called the Onia2MuMu analyzer. Before describing the cuts applied at the level of Onia2MuMu analyzer, a little digression on offline (i.e. after the data has been stored permanently) muon reconstruction is needed.

In the CMS standard offline muon reconstruction process, muons are defined as tracks reconstructed in the silicon tracker which are associated to a compatible signal in the muon chambers. Tracks are reconstructed using a Kalman filter algorithm which starts from pixel tracker seeds and then extrapolates the track to the silicon strip tracker.

Two different reconstructed muon types are thus distinguished. The first one, called Global Muon, provides high-quality and high-purity muon reconstruction for tracks with $p_T > 4GeV/c$ in the central pseudo-rapidity region, and $pT > 1GeV/c$ in the forward region. The second muon type, called Tracker Muon, achieves a better reconstruction efficiency at lower momenta.

Global Muons are built as a combined fit of silicon and muon-chamber hits, coming from different track segments found in the tracker and muon systems. In the muon system at least two stations must be present. The χ^2 per degree of freedom of the combined fit is required to be smaller than 20. On the other hand, the requirements for a Tracker Muon are looser than for Global Muons: the tracks found in the Tracker must be matched to at least one muon segment in one muon station. The two muon types differ in the way the hits in the muon chambers are combined with those of the tracker: requirements for Tracker Muons are less stringent, at the expense of a slightly larger background. If two or more tracks are close to each other, it is possible that the same muon segment or set of segments is associated to more than one track. In this case only one of the best matching track is chosen.

There is an overlap between these two reconstruction algorithms. If a Global Muon has an associated silicon track that has also been reconstructed as Tracker Muon, then it is assigned to the Global Muon category alone, making the two categories exclusive. For either case the track momentum is determined by the fit in the Tracker only. Further cuts are applied to the tracks to reject fake muons. The tracks must have at least 12 hits in the Tracker detector, out of which two in the pixel layers, a χ^2 per degree of freedom smaller than 4, and must pass within a cylinder of radius $3cm$ and length $30cm$ centered at the vertex of the primary interaction and parallel to the beam line.

The momentum measurement of muons and, more generally, of all charged tracks in the CMS detector can be affected by systematic uncertainties due to imperfect knowledge of the magnetic field and of the material budget, to subdetectors misalignment and to biases in the algorithms which fit the track trajectory. Studies performed with cosmic-ray muons and collision data show a very precise control of all these possible biases.

To select dimuon decays (that is, particles decaying in $\mu^+\mu^-$) the two muons trajectories are re-fitted forcing them originate from a common vertex, and events are retained if the fit χ^2 probability is larger than 0.1%. Pairs made of different muon type combinations are reconstructed: two global muons, two tracker muons or one global and one tracker muon. In case of multiple combinations in the same event, the combination with the purest muon content is chosen (global muon being favoured with respect to tracker muons). If two candidate pairs belong to the same dimuon type combination, the one with the largest p_T is chosen.

To select the events with J/ψ decays, muons with opposite charge are paired and their invariant mass is computed. The invariant mass of the muon pair is required to be between $3.0GeV/c^2$ and $3.2GeV/c^2$. In Figure 4.9 is reported the mass plot of J/ψ candidates before mass cut selection.

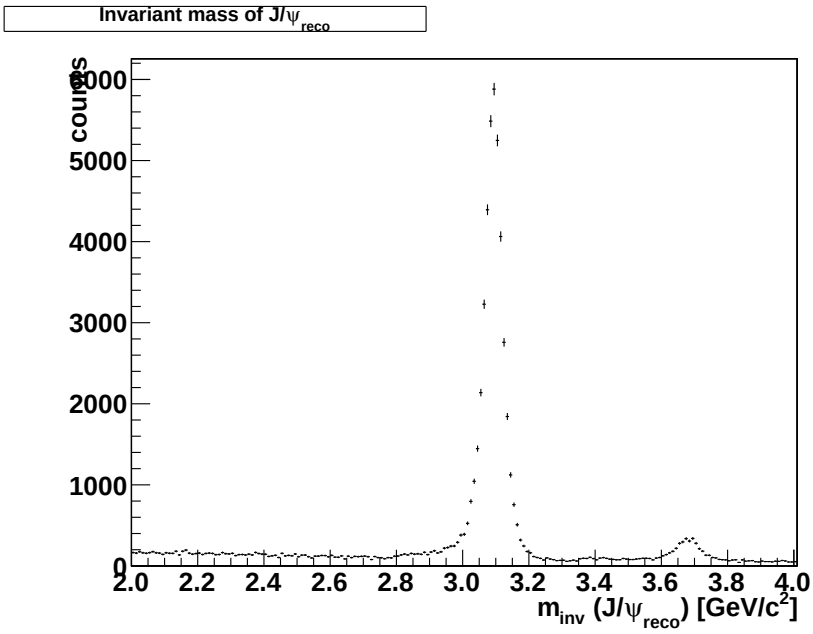

Figure 4.9: J/ψ candidates mass distribution (before mass cut).

The primary vertex of interaction is required to be contained in a cylinder collinear with the beamline, centred in the interaction point with radius $2.0cm$ and half-length $15.0cm$.

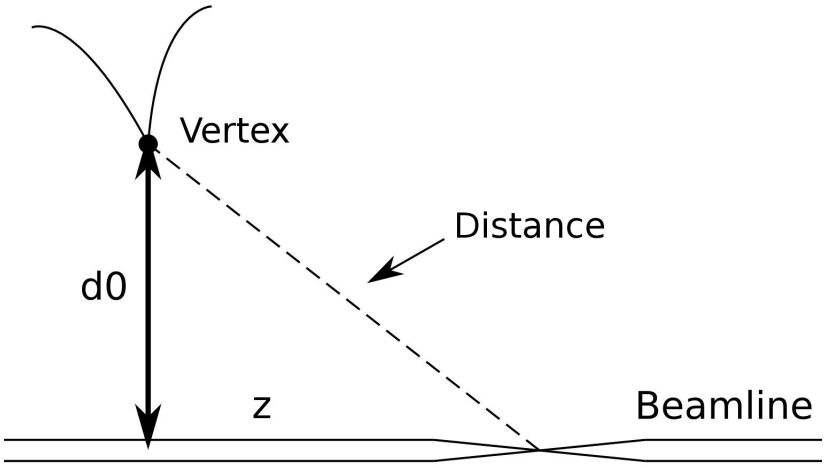

Figure 4.10: Schematic illustration of primary vertex cuts.

A further cut is applied concerning the rapidity of the J/ψ candidate: $|y_{\mu^+\mu^-}| < 1$, where y is the rapidity. This cut is performed to avoid that the photon generated by the χ_c decay will convert in the tracker endcap. The tracker endcaps begin at $|y| = 1.1$, however the cut is applied at $|y| = 1.0$ because between 1.0 and 1.1 there is a little region where the particle, crosses the pixel barrel, then a small piece of the pixel endcap and continues in the barrel strip detector. This "crossing" of different layers of the inner tracker makes the photon cross a thick non detecting material which may make it convert

thus making the delicate conversion reconstruction more complicated and less efficient. To avoid these problems the cut is set at $|y_{\mu^+\mu^-}| < 1$.

The last cut applied to J/ψ selection is a lifetime cut: $ct < 0.1mm$ where ct is the space of flight, the distance between the dimuon reconstructed vertex and the primary vertex, this cut allows to separate the χ_c promptly produced in the primary collision from the ones produced by the decays of B mesons. With this cut the χ_c promptly produced are selected; only promptly produced χ_c will be considered in the rest of the analysis. In Figure 4.11 the ct distribution of J/ψ candidates is shown.

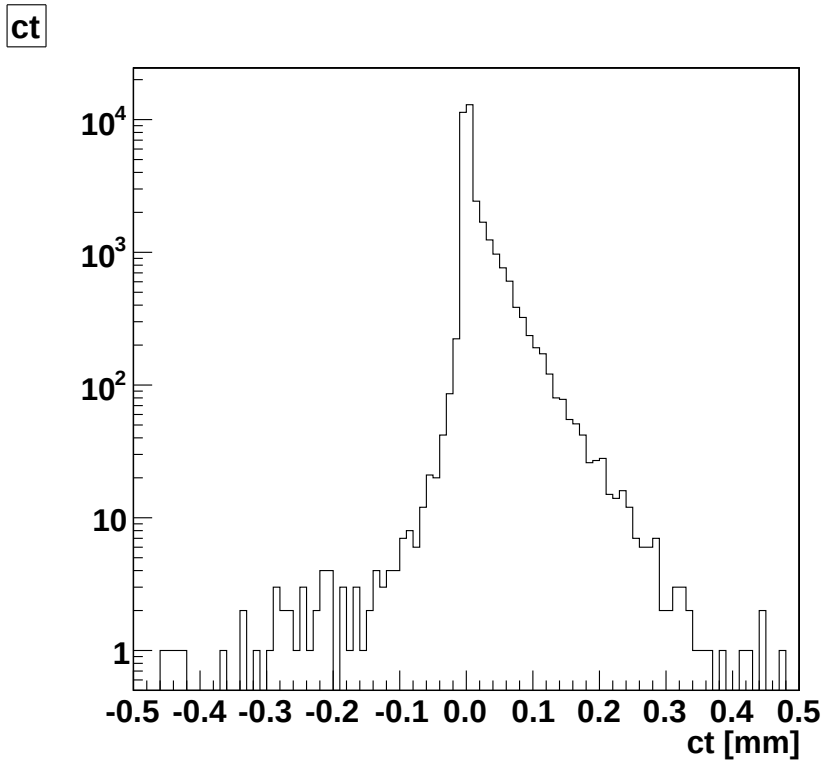

Figure 4.11: ct distribution of J/ψ candidates

In Figure 4.12 the selected J/ψ are shown.

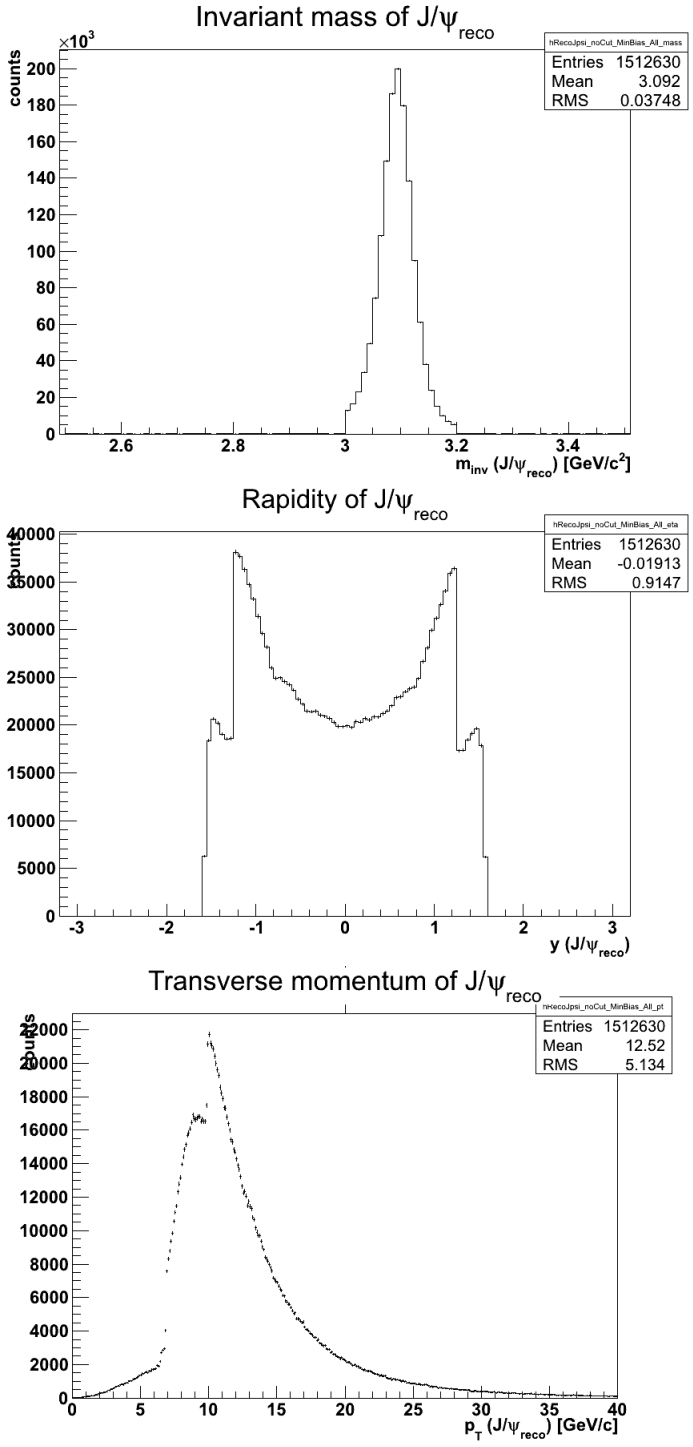

Figure 4.12: Invariant mass, p_T and rapidity distribution of selected J/ψ candidates.

4.2.3 Conversion reconstruction

The fundamental step in the χ_c candidate reconstruction is the reconstruction of the converted photon.

The algorithm used in this analysis for photon conversion reconstruction has been developed within the CMS collaboration and it is described in detail in the following

references [9] [8].

Following is a brief summary of the algorithm specifications to select the conversion candidates and the modifications and additional cuts applied specific to this χ_c analysis.

Photon conversions are characterized by an electron-positron pair originating from the photon vertex. The invariant mass must be compatible with zero and the two tracks are therefore parallel at production vertex and open only in the transverse plane because of the solenoidal magnetic field.

Some relevant plots about standard conversion reconstruction are shown in Figure 4.13, 4.14 and 4.15.

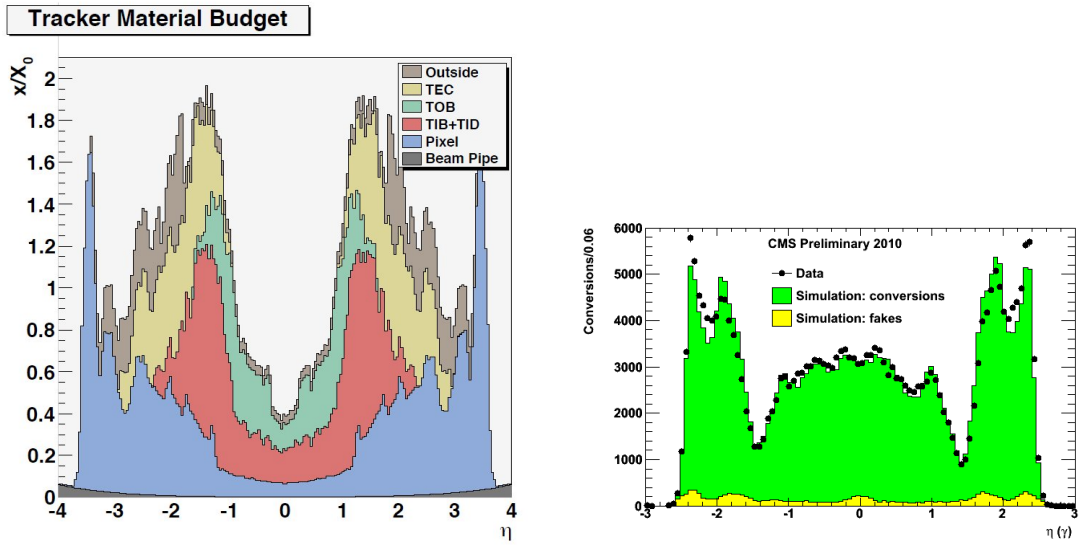

Figure 4.13: Material tracker budget in terms of radiation lengths (x/X_0) in function of pseudorapidity η and pseudorapidity distribution for all conversion candidates as reconstructed from the track-pair momentum in data and simulation (splitting fake candidates and real ones) [8].

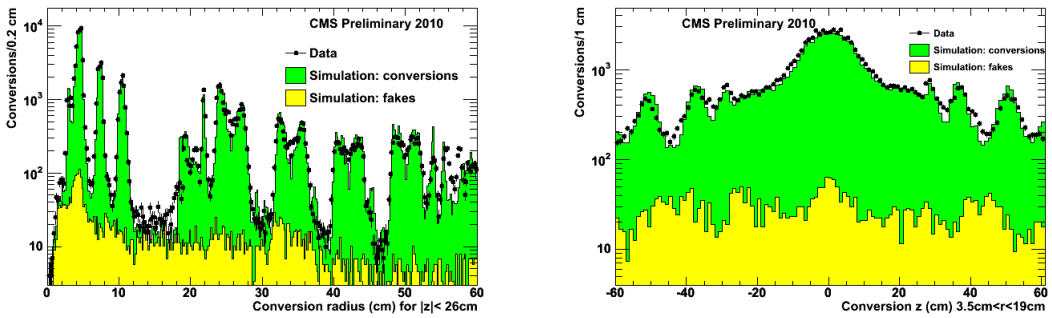

Figure 4.14: Conversion vertices: distributions of the radial position for $|z| < 26cm$, i.e. the central portion of the Tracker barrel, and longitudinal position for $3.5cm < R < 19cm$, i.e. Pixel Detector. In data the radius is calculated with respect to the centre of the Pixel detector. In simulation the contribution from real and fake conversions is splitted [8].

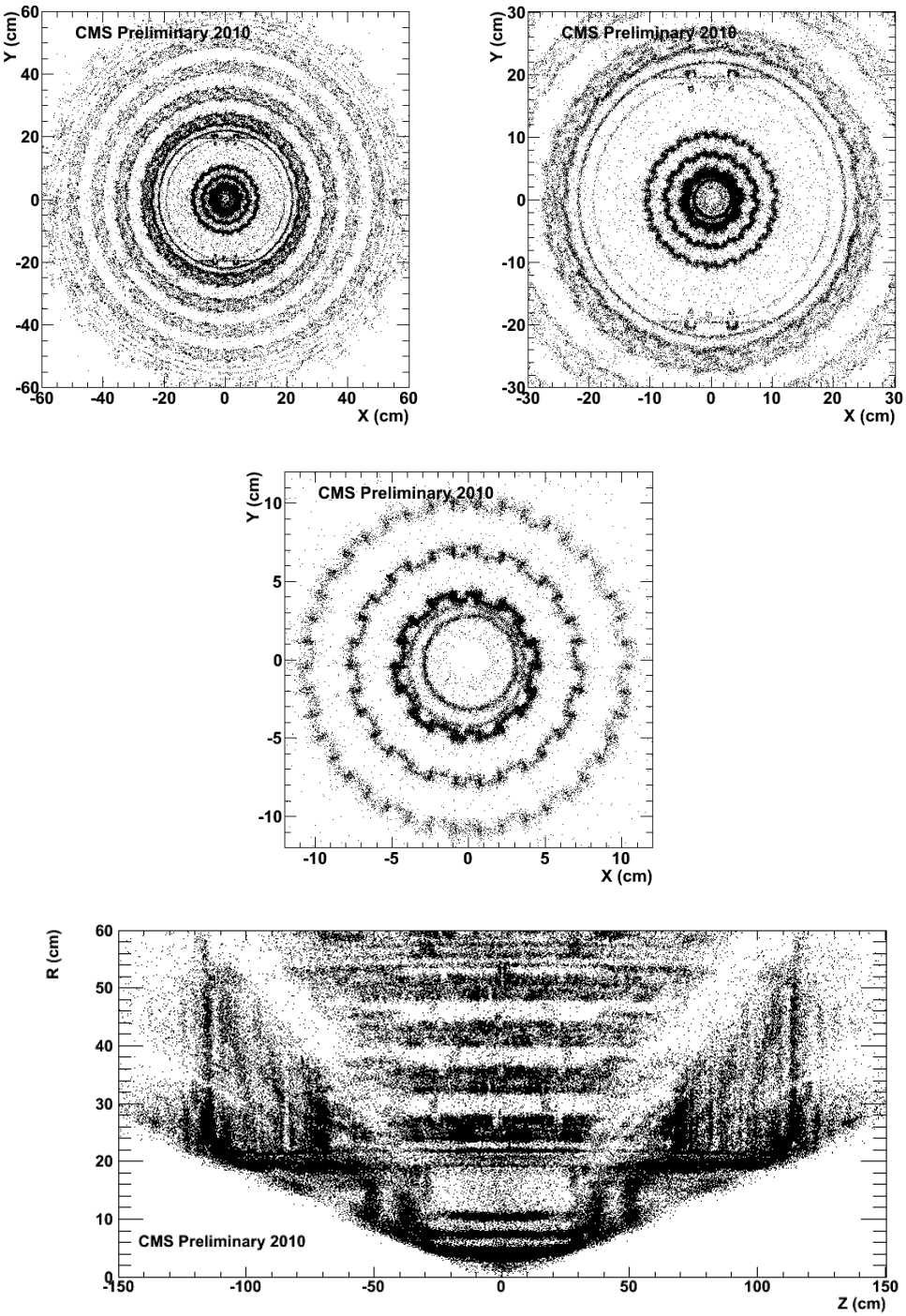

Figure 4.15: Conversion vertices in data in the (x, y) plane for $|z| < 26cm$ with increasing zoom and conversion vertices in data the (z, R) plane [8].

Photons originating from the radiative decay of the χ_c are very soft, and also the electron-positron pair resulting from an eventual photon conversions results soft as well. Because the electrons produced in these conversions are low energetic, most of them are either fully stopped before they reach the electromagnetic calorimeter or they are bended in a spiral (helix in 3D) within the tracker, thus such conversions can be only

reconstructed within the tracker detector. For this reason the algorithm is named tracker-driven conversion reconstruction, as it uses only the tracker.

The algorithm relies on the capability of iterative tracking, described in [9], to efficiently reconstruct low-p_T and displaced tracks as the ones coming from a typical photon conversion.

Opposite-sign track pairs are firstly required to satisfy basic quality criteria, i.e. have ≥ 6 hits and normalised $\chi^2 < 10$. Then the tracker-only conversion finding exploits the conversion pair signature to distinguish genuine pairs from fake pairs. Tracks are required to have positive charge-signed transverse impact parameter (the primary vertex lies outside the track trajectory helix) and the distance of minimum approach in the xy plane, d_m, between $-0.25cm$ and $1cm$ where d_m is defined as $d_{O_1-O_2} - (R_1 - R_2)$ where $d_{O_1-O_2}$ is the distance between the centres of the two track circles in the transverse plane and R_1 and R_2 are the two circles radii.

Further requirements include a small z separation between the tracks innermost points ($|\Delta z| < 5cm$) if they are in the barrel ($|z| < 120cm$) and a small opening angle in the longitudinal plane ($|\Delta \cot\theta| < 0.1$).

The two candidate conversion tracks must have one of the innermost two hits in the same detector layer. This to reduce the contribution of fake conversions due to soft displaced tracks that are artificially backward propagated.

Each conversion track candidate must be compatible in z, within five standard deviations, with at least one reconstructed primary vertex. Moreover the primary vertex closest in z to each track must be one of the two closest primary vertex of the other track.

Track pairs surviving the selection are then fitted to a common 3D-constrained kinematic vertex fitter. The 3D constraints imposes the tracks to be parallel in both transverse and longitudinal planes. The pair is retained if the fit converges and its χ^2 probability is greater than 5×10^{-4}.

For the present analysis only reconstructed conversion with a vertex transverse distance larger than $1.5cm$ with respect to the nominal beam spot are considered. This cut allows for the background contribution due to π_0 Dalitz decay to be suppressed while retaining photon conversion possibly occurring within the beam pipe volume.

The conversion reconstruction algorithm described above is not protected against the occurrence of a track shared among two or more reconstructed conversion. In this case only the conversion with the larger χ^2 probability is retained.

The p_t and η distribution of the reconstructed photon conversion are shown in Fig. 4.16. In Fig. 4.17 the position of the reconstructed conversion in the transverse plane is shown.

A reconstructed primary vertex is assigned to the photon reconstructed via the reconstruction of the conversion by extrapolating the reconstructed photon momentum and by choosing the closest vertex. If the distance is larger than ten standard deviations the conversion is rejected. The primary vertex associated to the conversion is required to be compatible with the reconstructed J/ψ vertex by asking their distance to be compatible within five standard deviations; furthermore, none of the two candidate muon tracks building the J/ψ vertex up must be the candidate electron or positron track of the reconstructed conversion vertex.

Finally each conversion candidate is associated to every other conversion candidate in the event, and to any Particle-Flow reconstructed photon. Particle-Flow photons are photons identified with the Particle-Flow algorithm.

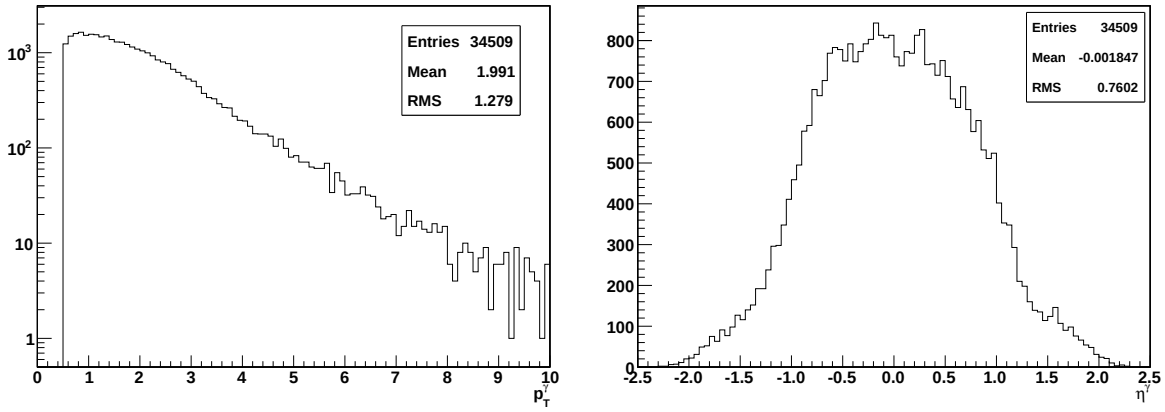

Figure 4.16: Distribution of p_T and η of the reconstructed photon conversion.

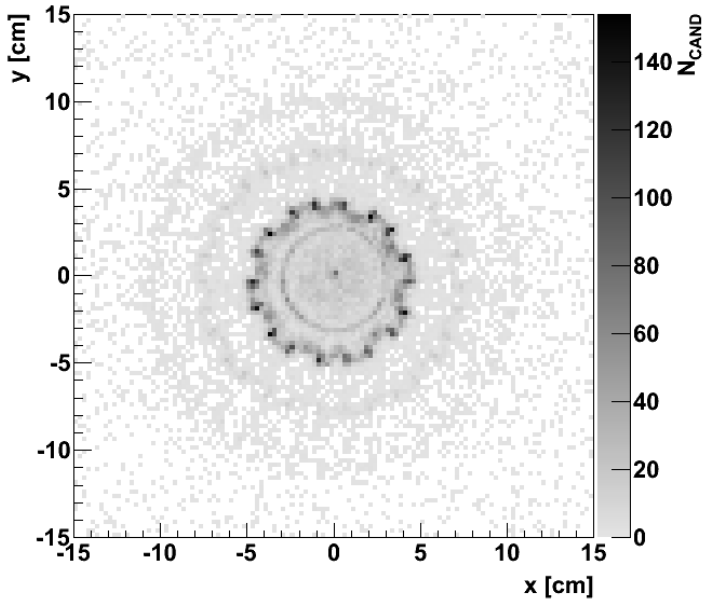

Figure 4.17: Distribution of the recostructed conversion vertex in the transverse plane.

The Particle-Flow algorithm consist in combining the information of the inner tracker, the electromagnetic and hadron calorimeter to try and associate to every track a cluster in the calorimeters. Once this step has been performed the ECAL clusters that weren't associated to any track are classified as Particle-Flow photons. This kind of photon identification is pretty loose allowing a high rate of fake photons.

If the resulting invariant mass of the pair falls in the mass range between $0.1GeV$ and $0.2GeV$ the conversion is rejected since it assumed to be compatible with a π_0 decay photon.

Further details on tracker physics performances and conversion reconstruction can be found in [9] [8] [7].

4.3 Data Analysis

To extract the number of χ_{c1} and χ_{c2} from data, an unbinned likelihood fit to the mass difference spectrum is performed in various p_T ranges using ROOFIT. The signal is modeled using a superposition of three Crystal Ball functions for χ_{c0}, χ_{c1} and χ_{c2}.

$$f_{CB}(m) = \begin{cases} e^{-\frac{(m-m_0)^2}{2\sigma}}, \text{ for } \frac{m-m_0}{\sigma} > \alpha \\ (n/\alpha)^n e^{-\alpha^2/2}(\frac{n}{\alpha} - \alpha - \frac{m-m_0}{\sigma})^{-n}, \text{ for } \frac{m-m_0}{\sigma} \leq \alpha \end{cases} \tag{4.2}$$

Each Crystal Ball function has four parameters: α, n, σ and m. Due to the small intrinsic width of the states investigated, the observed signal shape is dominated by the experimental resolution. The same α, n and σ is assigned to all three resonance shapes. The m parameter for the χ_{c1} is left free, while for the χ_{c2} and χ_{c0} it is fixed to $m_{\chi_{c2}} - m_{\chi_{c1}}$ and $m_{\chi_{c1}} - m_{\chi_{c0}}$, respectively, obtained from the PDG [14].

The combinatorial background is modelled by a probability distribution function of the kind

$$N_{bkg} = (x - q_0)^{\alpha_1} \cdot e^{(x-q_0)\cdot\beta_1} \tag{4.3}$$

where α_1 and β_1 are free parameters and q_0 is fixed to $3.2GeV$. In Figure 4.18 the measured mass difference spectrum for $p_T^{J/\psi}$ between $7GeV$ and $25GeV$ is shown. This procedure is repeated for several ranges of p_T of the J/ψ in order to extract $N_{\chi_{c1}}$ and $N_{\chi_{c2}}$. The results are shown in Table 4.1, where errors are statistical only. In Figure 4.19 is reported the invariant mass spectrum and fit for each $p_T^{J/\psi}$ bin.

$p_T^{J/\psi}[GeV]$	$N_{\chi_{c1}}$	$N_{\chi_{c2}}$
7.0-10.0	1139 ± 57	503 ± 40
10.0-13.0	2133 ± 75	944 ± 52
13.0-16.0	1189 ± 59	542 ± 40
16.0-19.0	631 ± 32	218 ± 21
19.0-22.0	391 ± 36	174 ± 26
22.0-25.0	157 ± 15	66 ± 11
7.0-25.0	6040 ±135	2588 ±91

Table 4.1: Number of χ_{c1} and χ_{c2} extracted from the maximum likelihood fit. Errors are statistical only.

In Appendix C it is reported the relevant piece of PYTHON code used to perform the unbinned fit. The pyROOT python wrapper to the ROOT framework is used alongside with the ROOFIT library to perform the unbinned fit.

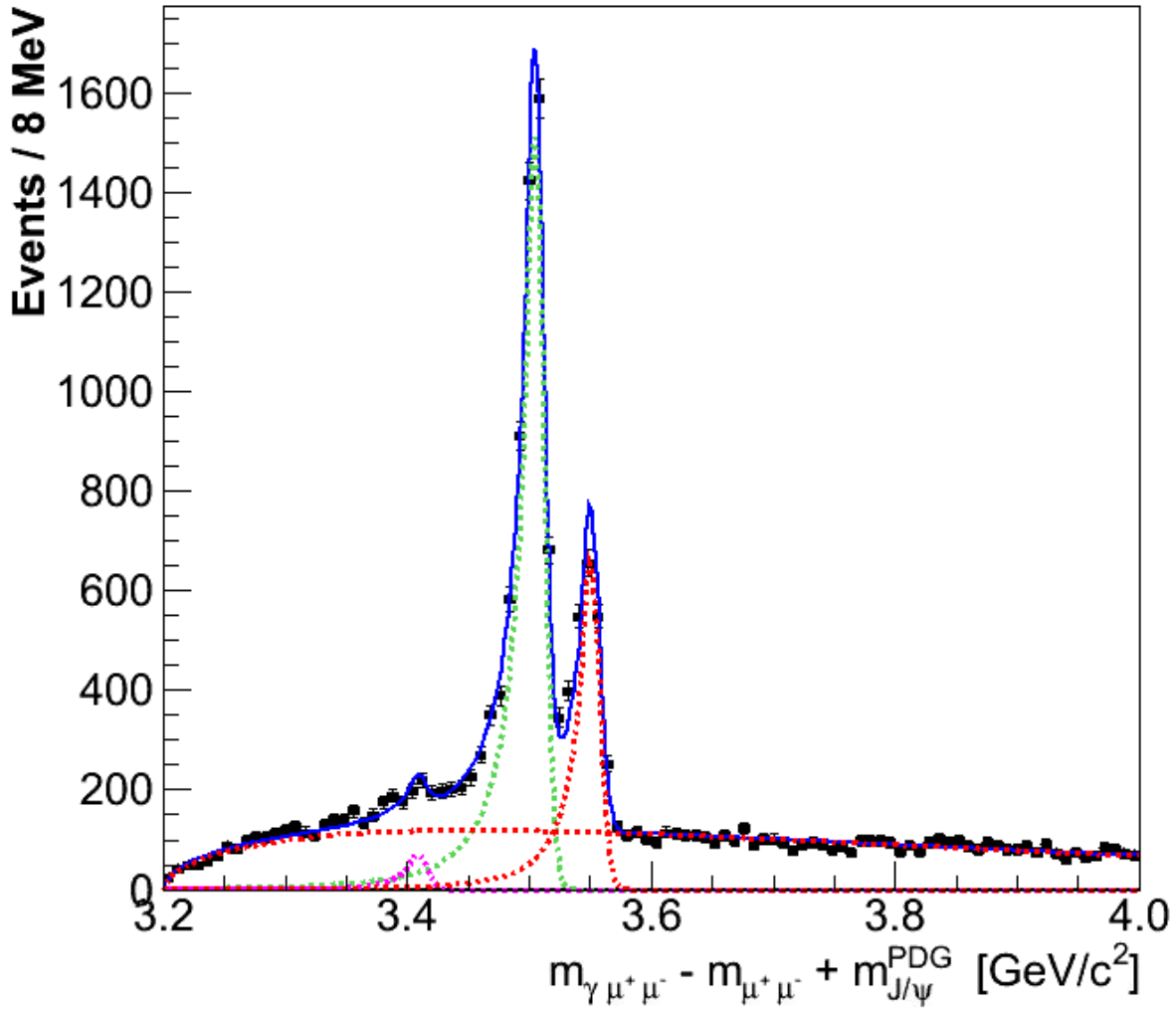

Figure 4.18: Mass difference spectrum for χ_c candidates with $p_T^{J/\psi}$ between $7.0GeV$ and $25.0GeV$. Purple line is χ_{c0}, green line is χ_{c1}, red line is χ_{c2}

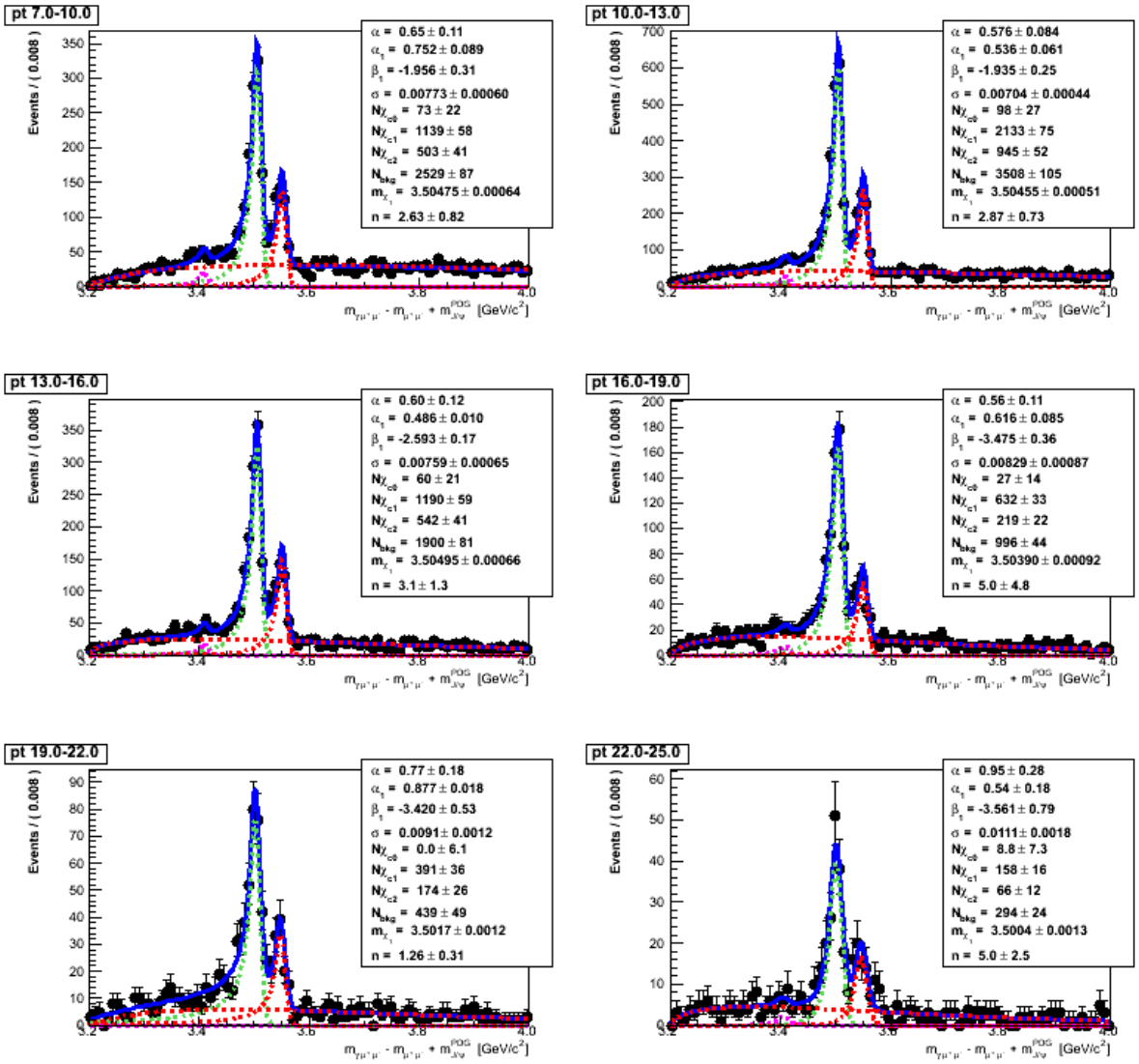

Figure 4.19: Mass difference spectrum for χ_c candidates in various $p_T^{J/\psi}$ bins

A variety of plots on χ_c candidates are reported on Appendix B while event displays on χ_c candidates are reported on Appendix A.

4.4 Acceptances and Efficiencies

In the calculation of the ratio, the possibility that the acceptance ϵ_i due to geometry, photon conversion probability and reconstruction efficiency is not the same for the χ_{c1} and the χ_{c2} (i.e. $\epsilon_1 \neq \epsilon_2$) must be taken into account.

In order to determine acceptance corrections, a Monte Carlo sample using a PYTHIA particle gun is prepared to generate χ_{c1} and χ_{c2} alternatively, with the same p_T spectrum measured for the J/ψ. The systematic error on $\frac{\epsilon_1}{\epsilon_2}$ which may derive from this assumption is discussed in the section regarding systematic errors. Both states are forced to decay to $J/\psi\gamma$. The decay products are then propagated to the full CMS detector simulation,

trigger selection and reconstruction. In order to increase computing efficiency, only events in which a conversion occurs are passed to trigger emulation and reconstruction. In Fig. 4.21 the mass difference spectrum obtained from this simulation is shown.

The ratio of efficiencies for the different bins of p_T of the J/ψ, is obtained as:

$$\frac{\epsilon_1}{\epsilon_2}(p_T^{J/\psi}) = \frac{\frac{N^{rec}_{\chi_{c1}}}{N^{gen}_{\chi_{c1}}}}{\frac{N^{rec}_{\chi_{c2}}}{N^{gen}_{\chi_{c2}}}}$$

where N^{rec} is the number of candidates reconstructed with the selection above, and N^{gen} is the number of Montecarlo generated candidates in the kinematic range $|y^{J/\psi}| < 1.0, p_T^{\gamma} > 0.5GeV$. The resulting values are shown in Table 4.2, where the error due to the limited size of the simulation sample is binomial.

21673296 events have been generated, resulting in 43886 reconstructed χ. This approach also allowed to study photon conversion probability and reconstruction efficiency, shown in Figure 4.20 as a function of p_T of the photon. The method described above has the advantage of allowing the generation of a large sample of χ_{c1} and χ_{c2}, but it reproduces a somewhat idealized condition, in particular inasmuch as the sample is completely free of background. To check the consistency of the results, another PYTHIA sample generated, in which the entire pp collision is reproduced has been used.

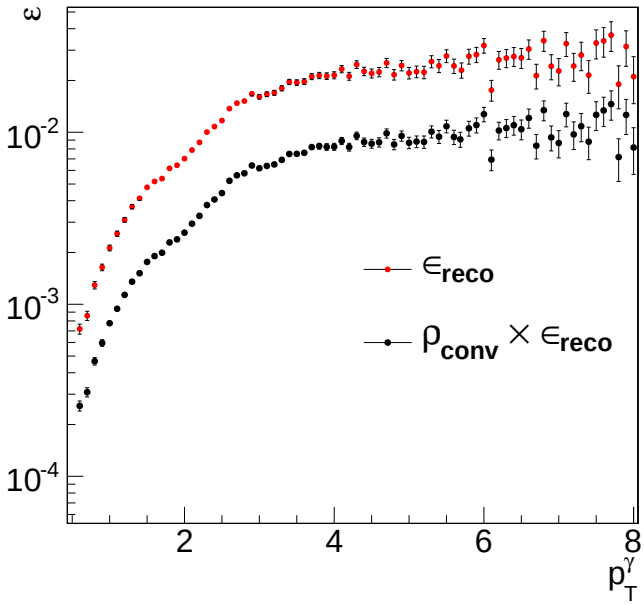

Figure 4.20: Efficiency of photon conversion reconstruction and product of conversion probability and reconstruction efficiency as a function of photon transverse momentum measured with PYTHIA particle gun.

The ratio ϵ_1/ϵ_2, which is actually the ratio of the geometric acceptances times the ratio of the reconstruction efficiencies, is influenced by:

$p_T^{J/\psi[GeV]}$	ϵ_1/ϵ_2
7.0-10.0	0.931 ±0.022
10.0-13.0	0.927 ±0.016
13.0-16.0	0.939 ±0.018
16.0-19.0	0.935 ±0.022
19.0-22.0	0.967 ±0.028
22.0-25.0	0.898 ±0.030
7.0-25.0	0.946 ±0.009

Table 4.2: Ratio of efficiencies ϵ_1/ϵ_2 measured with PYTHIA particle gun. Errors are statistical only.

1. Slightly different acceptance for the muon pair originating from the J/ψ when the latter is a decay product of the χ_{c1} or χ_{c2}.

2. Different p_T spectrum of the emitted photon.

From the study of the $\chi_{c1,c2}$ gun sample, it can be seen that the different acceptance of the analysis for the two states resides mostly in the reconstruction efficiency for the converted photon. While the dimuon spectra do not show significant differences for the two states, the higher mass of the χ_{c2} results in a significantly harder p_T spectrum of the photon. The situation is illustrated by Figure 4.22. As to provide further evidence of the fact that the ratio of acceptances is driven by the photon reconstruction efficiency, the ratio of reconstruction efficiencies is calculated for J/ψ coming from χ_{c1} and χ_{c2}, by comparing the number of generated and reconstructed J/ψ. The ratio $\frac{\epsilon_1^{J/\psi}}{\epsilon_2^{J/\psi}}$ is found to be close to unity in all pt ranges. The measurement is illustrated in figure 4.23.

In Figure 4.24 and 4.25 are reported event displays of the generated χ_c decays.

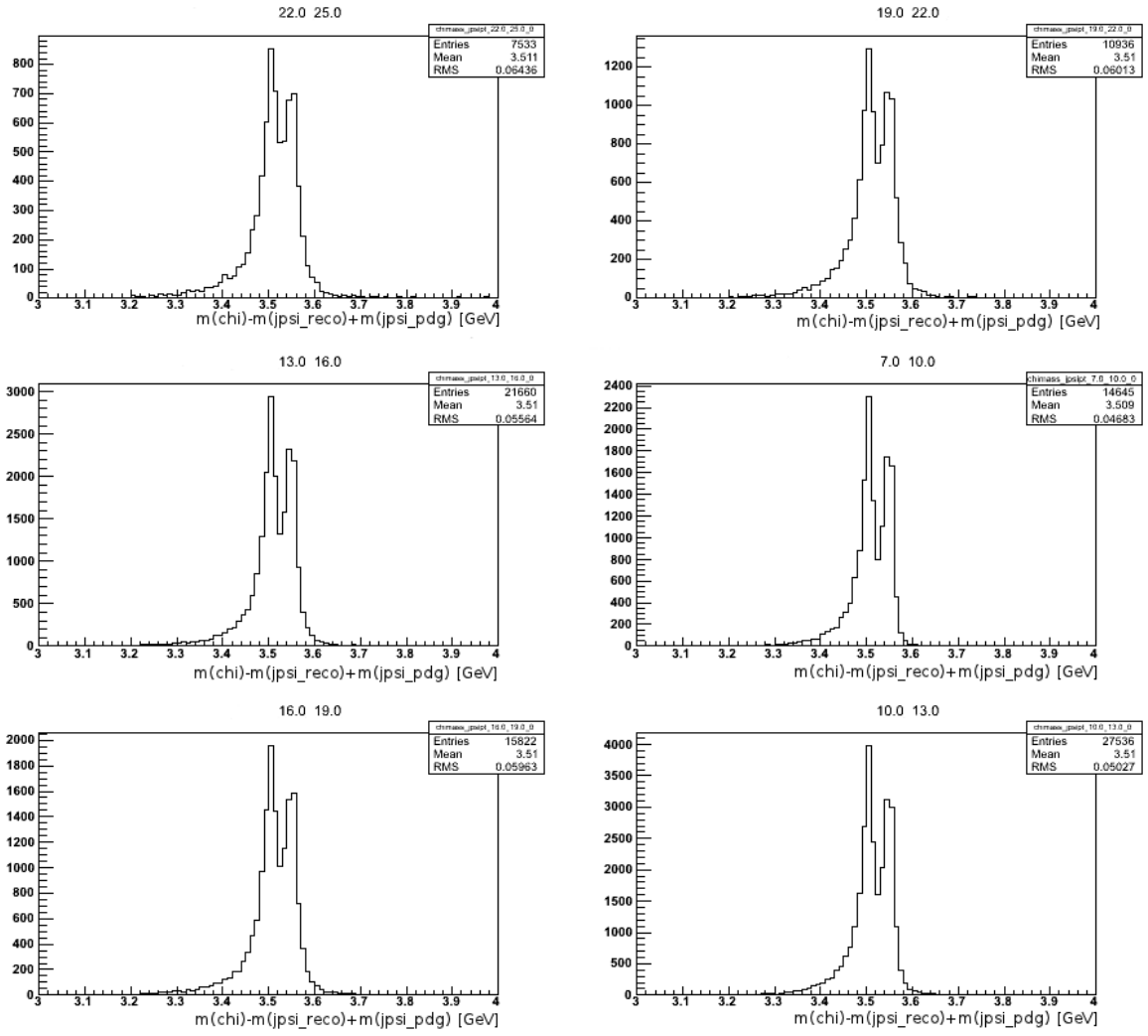

Figure 4.21: Mass difference spectra obtained with the particle gun simulation for χ_{c1} and χ_{c2} in various p_T bins.

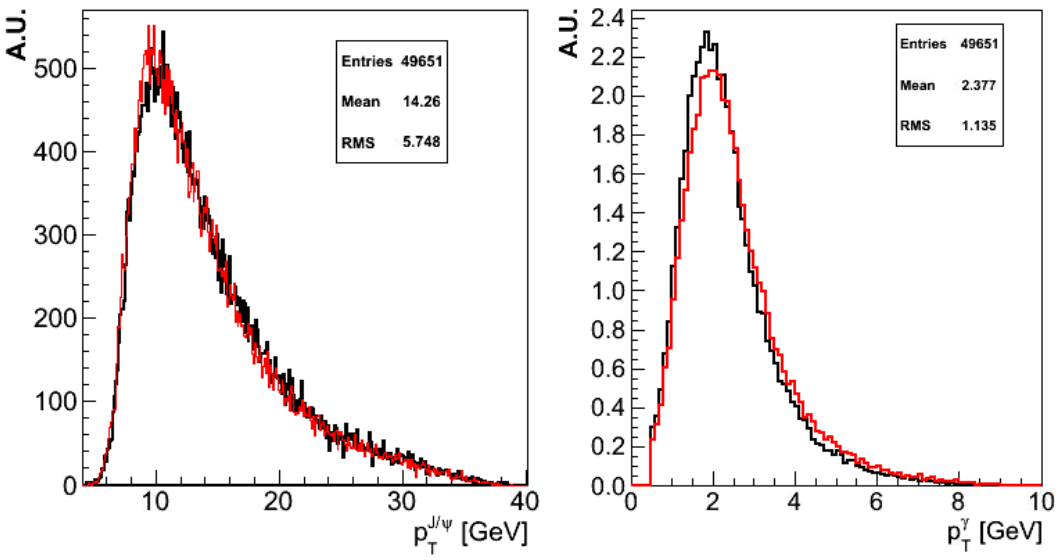

Figure 4.22: Left: p_T distribution of the J/ψ from the decay of χ_{c1} (black) and χ_{c2} (red) generated with a PYTHIA particle gun and passed through the complete CMS simulation and reconstruction. Right: p_T distribution of the photon from χ_{c1} (black) and χ_{c2} (red) generated with the same technique.

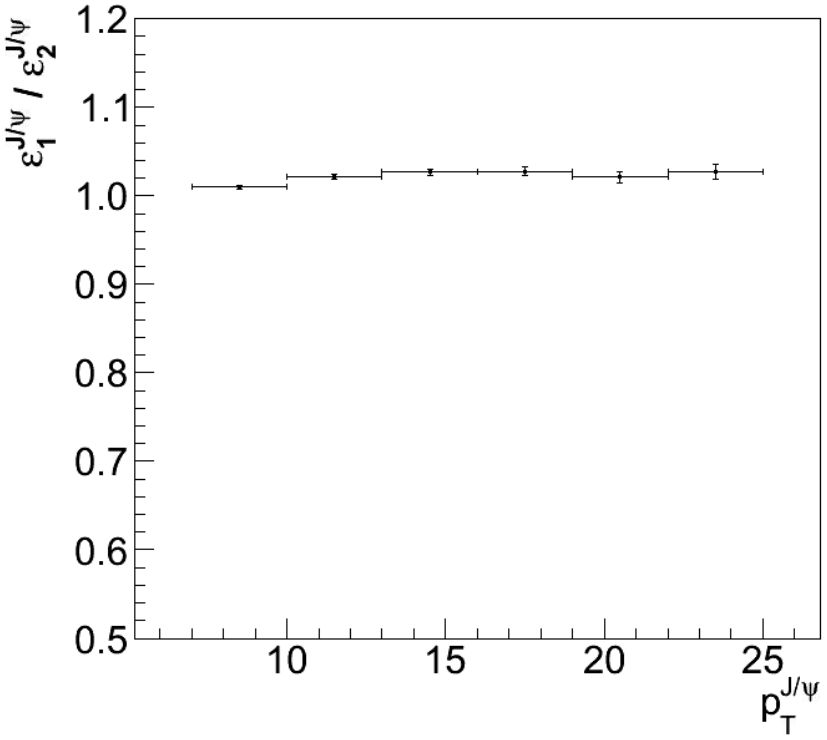

Figure 4.23: Ratio of efficiencies for J/ψ detection for J/ψ generated from simulated χ_{c1} and χ_{c2}

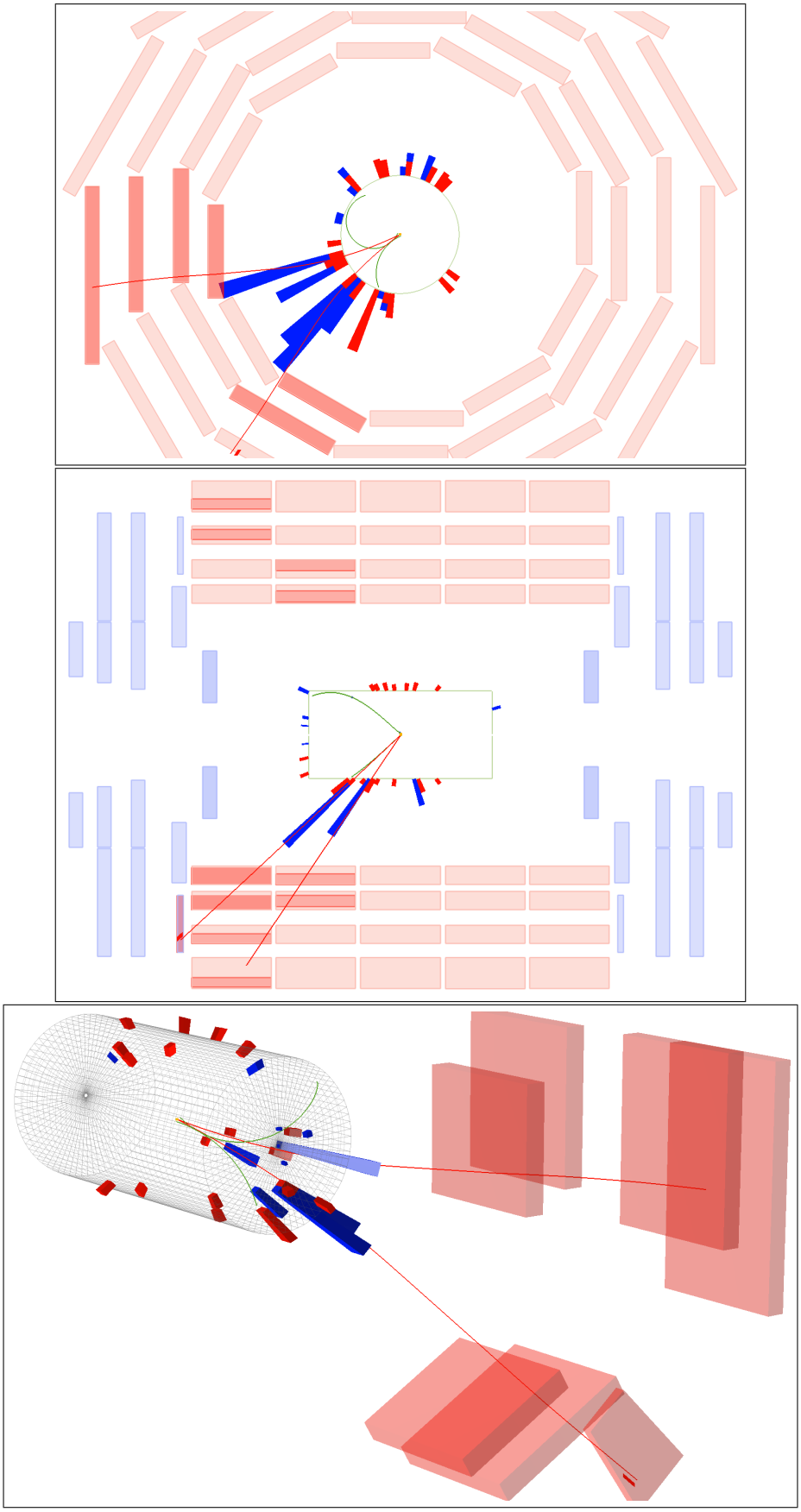

Figure 4.24: Event display of the generated χ_c decays with particle gun.

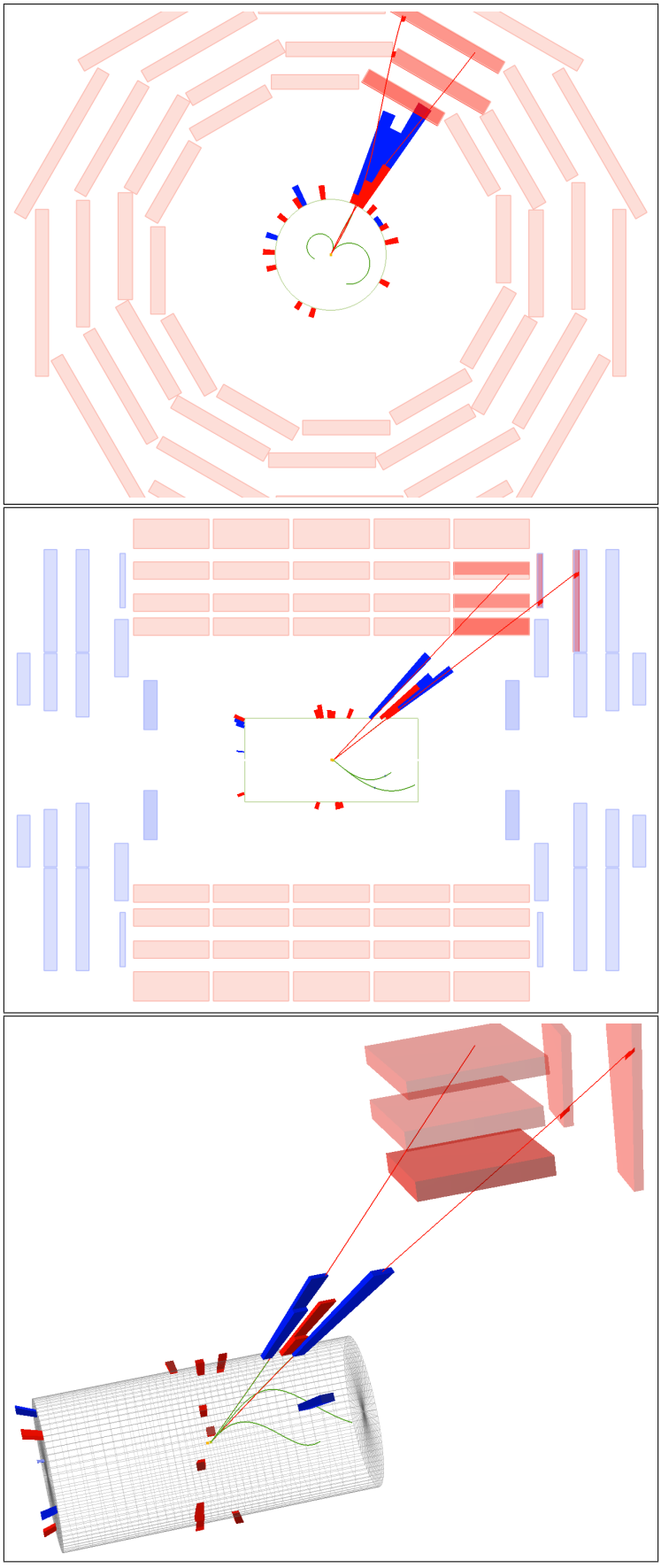

Figure 4.25: Event display of the generated χ_c decays with particle gun.

For the sake of completeness here it is reported the the relevant PYTHIA settings used to force the decay of the χ_c mesons in the desired one:

```
MSEL=61          ! Quarkonia
MDME(858,1)=0    ! J/psi -> ee turned OFF
MDME(859,1)=1    ! J/psi -> mumu turned ON
MDME(860,1)=0    ! J/psi -> random turned OFF
BRAT(861)=1.0    ! chi_2c->J/psi gamma
BRAT(862)=0.0    ! chi_2c->rndmflav rndmflavbar
BRAT(1501)=0.0   ! chi_0c->J/psi gamma
BRAT(1502)=0.0   ! chi_0c->rndmflav rndmflavbar
BRAT(1555)=1.0   ! chi_1c->J/psi gamma
BRAT(1556)=0.0   ! chi_1c->rndmflav rndmflavbar
```

4.5 Systematic Uncertainties

Several types of systematic uncertainties have been evaluated that might affect the measurement of the number of χ_{c1} and χ_{c2} from data and the evaluation of $\frac{\epsilon_1}{\epsilon_2}$ from the Monte Carlo.

4.5.1 Uncertainty from mass fit and χ_{c1} and χ_{c2} counting

To investigate the uncertainties on the fraction χ_{c1} and χ_{c2} deriving from the choice of fit function, several parametrizations of the mass difference spectrum have been used.

The way the parametrization of the background influences the ratio N_{χ_1}/N_{χ_2} has been investigated. To do so, a polynomial function and a Chebichev function have been used to describe the background. The ratio $N_{\chi c2}/N_{\chi c1}$ measured with these different choices is found to be within statistical error from the results obtained with the reference PDF.

Finally, instead of constrain the fit to use the same σ parameter for all three Crystal Ball functions, the case in which the resolution is potentially different for the χ_{c1} and χ_{c2} is explored by introducing another free parameter σ_2 for the Crystal ball describing the χ_{c2}. The results are found to vary within statistical error and the χ^2 of the fit to remain substantially unchanged.

To further validate the capability of the method to discern and count correctly χ_{c1} and χ_{c2} states, a PYTHIA-generated Monte Carlo sample is used, it is fed to the full CMS simulation and reconstruction chain. The true number of candidates of one state or the other, as extracted from the generator information, is consistent with the number derived from the fit to the reconstructed candidates. The PYTHIA sample was produced using the ability of the generator to reproduce the details of pp collisions leading to a J/ψ decaying to two muons in the final state. The sample could be used for consistency checks only, given the low yield of χ_c decaying to $J/\psi\ \gamma$ due to the small reconstruction efficiency. The statistical error on the ϵ_2/ϵ_1 ratio would be too big. For the same reason, it's possible to perform the check only in the first three bins in p_T.

The mass difference spectra obtained from this Monte Carlo are shown in figure 4.26 with the fit superimposed. In table 4.3 it is presented the number of χ_c candidates of each type from the Monte Carlo truth and from the same maximum likelihood approach

$p_T^{J/\psi}$	N_{χ_1}/N_{χ_2} Monte Carlo	N_{χ_1}/N_{χ_2} Fit	Relative difference
7-10	0.521 ± 0.037	0.515 ± 0.041	1.1%
10-13	0.405 ± 0.039	0.431 ± 0.047	6.0%
13-16	0.434 ± 0.067	0.445 ± 0.074	2.5%
16-19	0.474 ± 0.108	0.478 ± 0.121	0.8%

Table 4.3: A study on the full Monte Carlo to measure the accuracy of the maximum likelihood fit to discern χ_{c1} and χ_{c2}. Columns labeled "Monte Carlo" refer to the number of candidates as from the Monte Carlo truth. Columns labeled "Fit" refer to the number of candidates extracted from the fit procedure.

used with data. It is found that the result obtained with the fit is within statistical error from the Monte Carlo truth in all the p_T bins that was possible to explore with the given statistics.

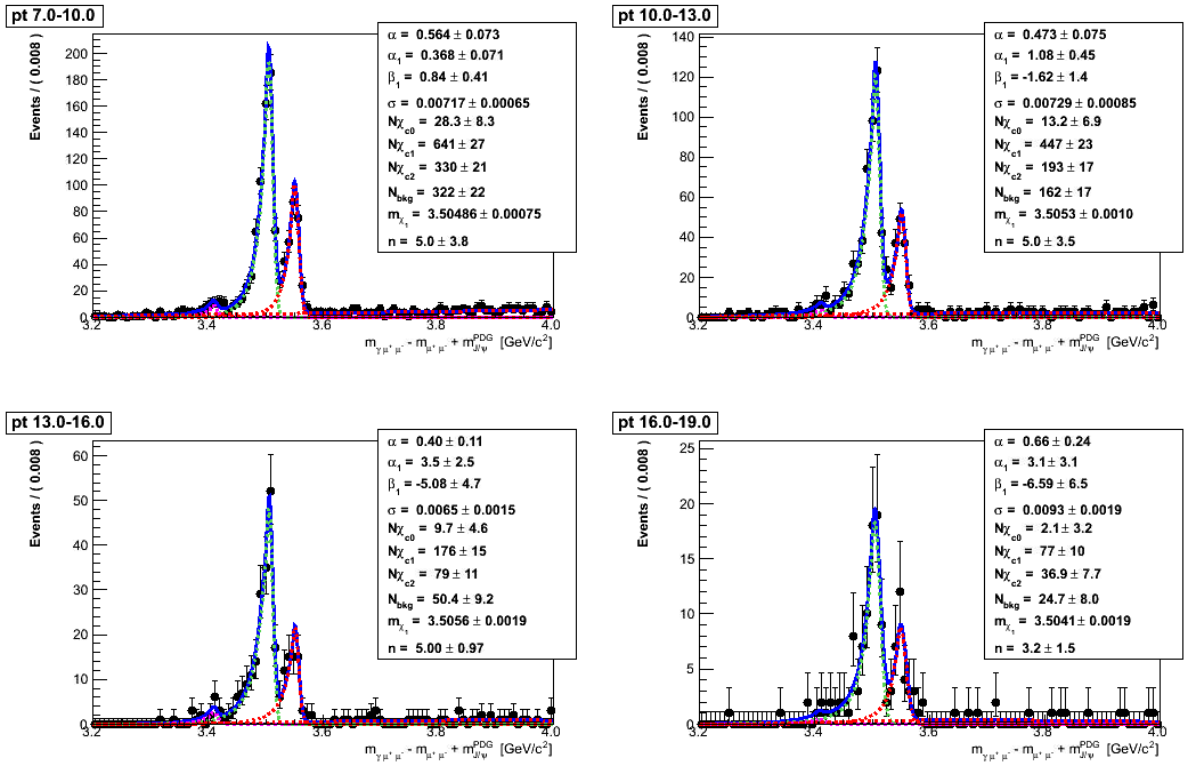

Figure 4.26: Fits to the mass difference spectra of the full Montecarlo sample in various bin of p_T

4.5.2 Uncertainty on ratio of efficiencies

Several sources of systematic uncertainties on $\frac{\epsilon_1}{\epsilon_2}$ deriving from the simulation are considered.

$p_T^{J/\psi}$	ϵ_1/ϵ_2 full Monte Carlo	ϵ_1/ϵ_2 particle gun	Relative difference
7.0-10.0	0.919 ± 0.055	0.931 ±0.022	1.3%
10.0-13.0	0.886 ± 0.065	0.927 ±0.016	4.6%
13.0-16.0	0.781 ± 0.089	0.939 ±0.018	17%
16.0-19.0	0.720 ± 0.114	0.935 ±0.022	23%
7.0-25.0	0.948 ±0.037	0.946 ±0.009	0.2%

Table 4.4: A study on the full Monte Carlo to measure ϵ_1/ϵ_2.

Firstly, it is evaluated the systematic error coming from the choice of simulation sample. To do so, the results obtained with the χ_c gun simulation are compared with the full simulation sample described above. The values obtained are shown in Table 4.4. The full Monte Carlo sample does not provide sufficient statistics to derive a systematic error in each p_T bin. When considering all the candidates in the $p_T^{J/\psi}$range [7.0,25.0] GeV, the value of the ratio of efficiencies $\frac{\epsilon_1}{\epsilon_2}$ is 0.948 ±0.037. Since the two values are statistically consistent, it is not assigned a systematic error.

It is estimated the uncertainty coming from a possible incorrect simulation of detector (tracker) material. To do so, the particle gun Monte Carlo is run with two modified material scenarios. These scenarios correspond to the hypothesis that 5% of the mass of the tracker is not represented in the simulation, which translates to maximum local variation of the radiation length X_0 of +8% -7%. In figure 4.27 it is presented the radius of conversion for Montecarlo produced events for three material scenarios: default, X_0^{min}, X_0^{max}. An extremely accurate representation of the geometry and material distribution of the detector is very difficult to obtain, however this aspect of the simulation is essential as conversion distribution of generated events may be affected by an imperfect material scenario. Thus this aspect is studied as a possible source of systematic error. In Figure 4.27 are reported η and radius of photon conversions in different material scenarios. ϵ_1/ϵ_2 is compared in the three cases : default material budget, high X_0 scenario, low X_0 scenario. The values are respectively : 0.955 ± .007, 0.048± 0.009, 0.951 ± 0.009. The three values are the same within statistical error, therefore it is not assigned a systematic error from this source of uncertainty.

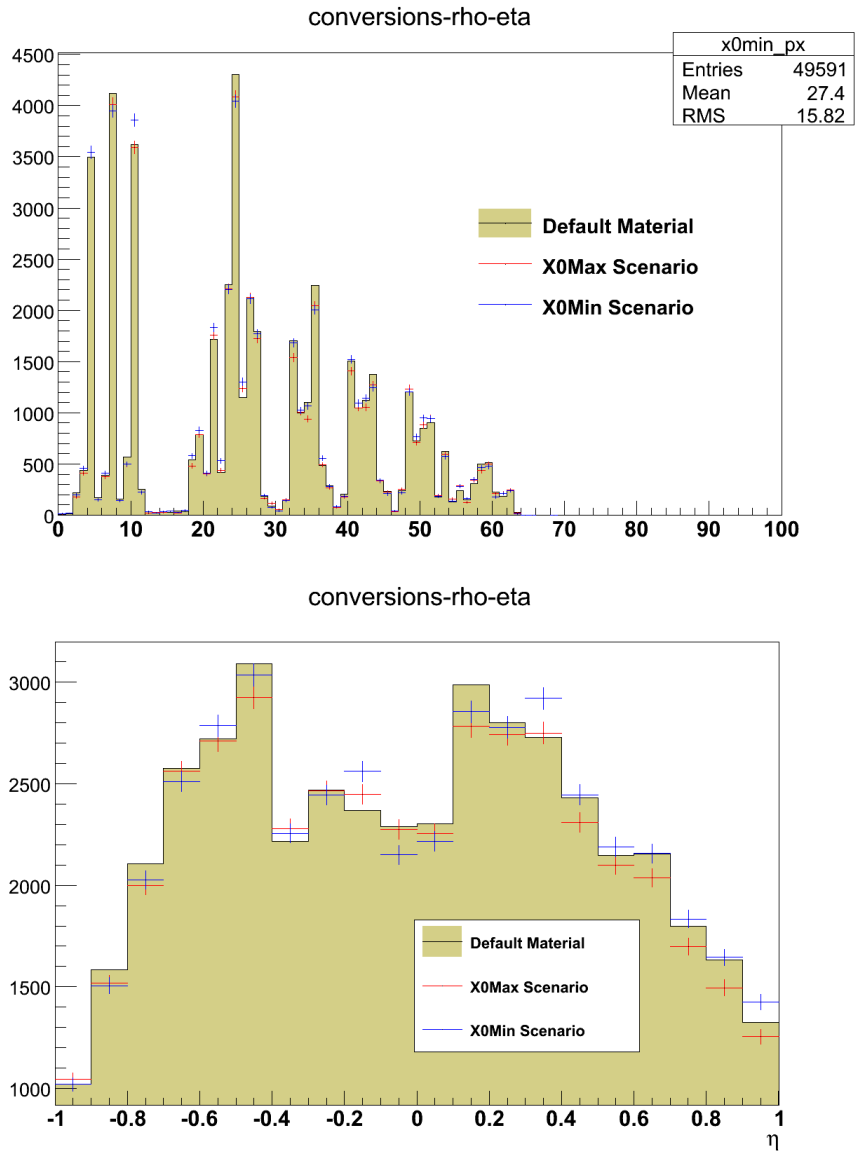

Figure 4.27: Radius and η of conversion of photons from Montecarlo produced events for three material scenarios

It is also tested the effect of assuming, in χ_c gun simulations, that the χ_{c1} and χ_{c2} have the same p_T distribution as the J/ψ. To do so, it is measured the p_T spectrum of the ψ' and produced a simulation in which the χ_c has the same p_T spectrum of the ψ'. The two p_T shapes are shown in Figure 4.28 The values of ϵ_1/ϵ_2 recalculated with this assumption are reported in table 4.5, along with the differences with respect to the default calculation. Again the difference is overstated by the statistical errors thus it is not assigned a systematic error.

$p_T^{J/\psi}$	ϵ_1/ϵ_2 with $p_{T\psi'}$	ϵ_1/ϵ_2 standard	Relative difference [%]
7.0-10.0	0.923 ±0.027	0.931 ±0.022	0.9%
10.0-13.0	0.920 ±0.020	0.927 ±0.016	0.8%
13.0-16.0	0.968 ±0.023	0.939 ±0.018	3.0%
16.0-19.0	0.935 ±0.028	0.935 ±0.022	0.0%
19.0-22.0	0.968 ±0.036	0.967 ±0.028	0.10%
22.0-25.0	0.972 ±0.046	0.898 ±0.030	8.2%

Table 4.5: The values of ϵ_1/ϵ_2 obtained from a χ gun simulation in which the two states are generated with a p_T distribution that follows the measured p_T distribution of the ψ'

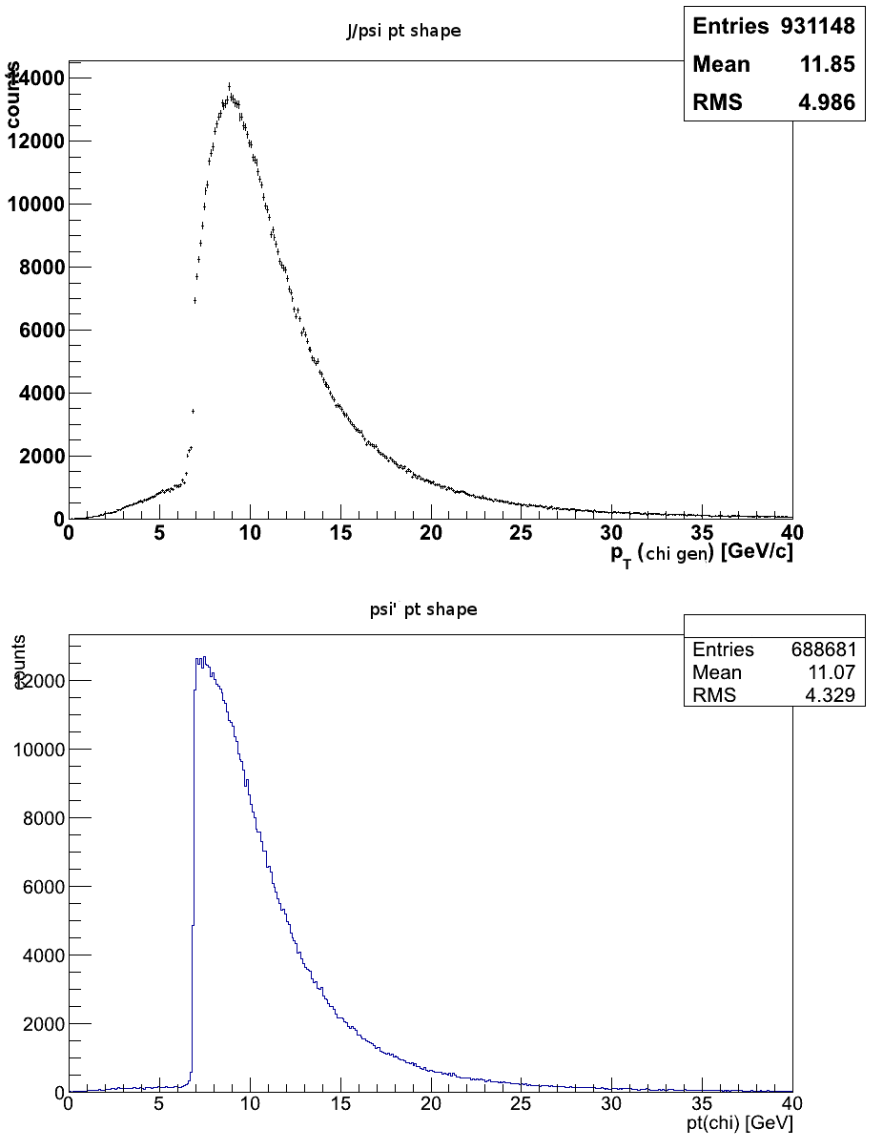

Figure 4.28: χ_c p_T shapes used to study systematics on p_T distribution. Above: p_T shape from J/ψ. Below: shape from ψ'

4.5.3 Pileup

As already described in the analysis strategy section of this chapter the instantaneous luminosity of LHC runs varied with time. The higher luminosity due to more squeezed beams and possibly a higher number of protons per bunch made the pileup (i.e. the number of primary vertices recorded for each event) higher. In this section the eventual dependence of the results of this analysis from the pileup is studied.

The stability of the analysis as a function of the number of primary vertices in the event is examined. It is checked that the number of candidates per unit of integrated luminosity, once trigger conditions are taken into account, has kept constant with varying instantaneous luminosity.

In Figure 4.29 it is plotted the number of primary vertices per event in Run 2011A and Run 2011B combined, in Figure 4.30 the same plot is shown for the two runs separately. It can be clearly seen that on average the Run 2011B has more primary vertices per event, thus more pileup.

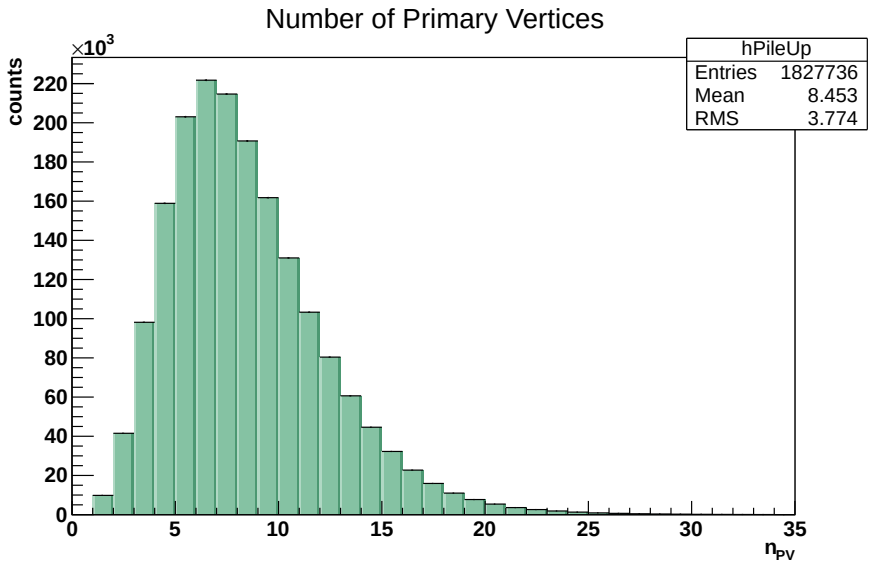

Figure 4.29: Distribution of the number of primary vertices per event for Run 2011A and Run 2011B combined

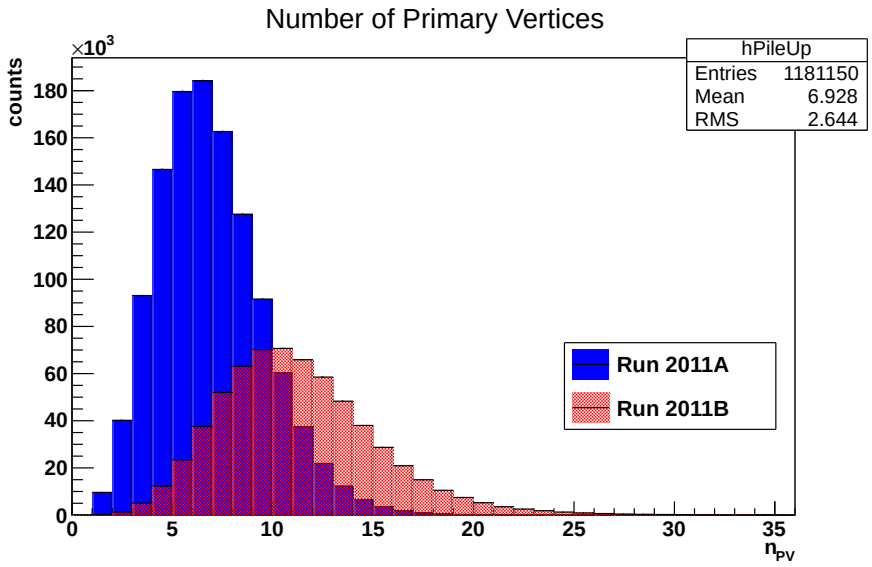

Figure 4.30: Distribution of the number of primary vertices per event for Run 2011A and Run 2011B separately

Now it is computed the ratio $R = N_{\chi c2}/N_{\chi c1}$ for events with at most n primary vertices for various values of n, R in function of n is plotted for Run 2011A and Run2011B together in Figure 4.31 and then for Run 2011A and Run 2011B separately in Figure 4.30.

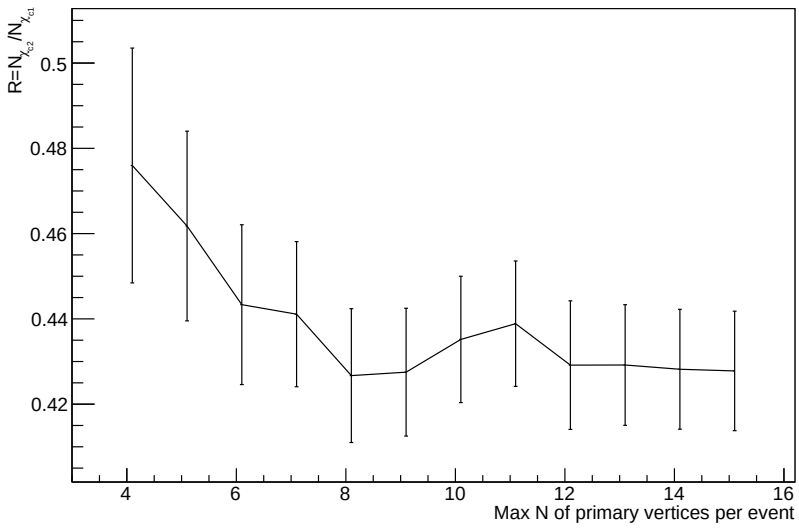

Figure 4.31: $R = N_{\chi c2}/N_{\chi c1}$ in function of the maximum number of primary vertices per event for Run 2011A and Run2011B together

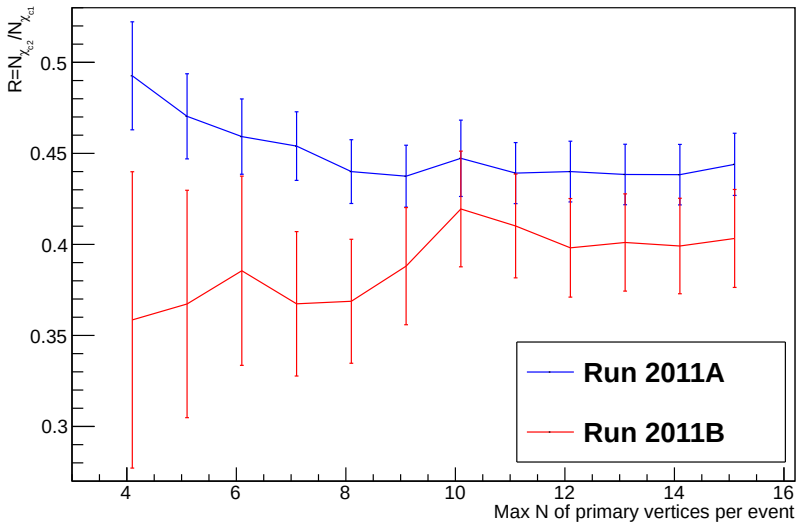

Figure 4.32: $R = N_{\chi_{c2}}/N_{\chi_{c1}}$ in function of the maximum number of primary vertices per event for Run 2011A and Run2011B separately

As can be seen from the previous pictures, while the ratio seems to be slightly influenced from the number of primary vertices in the event (pileup), the fluctuation lies within the statistical error, therefore it is not assigned a systematic uncertainty.

4.5.4 χ_c polarization

Another possible source of uncertainty is coming from the polarization of the χ_{c1} and χ_{c2}. The polarization of χ_{c1} and χ_{c2} when produced in hadron collisions is not known and there is no way to measure it with the detector. The different angular distribution of the photon may affect the photon p_T distribution, and, taken into account the photon detection efficiency, the total yield. To estimate the size of this uncertainty, a standalone Monte Carlo has been used by which it is possible to produce χ_{c1} and χ_{c2} in any polarization state. To take into account detector effects, the photon is weighted by the efficiency function, therefore using the approximation that the different efficiency for the two states is entirely due to the different photon spectrum. This exercise was made to estimate the size of the sensitivity of ϵ_1/ϵ_2 to polarization, and in particular to study the relative variation of ϵ_1/ϵ_2 with different polarization scenarios.

Therefore it is estimated ϵ_1/ϵ_2 for the cases in which the χ_{c1} is unpolarized or has helicity 0,$\pm$1 in combination with the χ_{c2} in unpolarized or helicity 0,$\pm$1 or $\pm$2 states, both in the helicity (HX) and Collins-Sooper (CS) frames. In Table 4.6 and 4.7 the values of ϵ_1/ϵ_2 are reported for the different polarization cases and helicity frames in each p_T bin. When quoting the final result, the maximum deviation from the unpolarized scenario as a possible systematic error is included.

Table 4.6: The values of ϵ_1/ϵ_2 for different polarization scenarios in the HX frame

	$p_T^{J/\psi} GeV/c$					
Polarisation scenario$(m_{\chi_{c1}}, m_{\chi_{c2}})$	$7-10$	$10-13$	$13-16$	$16-19$	$19-22$	$22-25$
$(Unpol, Unpol)$	0.877	0.833	0.878	0.920	0.941	1.002
$(Unpol, 0)$	1.014	0.890	0.926	0.894	0.876	1.129
$(Unpol, \pm 2)$	0.798	0.711	0.774	0.812	0.750	1.003
$(0, Unpol)$	0.969	0.990	0.979	1.078	0.996	1.026
$(\pm 1, Unpol)$	0.921	0.791	0.869	0.867	0.801	0.942
$(0, 0)$	1.120	1.058	1.034	1.048	0.927	1.156
$(0, \pm 2)$	0.882	0.844	0.863	0.952	0.794	1.028
$(\pm 1, 0)$	1.064	0.845	0.917	0.843	0.746	1.061
$(\pm 1, \pm 2)$	0.838	0.675	0.766	0.766	0.639	0.943

Table 4.7: The values of ϵ_1/ϵ_2 for different polarization scenarios in the CS frame

	$p_T^{J/\psi} GeV/c$					
Polarisation scenario$(m_{\chi_{c1}}, m_{\chi_{c2}})$	$7-10$	$10-13$	$13-16$	$16-19$	$19-22$	$22-25$
$(Unpol, Unpol)$	0.889	0.959	0.899	0.880	0.895	0.847
$(Unpol, 0)$	0.846	0.876	0.830	0.843	0.827	0.873
$(Unpol, \pm 2)$	0.958	0.989	1.003	0.930	0.747	1.028
$(0, Unpol)$	0.826	0.856	0.720	0.838	0.792	0.833
$(\pm 1, Unpol)$	0.893	0.943	0.884	0.865	0.939	0.865
$(0, 0)$	0.786	0.782	0.665	0.803	0.731	0.859
$(0, \pm 2)$	0.890	0.883	0.804	0.885	0.660	1.011
$(\pm 1, 0)$	0.850	0.860	0.817	0.828	0.867	0.893
$(\pm 1, \pm 2)$	0.962	0.972	0.987	0.913	0.783	1.050

4.5.5 Branching fractions

The measurement of the ratio of the cross section is affected by the error on the branching ratios of the two states into $J/\psi\gamma$. The quantity directly accessible with the experiment is

$$\frac{\sigma(pp \to \chi_{c2})}{\sigma(pp \to \chi_{c1})} \times \frac{BR(\chi_{c2} \to J\psi\gamma)}{BR(\chi_{c1} \to J\psi\gamma)}$$

In order to extract the ratio of production cross section, the branching ratios from [14] is used with their errors, from which it is obtained $BR(\chi_{c1} \to J/\psi + \gamma)/BR(\chi_{c2} \to J/\psi + \gamma) = 1.76 \pm 0.10$.

In table 4.8 the various sources of systematic uncertainties are summarized and their contribution to the total uncertainty quoted in the final result.

$p_T^{J/\psi}$	σ_2/σ_1	$\sigma_2/\sigma_1 BR_1/BR_2$
7.0-10.0	$0.725\pm0.067\ \pm0.041\ ^{+0.059\ +0.205}_{-0.084\ -0.067}$	0.411±0.038
10.0-13.0	$0.724\ \pm0.047\ \pm0.041\ ^{+0.022\ +0.199}_{-0.134\ -0.140}$	0.410±0.026
13.0-16.0	$0.760\pm0.064\ \pm0.043\ ^{+0.087\ +0.136}_{-0.198\ -0.098}$	0.43±0.036
16.0-19.0	$0.570\pm0.073\ \pm0.032\ ^{+0.031\ +0.098}_{-0.050\ -0.095}$	0.323±0.041
19.0-22.0	$0.733\pm0.131\ \pm0.041\ ^{+0.035\ +0.043}_{-0.192\ -0.238}$	0.415±0.074
22.0-25.0	$0.689\pm0.156\ \pm0.039\ ^{+0.164\ +0.104}_{-0.011\ -0.041}$	0.391±0.088
7-25	$0.723 \pm 0.028\ \pm0.041$	0.409 ± 0.016

Table 4.9: The results of the measurement for the various values of $p_T^{J/\psi}$ for Run2011A and Run2011B combined. For σ_2/σ_1 the first error is statistical, the second is from the branching fractions uncertainty, the third is from the extreme polarization scenarios in the CS frame , the fourth from the extreme polarization scenarios in the HX frame

Source of systematic Uncertainty	Relative Uncertainty
Choice of fit functional form	Within statistical error
χ_{c1} / χ_{c2} counting accuracy	Within statistical error
Full simulation / particle gun	Within statistical error
Detector material	Within statistical error
Simulation sample size	Within statistical error
χ_{c1} χ_{c2} generated p_T	Within statistical error
Branching fractions	0.05

Table 4.8: The source of systematic uncertainties that were identified and quantified

4.6 Results

In table 4.9 the result for the measurement of $\frac{\sigma(pp\to\chi_{c2})}{\sigma(pp\to\chi_{c1})} \times \frac{BR(\chi_{c2}\to J\psi\gamma)}{BR(\chi_{c1}\to J\psi\gamma)}$ and $\frac{\sigma(pp\to\chi_{c2})}{\sigma(pp\to\chi_{c1})}$ are reported, for the kinematic range $p_T^\gamma > 0.5$ and $|y^{J/\psi}| < 1.0$, for data in RUN2011A and RUN2011B. The first error is statistical, and combines in quadrature the error from the fit and the statistical error on the ratio of efficiencies. The last column reports the variation in the ratio of acceptances ϵ_1/ϵ_2 in the two polarization scenarios that result in the maximum deviation from the unpolarized case. In Figure 4.33 a visual representation of the above table with statistical error is presented.

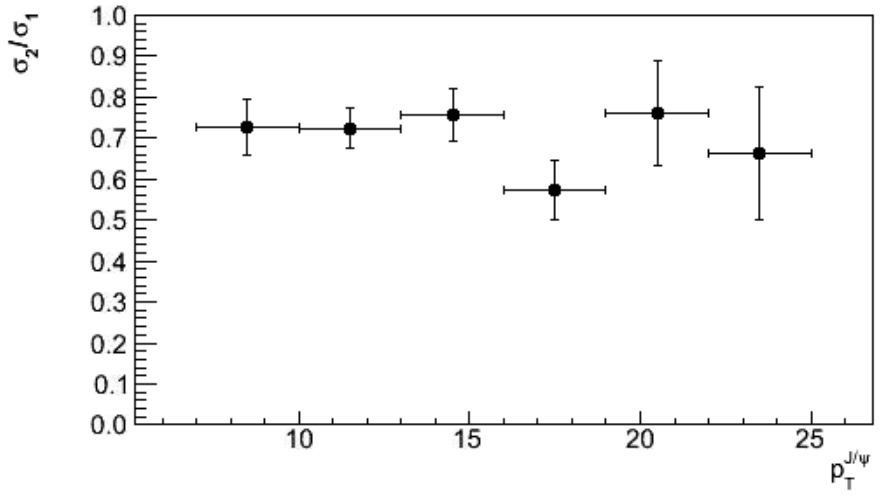

Figure 4.33: Cross section ratio for various p_T bins with statistical errors.

Chapter 5

Conclusions

The ratio $\sigma(pp \to \chi_{2c})/\sigma(pp \to \chi_{1c})$ has been measured in the CMS detector using the data taken during 2011.

Thanks to the excellent performance of the CMS tracking system, an excellent separation between the two states in the kinematical range $p_T^{\gamma} > 0.5GeV$, $|y^{J/\psi}| < 1.0$, $p_T^{J/\psi}$ was achieved. In particular the width of the χ_c peaks in the mass distribution is as low as $10MeV/c^2$, which represent the resolution of the inner tracker. This represent a success of the low energy conversion reconstruction algorithm achieved thanks to the robust performance of the inner tracker even in a scenario with low energy tracks and high track multiplicity in the events.

The ratio is found to be $R = \sigma(pp \to \chi_{2c})/\sigma(pp \to \chi_{1c}) = 0.723 \pm 0.028(stat) \pm 0.041(syst)$.

The ratio is corrected for efficiencies of reconstruction and acceptances. The correction has been performed through the use of a particle gun Montecarlo that provided enough statistics to obtain the efficiency ratio ϵ_1/ϵ_2 with enough precision.

Several possible sources of systematics errors have been examined in the analysis. Systematic errors on ϵ_1/ϵ_2 are smaller than the statistical fluctuations due to the limited size of the Montecarlo particle gun dataset.

The ratio has been obtained also in various bins of p_T of the J/ψ, this subdivision shows that the ratio is constant, within the statistical and systematic errors, in the range of p_T examined $(7 - 25GeV)$.

The ratio obtained is in agreement (within statistical and systematic uncertainties) with the value obtained at the CDF experiment at Tevatron. The study of χ_c states is useful to test theoretical models on quarkonium production and for studies of J/ψ production.

Appendix A

Event Displays

Here are reported some event displays of χ_c candidates taken from the 2011 run.

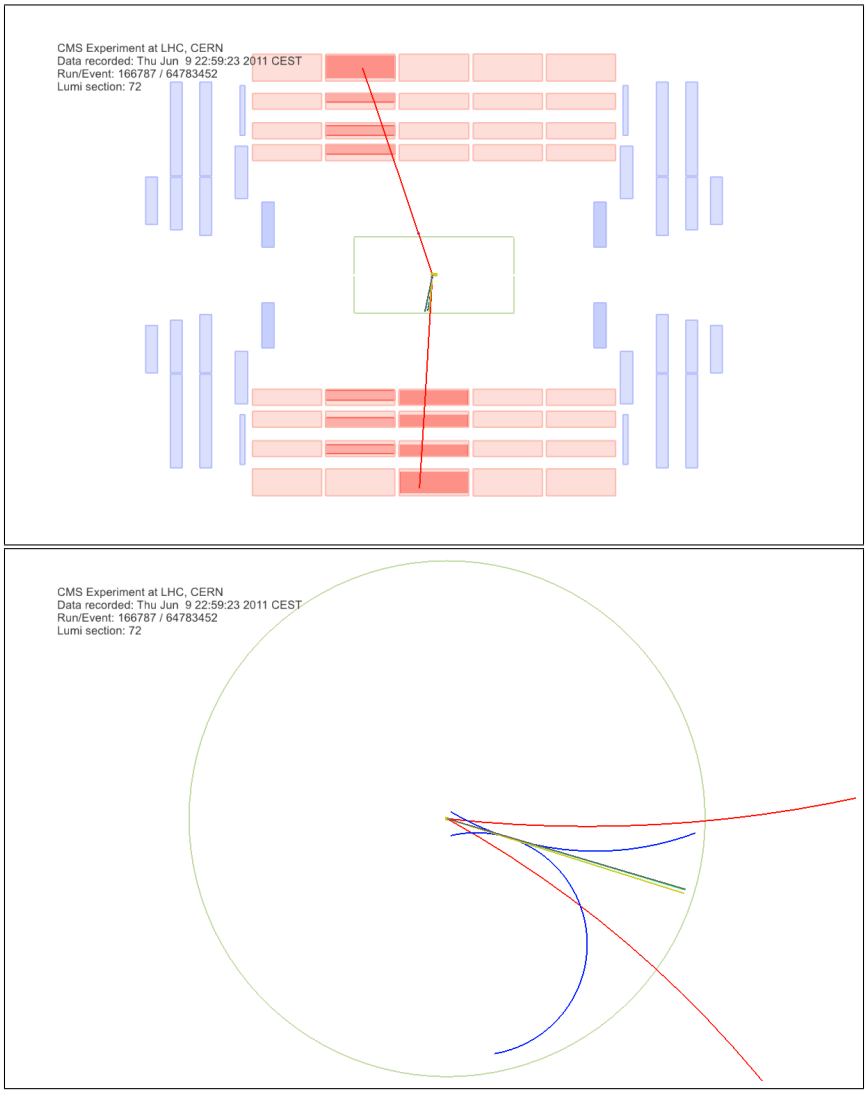

Figure A.1: Red: μ, yellow: γ candidate, blue: conversion e, light green: χ_c candidate, gray: J/ψ candidate, dark green: other tracks

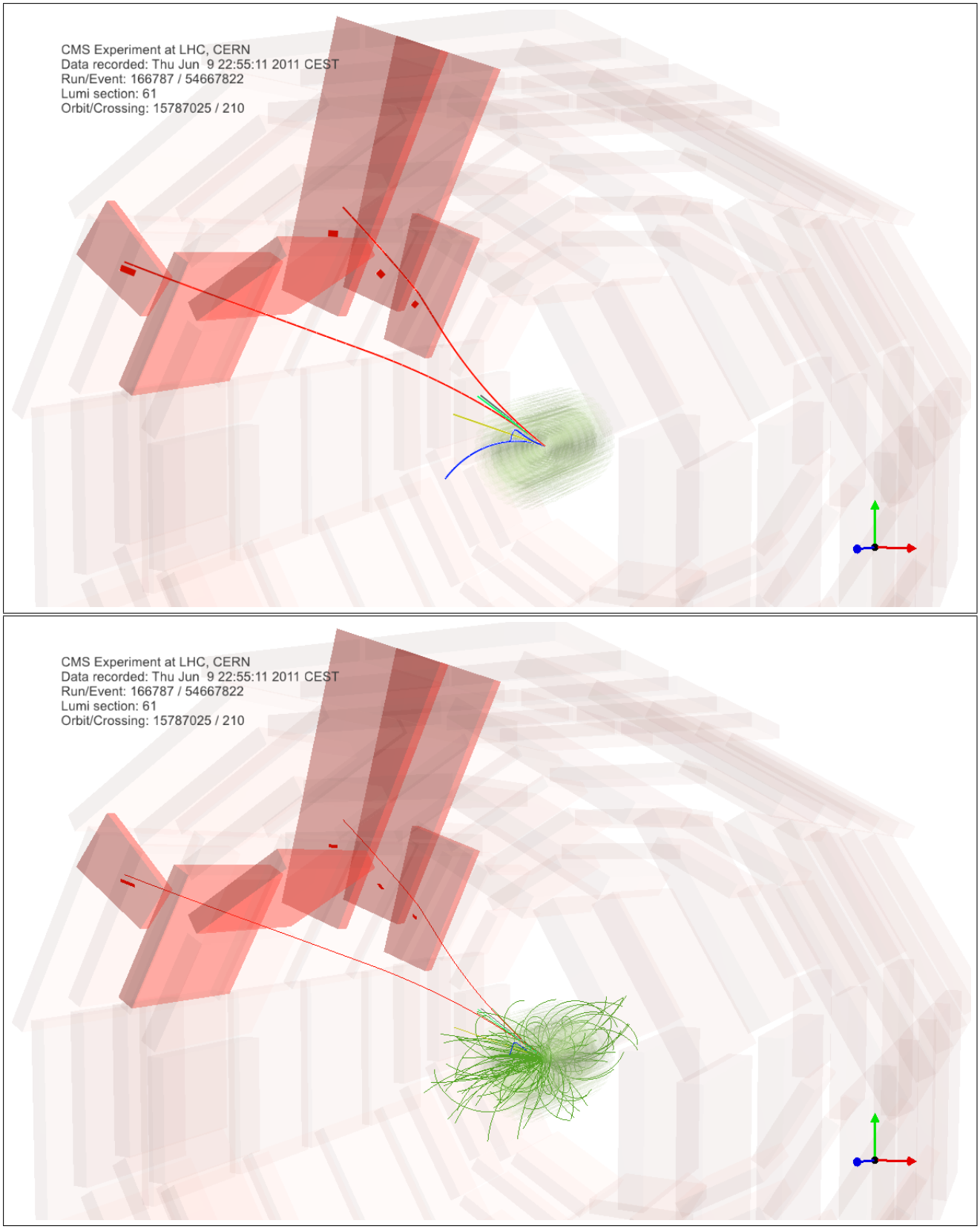

Figure A.2: Red: μ, yellow: γ candidate, blue: conversion e, light green: χ_c candidate, gray: J/ψ candidate, dark green: other tracks

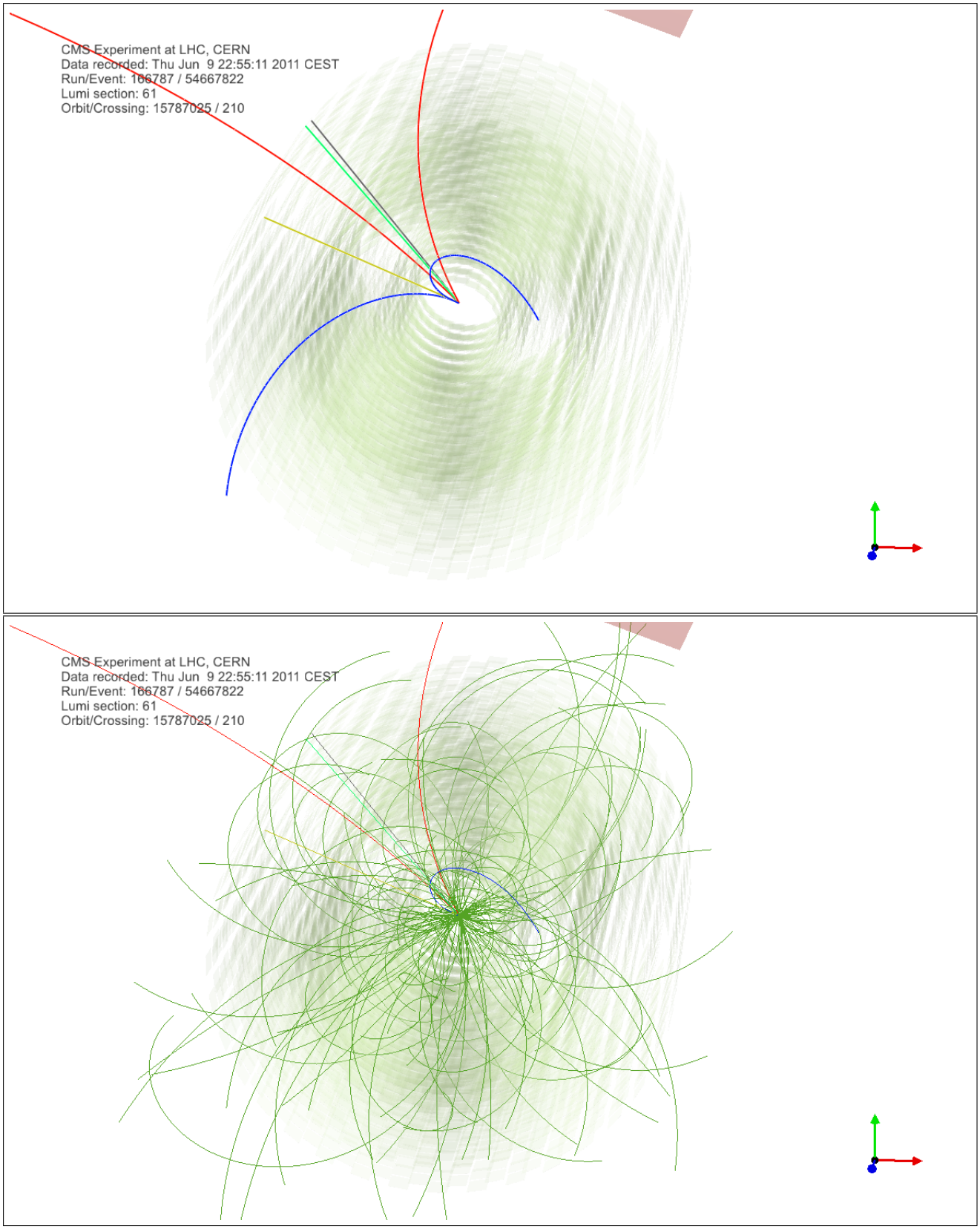

Figure A.3: Red: μ, yellow: γ candidate, blue: conversion e, light green: χ_c candidate, gray: J/ψ candidate, dark green: other tracks

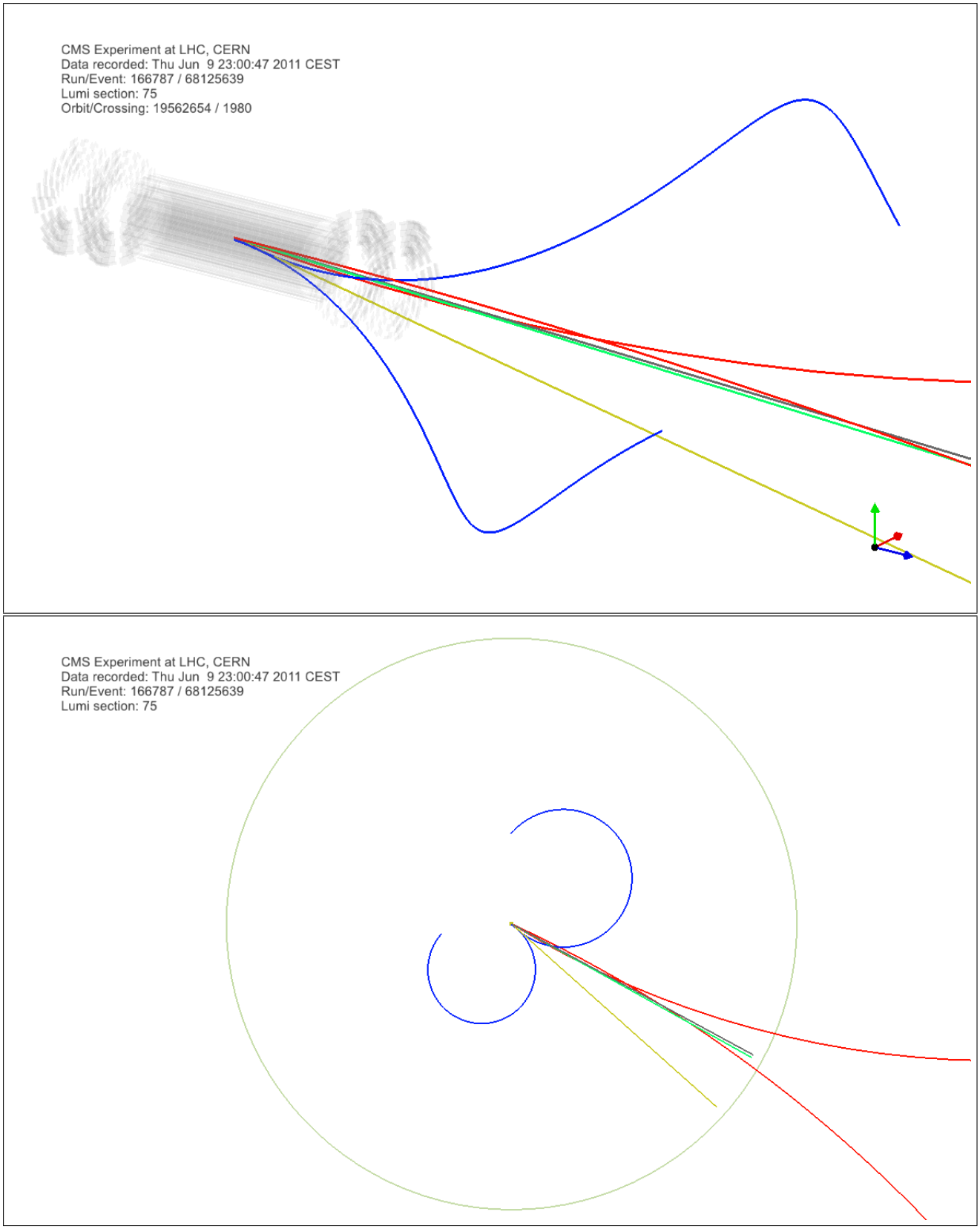

Figure A.4: Red: μ, yellow: γ candidate, blue: conversion e, light green: χ_c candidate, gray: J/ψ candidate, dark green: other tracks

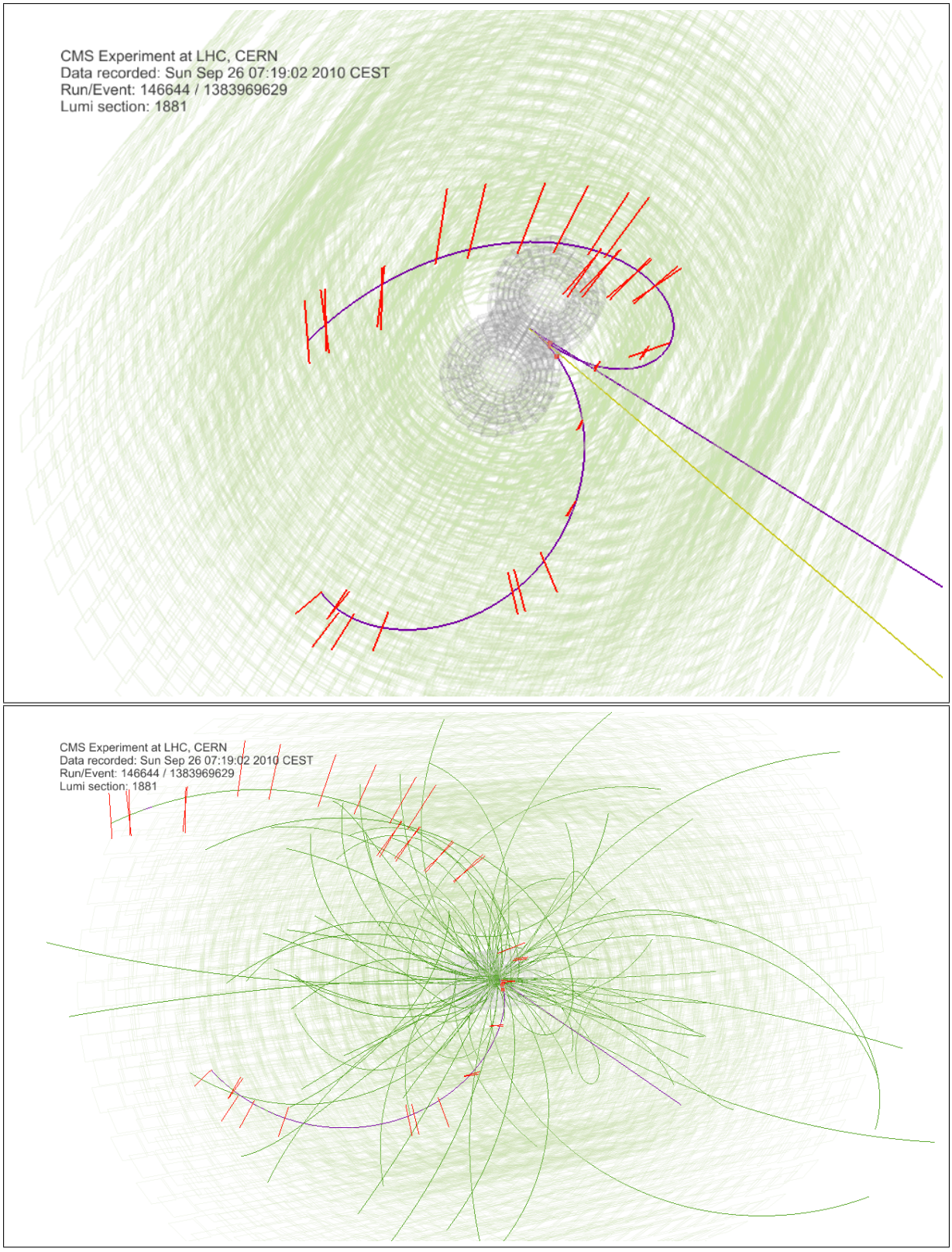

Figure A.5: Event display

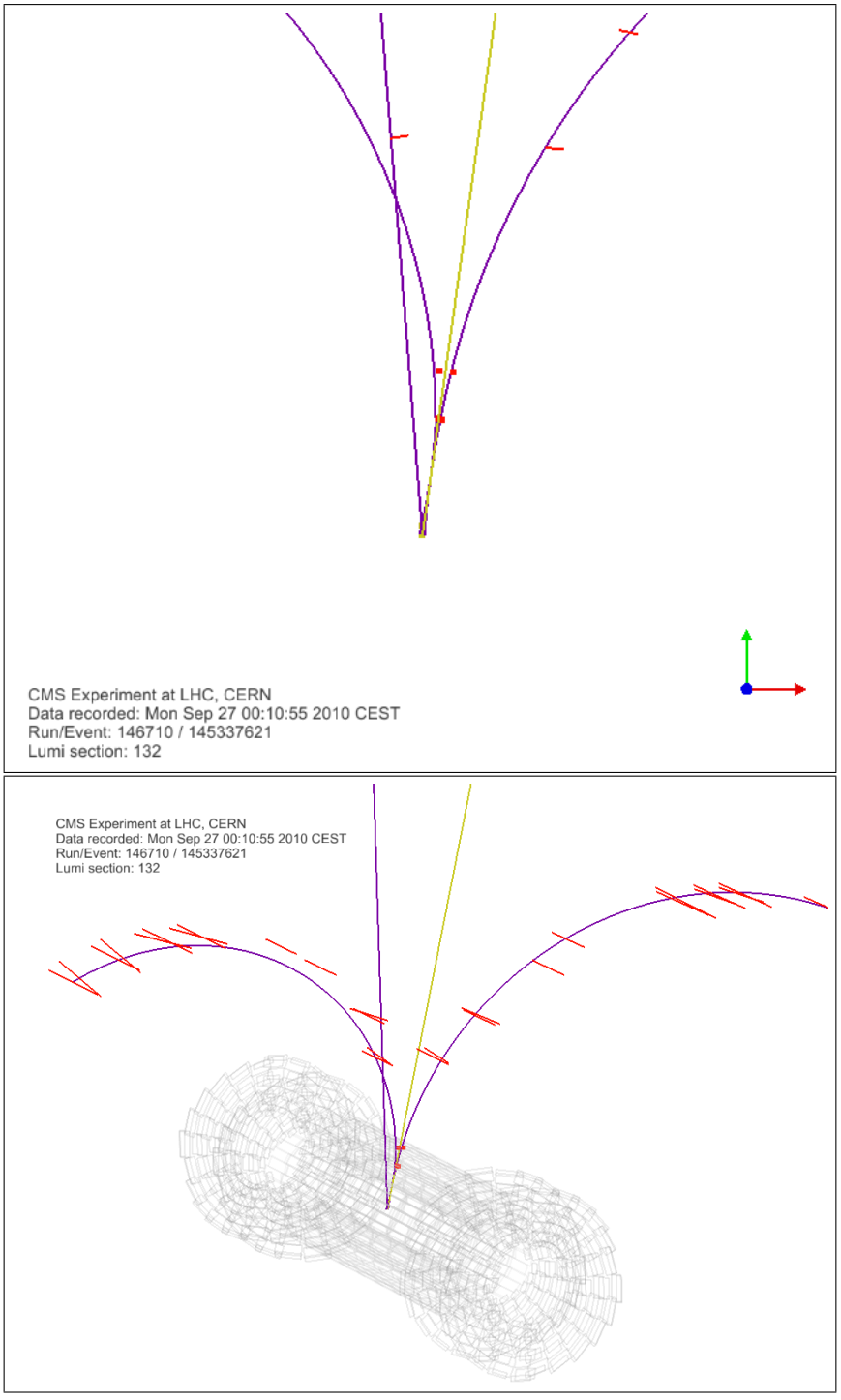

Figure A.6: Event display

Appendix B

Plots on χ_c candidates

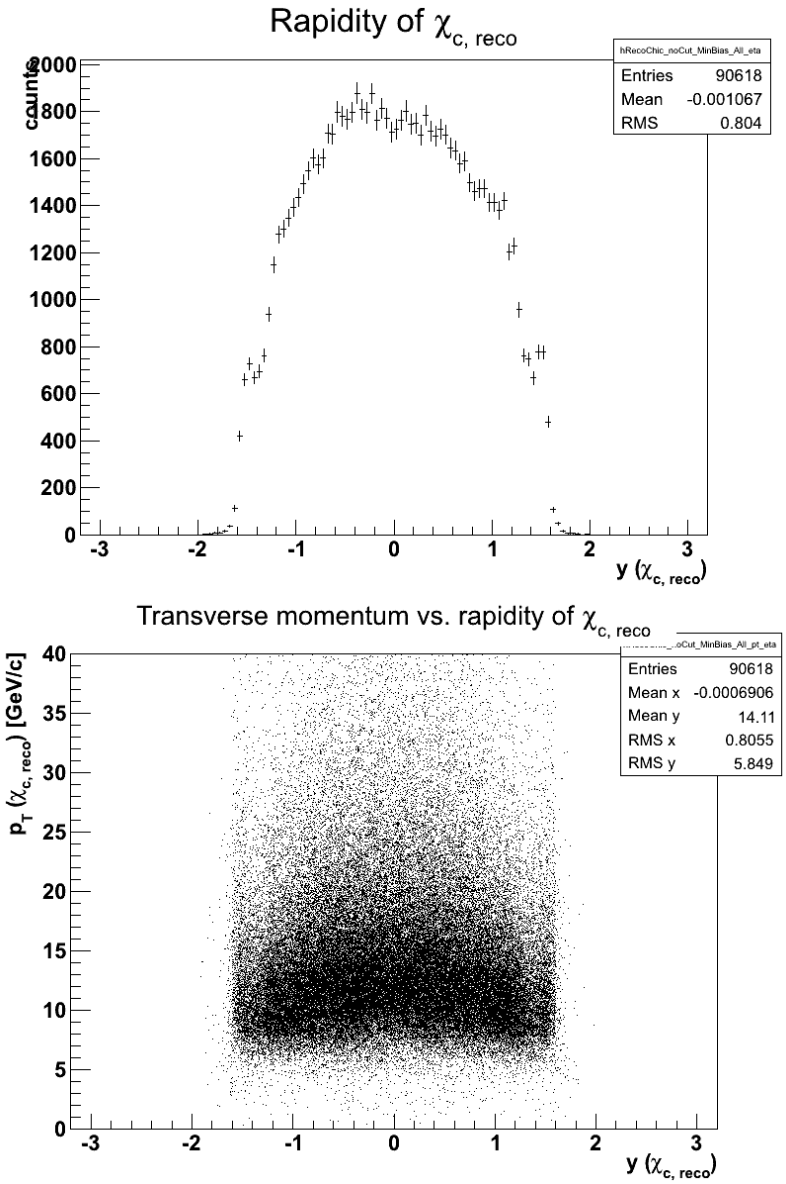

Figure B.1: Various χ_c candidates plot

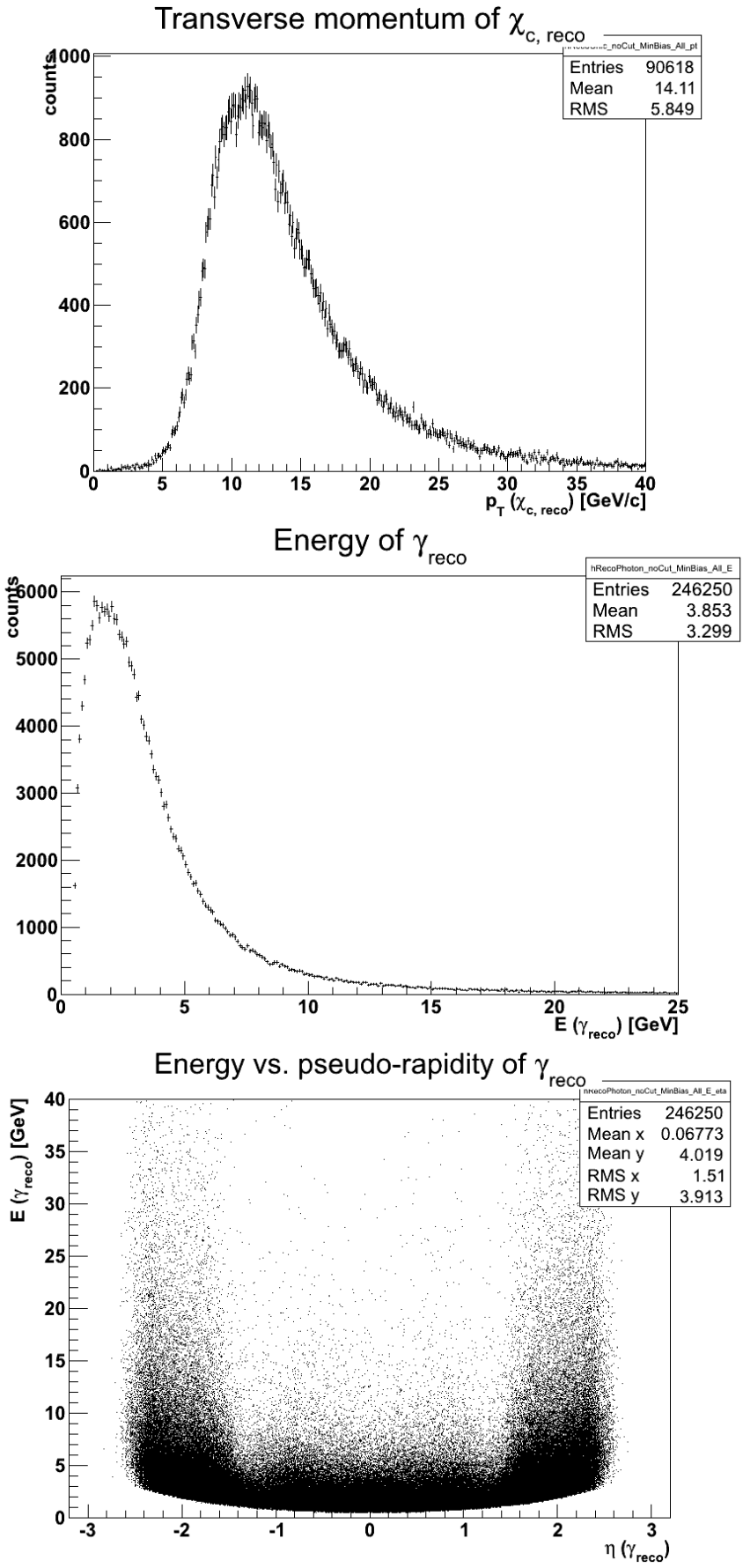

Figure B.2: Various χ_c candidates plot

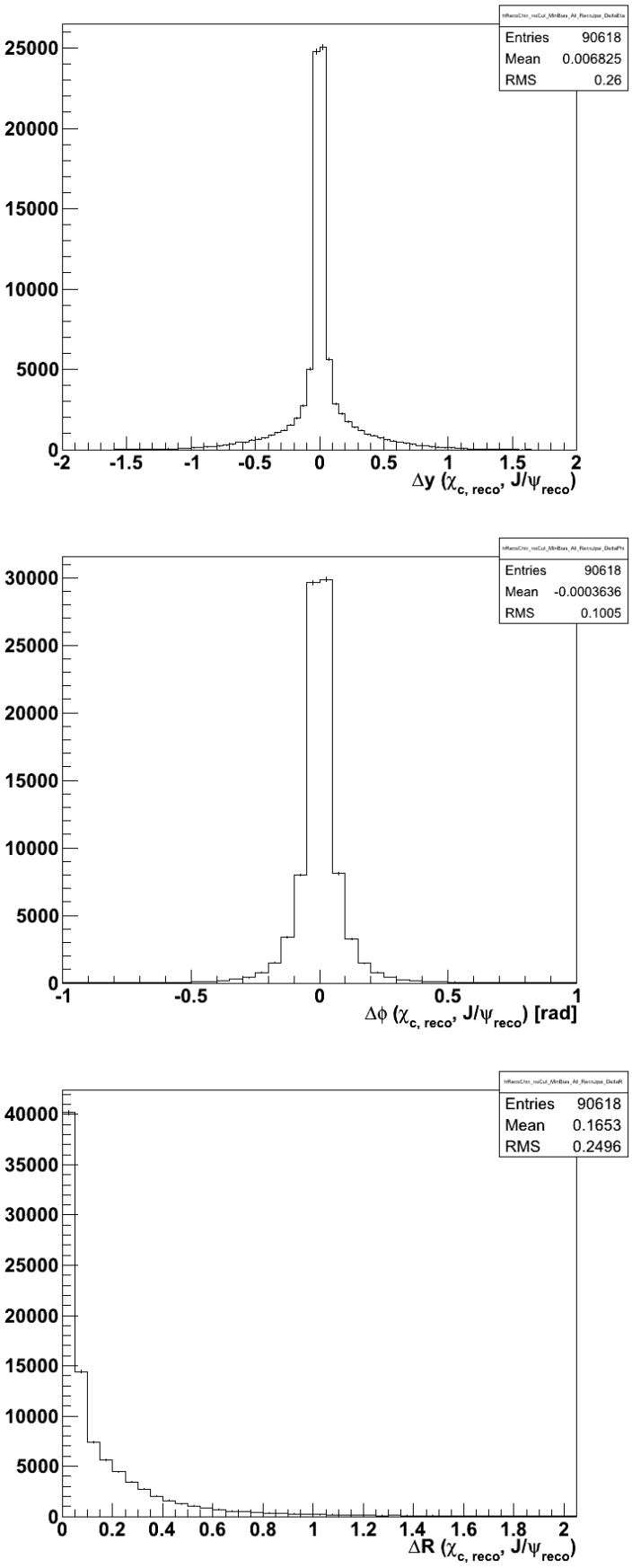

Figure B.3: Various χ_c candidates plot

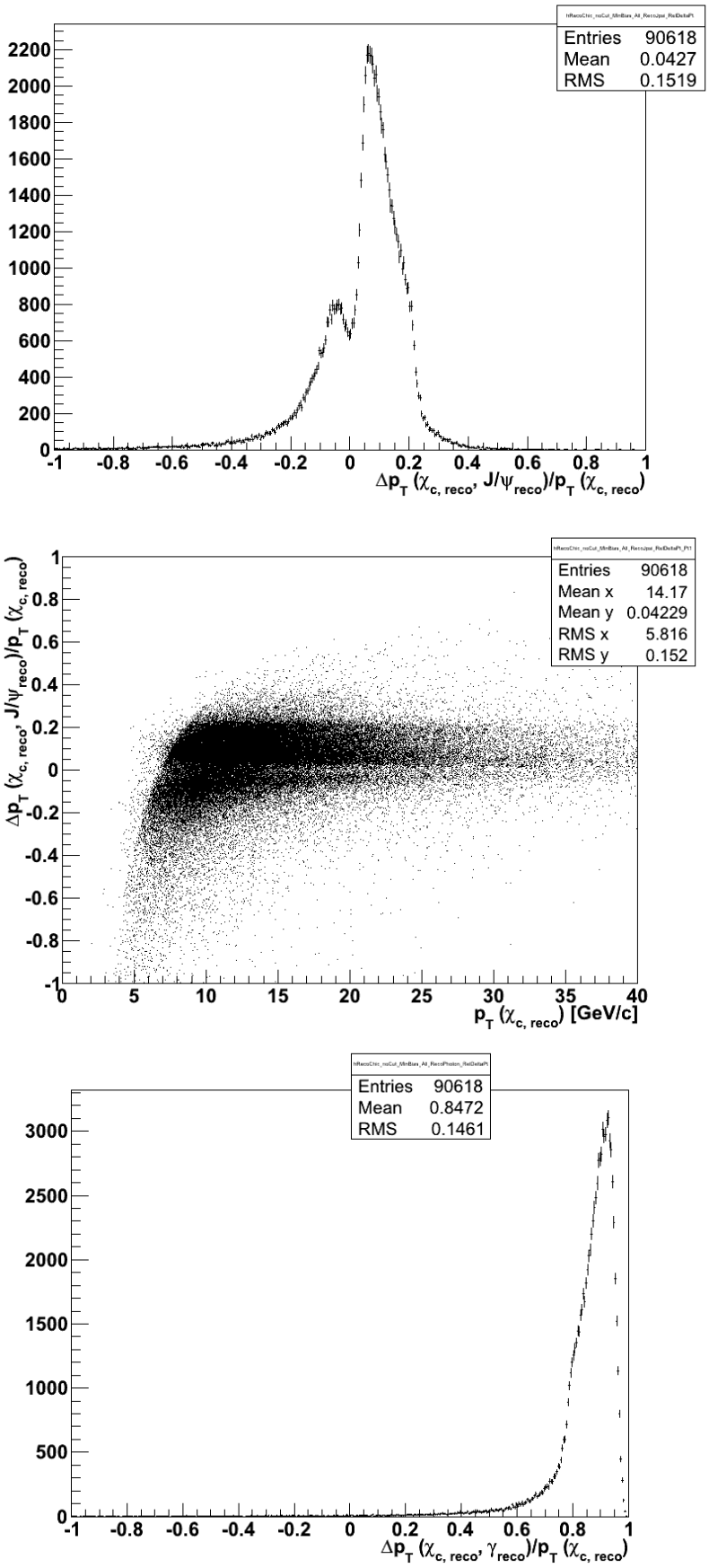

Figure B.4: Various χ_c candidates plot

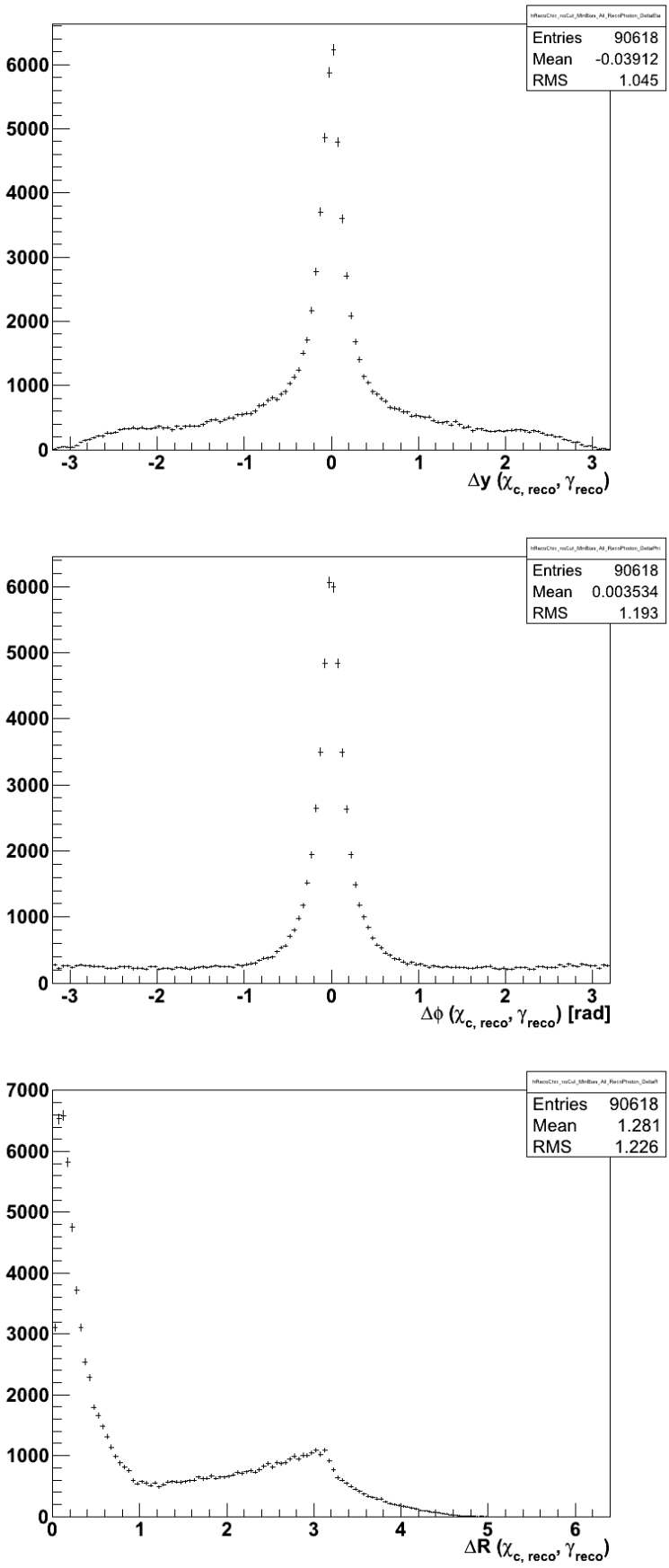

Figure B.5: Various χ_c candidates plot

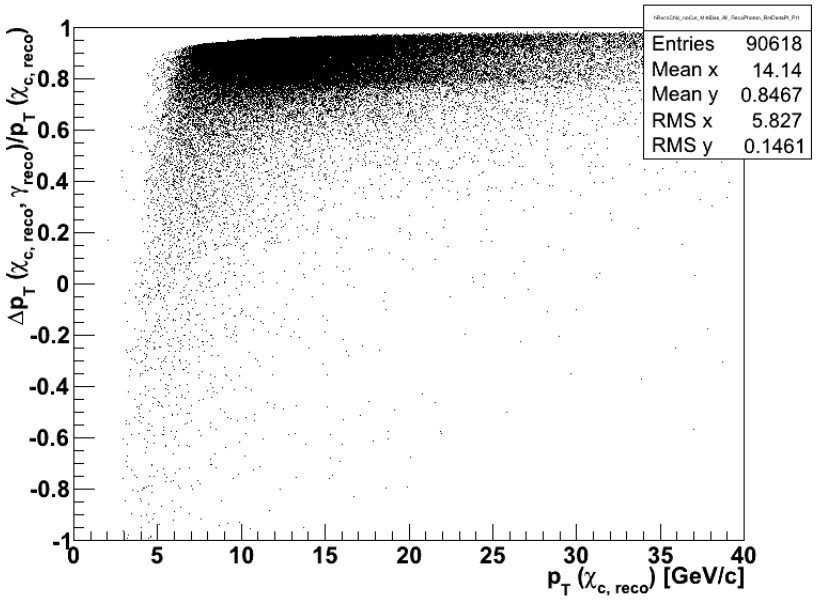

Figure B.6: Various χ_c candidates plot

Appendix C

PYTHON code used to perform the unbinned fit

```
from ROOT import RooDataSet,RooRealVar,RooArgSet,RooFormulaVar,RooGenericPdf
from ROOT import RooCBShape,RooAddPdf, RooArgList, RooPlot, RooDataHist, RooFitResult
from ROOT import RooFit
from ROOT import TFile,TCanvas,TH1F,TGraphErrors,gPad
import ROOT
from array import array
from math import sqrt

def dofit (roodataset, hname,plots,type='unbinned') :
    """Fit the chic lineshape, type is 'binned' or 'unbinned' (default)  """

    # m_chic1 is free, fix delta masses
    m_chic1= RooRealVar("m_{#chi_{1}}","m_{#chi_{1}}",3.51066,3.41066,3.61066)

    dm10= RooRealVar("dm10","dm10",-0.095910);
    dm12= RooRealVar("dm12","dm12",0.045540);

    m_chic0 = RooFormulaVar("m_chic0","@0+@1",RooArgList(m_chic1,dm10));
    m_chic2 = RooFormulaVar("m_chic2","@0+@1",RooArgList(m_chic1,dm12));

    sigma  = RooRealVar("#sigma","#sigma",0.009,0.005,0.015)
    alpha  = RooRealVar("#alpha","#alpha",1,0,5)
    n      = RooRealVar("n","n",1,0,5)

    ## define power low and exponential
    x      = RooRealVar("invm","#chi_{c} Data",3.2,4.0);
    alpha1 = RooRealVar("#alpha_{1}","#alpha_{1}",1.0,-50.,50.)
    beta1  = RooRealVar ("#beta_{1}","#beta_{1}",-1.6,-50.,50.)
    q0     = RooRealVar ("q0","q0",3.2)
    a      = RooFormulaVar ("a","@0-@1",RooArgList(x,q0))
    b      = RooFormulaVar ("b","@0*(@1-@2)",RooArgList(beta1,x,q0))
    background = RooGenericPdf ("background","bkg",
                                "pow(a,#alpha_{1})*exp(b)",
                                RooArgList(a,alpha1,b))

    #define resonances signal
    chic1_sig      = RooCBShape ("chic1_sig","chic1_sig",x,m_chic1,sigma,alpha,n)
    chic1_nevt     = RooRealVar ("N#chi_{c1}","N#chi_{c1}",6000,0,1000000)
```

```
chic2_sig      = RooCBShape ("chic2_sig","chic2_sig",x,m_chic2,sigma,alpha,n)
chic2_nevt     = RooRealVar ("N#chi_{c2}","N#chi_{c2}",2000,0,1000000)

chic0_sig      = RooCBShape ("chic0_sig","chic0_sig",x,m_chic0,sigma,alpha,n)
chic0_nevt     = RooRealVar ("N#chi_{c0}","N#chi_{c0}",200,0,100000)

background_nevt= RooRealVar("N_{bkg}","N_{bkg}",5000,0,100000000)

modelPdf= RooAddPdf("ModelPdf","ModelPdf",
                    RooArgList(chic0_sig,chic1_sig,chic2_sig,background),
                    RooArgList(chic0_nevt,chic1_nevt,chic2_nevt,background_nevt))

#fit
if type is 'binned':
    data = RooDataHist("data","signal+background data",RooArgSet(x),roodataset)
else :
    data = roodataset

result = modelPdf.fitTo(data,RooFit.Save())

frame= x.frame(RooFit.Title(hname))
data.plotOn(frame)
modelPdf.plotOn(frame)
modelPdf.paramOn(frame,RooFit.Layout(0.65))

#argset =     RooArgSet(chic1_sig,background)
argset =     RooArgSet(chic1_sig)
modelPdf.plotOn(frame,RooFit.Components(argset),
                RooFit.LineColor(8),RooFit.LineStyle(2));

#argset =     RooArgSet(chic0_sig,background)
argset =     RooArgSet(chic0_sig)
modelPdf.plotOn(frame,RooFit.Components(argset),
                RooFit.LineColor(6),RooFit.LineStyle(2));

#argset =     RooArgSet(chic2_sig,background)
argset =     RooArgSet(chic2_sig)
modelPdf.plotOn(frame,RooFit.Components(argset),
                RooFit.LineColor(2),RooFit.LineStyle(2));

argset =     RooArgSet(background)
modelPdf.plotOn(frame,RooFit.Components(argset),
                RooFit.LineColor(2),RooFit.LineStyle(2));

frame.GetXaxis().SetTitle("m_{#gamma #mu^{+} #mu^{-}} - m_{#mu^{+} #mu^{-}}
+ m^{PDG}_{J/#psi}  [GeV/c^{2}]")
frame.GetXaxis().SetTitleSize(0.04)
frame.GetYaxis().SetTitleSize(0.04)
frame.GetXaxis().SetTitleOffset(1.1)
frame.GetXaxis().SetLabelSize(0.04)
frame.GetYaxis().SetLabelSize(0.04)

frame.chiSquare()
frame.Draw()
```

```
plots.append(frame)

cr= result.correlation(chic1_nevt,chic2_nevt)

return (chic0_nevt.getVal(),chic0_nevt.getError(),
        chic1_nevt.getVal(),chic1_nevt.getError(),
        chic2_nevt.getVal(),chic2_nevt.getError(),
        alpha.getVal(), alpha.getError(),
        sigma.getVal(), sigma.getError(),
        background_nevt.getVal(),background_nevt.getError(),
        cr
        )
```

Appendix D

Trigger Paths and datasets

Here the complete list of trigger used is reported:

HLT_Dimuon5_Upsilon_Barrel_v3
HLT_Dimuon10_Jpsi_Barrel_v3
HLT_Dimuon7_Jpsi_X_Barrel_v3
HLT_Dimuon0_Jpsi_Muon_v1
HLT_Dimuon0_Upsilon_Muon_v1
HLT_Dimuon0_Jpsi_v3
HLT_Dimuon0_Upsilon_v3
HLT_Dimuon5_Upsilon_Barrel_v5
HLT_Dimuon10_Jpsi_Barrel_v5
HLT_Dimuon7_Jpsi_X_Barrel_v5
HLT_Dimuon0_Jpsi_Muon_v6
HLT_Dimuon0_Upsilon_Muon_v6
HLT_Dimuon0_Jpsi_v5
HLT_Dimuon0_Upsilon_v5
HLT_Dimuon0_Jpsi_NoVertexing_v2
HLT_Dimuon7_Upsilon_Barrel_v1
HLT_Dimuon9_Upsilon_Barrel_v1
HLT_Dimuon10_Jpsi_Barrel_v6
HLT_Dimuon13_Jpsi_Barrel_v1
HLT_Dimuon0_Jpsi_Muon_v7
HLT_Dimuon0_Upsilon_Muon_v7
HLT_Dimuon0_Jpsi_v6
HLT_Dimuon0_Upsilon_v6
HLT_Dimuon0_Jpsi_NoVertexing_v3
HLT_Mu5_L2Mu2_Jpsi_v8
HLT_Mu5_L2Mu2_Jpsi_v9
HLT_Mu5_Track2_Jpsi_v9
HLT_Mu7_Track7_Jpsi_v10
HLT_Dimuon7_PsiPrime_v3
HLT_Dimuon7_PsiPrime_v5
HLT_Dimuon9_PsiPrime_v1
HLT_Dimuon11_PsiPrime_v1

Here the complete list of datasets used is reported:

Data:

```
/MuOnia/Run2011A-May10ReReco-v1/AOD
/MuOnia/Run2011A-PromptReco-v4/AOD
/MuOnia/Run2011A-PromptReco-v5/AOD
/MuOnia/Run2011A-PromptReco-v6/AOD
/MuOnia/Run2011B-PromptReco-v1/AOD
```

Montecarlo:

```
/JPsiToMuMu\_2MuPEtaFilter_7TeV-pythia6-evtgen/Summer11-PU_S4_START42_V11-v2/
```

Appendix E

Tracker image

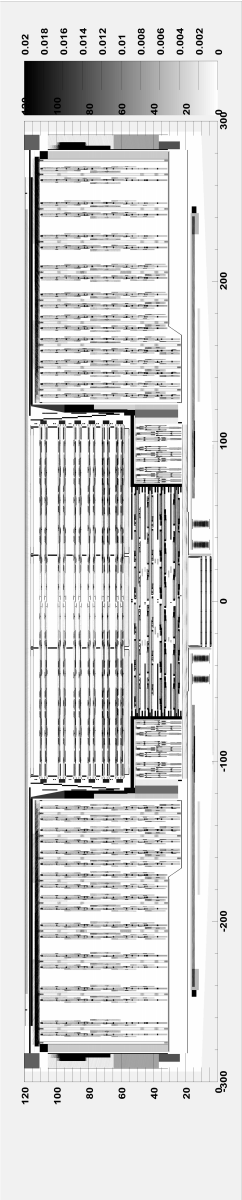

Figure E.1: Tracker "radiography" obtained with Montecarlo conversions vertices distribution.

Bibliography

[1] The CDF Collaboration A. Abulencia et al. Measurement of $\sigma(\chi_{c2})b(\chi_{c2} \rightarrow j/\psi\,\gamma)/\sigma(\chi_{c1})b(\chi_{c1} \rightarrow j/\psi\,\gamma)$ in $p\bar{p}$ collisions at $\sqrt{s} = 1.96tev$. *Phys. Rev. Lett.*, 2007.

[2] Y. Keung V.D. Barger and R.J. Phillips. *Phys.Lett. B, 91:253*, 1980.

[3] W. E. Caswell and G. P. Lepage. Effective lagrangians for bound state problems in qed, qcd, and other field theories. *Phys.Lett. B, 167:437*, 1986.

[4] The CMS collaboration. The magnet project technical design report tech.rep. *CERN/LHCC 97-10 and CMS TDR1, CERN*, 1997.

[5] The CMS collaboration. The tracker project, technical design report. *CERN/LHC 1998-006, CMS TDR 5*, 1998.

[6] The CMS collaboration. Detector performance and software, physics technical design report, vol. i. *CERN/LHC 2006-001, CMS TDR 8.1*, 2006.

[7] The CMS collaboration. j/ψ prompt and non-prompt cross sections in pp collisions at $\sqrt{s} = 7tev$. *CMS PAS BPH-10-002*, 2010.

[8] The CMS collaboration. Studies of tracker material. *CMS-PAS-TRK-10-003*, 2010.

[9] The CMS collaboration. Tracking and vertexing results from first collisions. *CMS-PAS-TRK-10-001*, 2010.

[10] H. T. Haber et al. The search for supersimmetry: probing physics beyond the standard model. *Physics Report 117, pg.75*, 1985.

[11] K. Anikeev et al. B physics at the tevatron: Run ii and beyond. 2002.

[12] M. Raymond et al. The cms tracker apv25 0.25 mm cmos readout chip. *Proceedings of the 6th workshop on electronics for LHC experiments, Krakow, Poland*, 2000.

[13] R. Adolphi et al. The cms experiment at the cern lhc. *JINST 0803*, 2008.

[14] K. Nakamura et al. (Particle Data Group). *J. Phys. G 37, 075021*, 2010.

[15] H. Fritzsch. *Phys.Lett. B, 67:217*, 1977.

[16] Eric Braaten Geoffrey T. Bodwin and G. Peter Lepage. Rigorous qcd analysis of inclusive annihilation and production of heavy quarkonium. *ERRATUM-IBID.D, 55:5853*, 1997.

[17] J.F. Owens M. Glock and E. Reya. *Phys.Lett. D, 17:2324*, 1978.

[18] F. Halzen. *Phys.Lett. B, 69:105*, 1977.

[19] LHC Higgs Cross Section Working Group Handbook of LHC Higgs Cross Sections. 1. inclusive observables. *arXiv:1101.0593*.

[20] The LHC study group. Lhc the large hadron collider: conceptual design. *CERN/AC/95-05 vol.II*, 1995.

[21] B. A. Thacker and G. Peter Lepage. Heavy-quark bound states in lattice qcd. *Phys.Lett. D, 43(1):196-208*, 1991.

[22] J. L. Rosner W. Kwong, , and C. Quigg. Heavy-quark systems. *Annual Review of Nuclear and Particle Science*, 1987.

[23] Kuang-Ta Chao Yan-Qing Ma, Kai Wang. Qcd radiative corrections to χ_{cJ} production at hadron colliders. *Phys. Rev. D*, 2011.